UNIVERSITÀ DEGLI STUDI DI TRIESTE

XXVIII CICLO DEL DOTTORATO DI RICERCA IN

ENVIRONMENTAL AND INDUSTRIAL FLUID MECHANICS

SPILLWAY STILLING BASINS AND PLUNGE POOLS LINING DESIGN

Settore scientifico-disciplinare: **ICAR/01**

PH.D STUDENT:	Shayan Barjastehmaleki
PH.D. PROGRAM DIRECTOR:	Prof. Vincenzo Armenio
THESIS SUPERVISOR:	Prof. Virgilio Fiorotto
THESIS CO-SUPERVISOR:	Prof. Elpidio Caroni

ANNO ACCADEMICO 2014 / 2015

Shayan Barjastehmaleki
Dipartimento di Ingegneria e Architettura,
Universit`a degli Studi di Trieste,
P.le Europa 1, 34127,
Trieste, Italy
shayan.barjastehmaleki@phd.units.it
shayan.malekii@gmail.com

Day of the defence: 29th April 2016

Signature from head of Ph.D. committee:

Abstract

The stability of slabs at the bottom of spillway stilling basins or plunge pools downstream of large dams came to the great practical interest when the slab protection in some hydraulic plants was seriously damaged by floods smaller than maximum design value. This thesis offers novel practical design criteria to define the concrete thickness of spillway stilling basins and plunge pools Lining. In the case of spillway stilling basins, the study presents a new experimental procedure that can define the global instantaneous uplift force. Results from detailed experiments of the statistical structure of turbulence pressure fluctuations at the bottom of hydraulic jumps is reported. Here, the whole spatial correlation structure of the fluctuating pressure field is required in order to evaluate slab stability. This is computed via simultaneous acquisition of the point pressure fluctuations on a dense grid in the hydraulic jump region, requiring a severe experimental work. As an alternative, one can evaluate spatial correlation structure of the pressure via auto-correlation using one point pressure acquisition and applying the Taylor hypothesis. To adopt the Taylor hypothesis, one must know the pressure propagation celerity in space that can be obtained by comparing the whole spatial pressure correlation with the pivot point pressure auto-correlation. The experiments were performed by simultaneous pressure acquisitions at the bottom of the hydraulic jumps for Froude numbers of the incident flow ranging from 4.9 to 10.3. From experiments, a criterion to define the pressure celerity as a function of the incident flow velocity is presented. The results highlight a good agreement between the relevant pressure statistical parameters as measured and the ones computed using the Taylor hypothesis. The comparison between the slab thicknesses as computed via Taylor hypothesis with the ones retrievable in literature (obtained by direct force measurement on instrumented slabs in laboratory conditions) highlights the accuracy of the proposed approach that presents undeniable practical advantages.

While this simplified approach based on the Taylor hypothesis is used to assess the pressure field acting on the slab, the pressure propagations at the lower surface of the slab is evaluated by developing a new 3D model based on unsteady flow analysis of seepage through porous media. By this approach, it is possible to consider the effect of finite thickness foundation layers, typical in the case of earth dams, rock-fill dams and in other dam types. Slabs with unsealed joints are considered and compared to the case of sealed joints. The dynamic behavior of anchored slabs is also investigated. These results are relevant to a robust and safe design and maintenance of stilling basins downstream of large dams.

In the case of plunge pools, the stability of concrete slabs or rock blocks under the impact of an impinging jet is theoretically analyzed, with reference to the mean characteristics of the flow field: pressure and velocity. In cases that the mean components are relevant respect to the fluctuating ones this analysis is exhausting. In other cases, a separate evaluation of the fluctuation effects in lining design is treated, by means of experimental evidences. The mean dynamic pressure at the bottom depends strongly on the impingement angle that assumes a relevant role in the design of floor protections. In plunge pools which are confined upstream by the presence of the drop structure, the impingement angle is theoretically determined by mass balance and momentum conservation, resulting independent on the jet entrance angle at the plunge pool water surface. The theoretical results are compared with literature experimental evidences and numerical simulations. This highlights the capability of the proposed theoretical framework to correctly interpret the physical phenomena and to produce suitable engineering approaches in plunge pools bottom lining design.

This thesis is dedicated to my parents

For their endless love, support and encouragement.

Acknowledgements

First and foremost I would like to sincerely thank my Supervisors Prof. Fiorotto and Prof. Caroni. It has been an honor to be their last Ph.D student. They have taught me, both consciously and unconsciously, how good experimental and numerical hydraulics is done. I appreciate all their contributions of time, ideas and funding to make my Ph.D experiences productive and stimulating. The joy and enthusiasm they have for their researches was contagious and motivational for me, even during tough times in the Ph.D pursuits.

I would like to thank Lucia, the wife of Prof. Fiorotto for her endless kindness and nice hospitality during the days I was working with Prof. Fiorotto in Mestre.

I would like to thank the technical assistant with my laboratory experiments, in particular, Mr Ruzzier.

Thanks to Professor Hajikandi, my former advisor at University of Central Tehran. Without his encourage I would not have started my study in Italy and owned what I own today.

I would like to thank my colleagues at Units for making my time a colorful one. My time in Trieste was made enjoyable in large part due to the many friends and the groups that became a part of my life. I am grateful for time spent with friends, for my buddies and our memorable trips to San Foca, Croatia and Zugliano, for Corbatto, Santo and Leonardi familys' hospitality, and for many other people and memories.

Many individuals have Support me over the years. I am especially grateful to:

Mehrdad Mortezaei, Marco Santo, Alessandro Leonardi, Alessandro Corbatto, Rosanna Klun, Piero Favero, Roberta Formisano, Michela Dal cin, and Kristina Habjan.

I will forever be thankful to my cousins in Trieste: Dr. Mahmoud Ghasempour, Dr. Saheb Ghasempour, Sara, Nadia, Avid, Archia, Dario, Daniele and Simone. I am indebted to them for their help and constant support.

A very special thanks goes out to Katrin. Through good times and Bad, your kindness and extensive support was present in the first two years of my Ph.D, for which I am eternally grateful.

Lastly, I would like to thank my family for all their love and encouragement. For my Mom Haniyeh, for dealing with me being worlds away, but only writing sporadically and then mainly to complain about the thesis. Thank you so much for tying up many important loose ends while I was away. For my Father Mansour who raised me with a love of science and supported me in all my pursuits. For my sister Dorsa who has inspired me to hold tight to my position no matter how complicated it gets. Thank you.

Table of Contents

List of Figures

Publications:

1. Barjastehmaleki, S., Fiorotto, V., and Caroni, E. (2016). “Spillway Stilling Basins Lining Design via Taylor Hypothesis.” *J. Hydraul. Eng.*, 10.1061/(ASCE)HY.1943-7900.0001133.
2. Barjastehmaleki, S., Fiorotto, V., and Caroni, E. (Accepted-Corrections ongoing). “Sealed and unsealed joints in stilling basins lining design.” *J. Hydraul. Eng.*
3. Fiorotto, V., Barjastehmaleki, S., and Caroni, E. (2016). “Stability Analysis of plunge pool Linings.” *J. Hydraul. Eng.*10.1061/(ASCE)HY.1943-7900.0001175.
4. Barjastehmaleki, S., Fiorotto, V., and Caroni, E. (2015). “Stochastic Analysis of Pressure Field in Hydraulic Jump Region via Taylor Hypothesis.” *E-Proc. 36th IAHR World Congress*, The Hague, the Netherlands, 1-12.

1

Introduction

High dams are built to store water and make it available for irrigation, drinking water supply, energy production and flood retention. These structures include by-pass channels or orifices to control the water level in the reservoir. In case the storage limit is attained during an important flood, water has to be released; further water level rise may be dangerous for dam safety. The discharges release water that is stored a few dozen meters higher than the river downstream. The potential energy of the water is converted in kinetic energy of flows passing in channel spillways or through orifices. The velocities reached by such flows are largely in excess of corresponding flow velocities in natural floods in the downstream reach and may produce uncontrolled erosion of the riverbed and banks. Therefore, part of this kinetic energy has to be dissipated locally, so that restitution velocities become lower. The action of energy dissipation may even be amplified by designing energy dissipators. Numerous structures have been developed by which a fast flowing water current may be transformed into a calm stream (Hager, 1992). The hydraulic jumps downstream of high dams or direct impact of falling jets on the riverbanks are often used as a solution for dissipation of water energy from floods.

A hydraulic Jump is a rapidly varied phenomenon in free surface flow. It corresponds to a discontinuous transition from supercritical to subcritical flows in an open channel. A Hydraulic jump includes several features by which excess mechanical energy may be dissipated into heat.

A free falling jet is another attractive method in which the structure is compact and means can readily be incorporated to break up the jet and dissipate substantial amounts of energy by air resistance.

In both cases, it is essential to provide a floor protection downstream of the dam. The stability of slab protection at the bottom of spillway stilling basins or plunge pools downstream of large dams came to the great practical interest when the protection under the hydraulic jump stilling basins in some hydraulic plants was seriously damaged by floods smaller than maximum design value. Most notable cases of lining damages were the stilling basin of Malpaso Dam (Sanchez Bribiesca and Capella Viscaino 1973), the tunnel of Tarbela Dam and the chute of Karnafuli Dam (Bowers and Toso 1988); other examples of damages were reported at the Hydroelectric Stations Liu Jia-Xia (in 1969) and Wu Qiang-Xi (in 1996), in China.

Numerous studies (e.g., Sanchez Bribiesca and Capella Viscaino 1973; Bowers and Tsai 1969; Bowers and Toso 1988; Toso and Bowers 1988) all agreed that the displacement of large concrete slabs were due to the intense, large, low frequency turbulent pressure fluctuations. It was pointed out that the loss of the stability of the slabs is due to the severe pulsating pressures on the slab, in particular it was detected that:

1. The pressure fluctuations may damage the sealed joints of the slabs and, through the unsealed joints, extreme pressure values may propagate from the upper to the lower surface of the slabs.
2. The instantaneous difference between the total pressures p acting on the upper surface and the pressures p_u acting on the lower surface of the slab can reach high values, occasionally causing the total uplift force to exceed the weight of the slab.
3. The instantaneous spatial structure of the pressure fluctuations may play a relevant role in the magnitude of the overall lifting force.

The thesis includes study of lining design of two cases of spillway stilling basins and plunge pools. The objectives of this thesis is to provide novel practical design criteria to define the concrete thickness of the plunge pools and stilling basins lining. In particular, in the case of spillway stilling basins, this study offers a comprehensive design approach to evaluate the protection slab thickness, considering three dimensionality of the phenomena, in the case of slab with both sealed and unsealed joints. Furthermore, the effect of anchor in this context is investigated. In the case of Plunge pools, a theoretical framework

is proposed to correctly interpret the physical phenomena and to produce suitable engineering approaches in plunge pools bottom lining design. Results are relevant to a robust and safe design and maintenance of stilling basins and plunge pools downstream of large dams.

The thesis is organized as follow: in chapter 2 the evaluation of whole structure of pressure fluctuations on slabs via Taylor hypothesis is experimentally investigated and described; in chapter 3 the computation of pressure under slabs using 3D unsteady seepage is presented. In chapter 4 some considerations about dynamic behavior of anchored slabs is reported. The stability of plunge pools lining is theoretically and numerically analyzed in chapter 5 and finally in chapter 6 some concluding remarks are given.

2

Pressure on slabs via Taylor hypothesis

2.1 Introduction

The instantaneous spatial structure of pressure fluctuations plays a key role in the evaluation of the slab stability beneath the jump (Fig. 1). The slab uplift force results from an instantaneous equilibrium unbalance between the integral of pressures p acting at the slab upper surface and the integral of pressures p_u under the slab. With reference to sealed joints, as generally used in stilling basins, the pressure p_u is determined by the tailwater depth y_2, while the pressure p is equal to the average pressure $\gamma\, y_m$ plus its fluctuating component. In this case, only the negative pressure fluctuations contribute to slab instability (being limited within cavitation), because positive fluctuations contribute to stability. For unsealed joints, as obtained when sealing fails (that was the case of the Malpaso Dam) or for purpose design in order to reduce the slab thickness (e.g. Marson et al., 2007, Caroni et al., 2002), the pressure p is due only to the fluctuating pressure component on the slab, while the pressure p_u under the slab is due to the transmission of pressures acting at the unsealed joints through the saturated foundation layer.

With reference to sealed joints, as generally used in stilling basins, the pressure p_u is determined by the tailwater depth y_2, while the pressure p is equal to the average pressure yy_m plus its fluctuating component. Fiorotto and Rinaldo (1992a) proposed a design criterion based on geometric parameters and the magnitude of the uplift force induced by severe fluctuations associated with energy dissipation in the hydraulic jump zone, giving the stable slab thickness s in the case of sealed joints as:

$$s = \frac{\gamma}{\gamma_c - \gamma}\left[\Omega^*\left(\frac{L_x}{y}, \frac{L_x}{I_x}, \frac{L_y}{I_y}\right) c_p^- \frac{u_1^2}{2g} + y_2 - y_m\right] \quad (2.1)$$

whereas, in the case of unsealed joints, it is:

$$s = \Omega\left(\frac{L_x}{y_1}, \frac{L_x}{I_x}, \frac{L_y}{I_y}\right)(c_p^+ + c_p^-)\frac{u_1^2}{2g}\frac{\gamma}{\gamma_c - \gamma} \quad (2.2)$$

where Ω and Ω^* = dimensionless coefficients related to the instantaneous spatial distribution of the pulsating pressures for sealed and unsealed joints, respectively; y_1 = depth of incident flow; y_2 = downstream tailwater depth; y_m = mean water level on the slab area; L_x and L_y = slab length and width; I_x and I_y = turbulence integral scales along the flow direction and transversally; c_p^+ and c_p^- = positive and negative pressure fluctuations ; $u_1^2/2g$ = kinetic energy head of the entering flow where u_1 is the mean velocity of inlet flow and γ and γ_c = specific weights of water and concrete (Fig. 1). The use of Eqs. (2.1) and (2.2) for design purpose needs the evaluation of the maximum positive and negative fluctuating pressures, as well as the evaluation of the reduction factors: Ω^*, for sealed joints, by:

$$\Omega^* = \frac{1}{\sigma_p N_s}\left(\sum_k \sum_{i=1}^{N_s}\sum_{j=1}^{N_s} \hat{p}_{k,i}\hat{p}_{-k,j}\right)^{1/2} \quad (2.3)$$

and Ω, for unsealed joints, by:

$$\Omega = \frac{1}{2\sigma_p N_s}\left(\sum_k \sum_{i=1}^{N_s}\sum_{j=1}^{N_s} \hat{p}_{k,i}\hat{p}_{-k,j} + \sum_k \sum_{i=1}^{N_s}\sum_{j=1}^{N_s}\sum_{k1=1}^{N_b}\sum_{k2=1}^{N_b} \alpha^*_{k,k1,i}\alpha^*_{-k,k2,j}\,\hat{p}_{k,k_1}\hat{p}_{-k,k_2} - 2\sum_k \sum_{i=1}^{N_s}\sum_{j=1}^{N_s}\sum_{k3=1}^{N_b} \alpha^*_{k,k3,j}\,\hat{p}_{k,k3}\hat{p}_{-k,i}\right)^{1/2} \quad (2.4)$$

where $\hat{p}_k$= spectral components of the fluctuating pressures, σ_p = standard deviation of the fluctuating pressures, *i*, *j*= position indexes of one of the N_s patches in which the slab area is subdivided; *k*1, *k*2, *k*3= position indexes at the N_b points along the unsealed joints; $\alpha^*_{k,k1,i}$= ratio between the underside pressure in *i* and the pressure at the *k*1 edge, for the wave number *k*. It is obtained by computing the pressure value at the *i* position under the slab, produced by a pressure $\hat{p}_k$ = 1 at the *k*1 edge and $\hat{p}_k$ = 0 at the other ones via the pressure propagation equation within the foundation layer (Fiorotto and Caroni 2014) as shown in Fig. 1. The three terms at the right hand side of Eq. (2.4) take into account: the first term the pressures acting on the slab, the second one, the pressures underneath the slab transferred through the unsealed joints, and the third one, the simultaneous pressures acting at the upper and lower slab surfaces, being transferred through the unsealed joints. One can note that in Eq. (2.3) only

the first term of Eq. (2.4) appears, being related to the pressure fluctuations on the slab, because, under the slab, the pressure is constant.

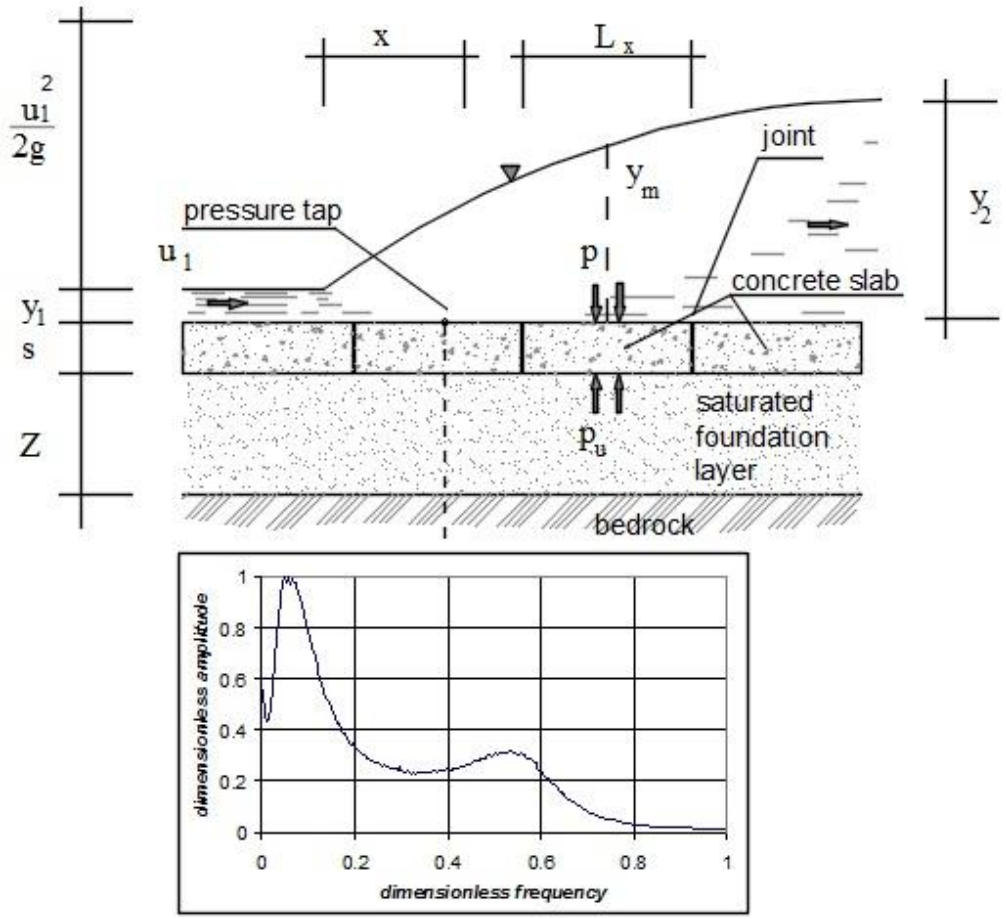

Fig. 1: Slab stability scheme and pressure spectrum, dimensionless with the maximum spectral component and half of the sampling frequency (100 Hz)

Several authors studied experimentally the statistical characteristics of hydraulic jumps: Abdul Khader and Elango (1974), Lopardo and Henning (1985), Toso and Bowers (1988), Vasiliev and Bukreyev (1967) and Wang et al. (1984). These papers have dealt with the values of standard deviation, skewness and kurtosis, maximum and minimum value, temporal and longitudinal spatial correlation of the pulsating pressures. Most of the recent investigations were conducted by Fiorotto and his colleagues. Fiorotto and

Rinaldo (1992b) measured the spatial correlation function in both transversal and longitudinal directions under the hydraulic jump. Bellin and Fiorotto (1995) provided the direct experimental evaluation of the uplift coefficient Ω. Fiorotto and Salandin (2000) examined the validity of the design criterion expressed in Eq. (2.1) for anchored slabs via experimental and theoretical analysis. Anchored concrete linings at the bottom of plunge pools, loaded by high velocity jets, were investigated by Mahzari and Schleiss (2010). Fiorotto and Caroni (2014) presented a model based on unsteady flow analysis of seepage through porous media that summarized all the models that define the propagation of pressure fluctuations within lining slab joints in stilling basins, as separately analyzed by Liu and Li (2007).

Despite these recent advances, knowledge of the spatial structure of the pressure fluctuations under the hydraulic jump as a whole, in order to compute Eqs. (2.3) and (2.4), is still insufficient. The simultaneous acquisition of pressure in a large number of points can be prohibitive in real life conditions because of its costs in terms of time and laboratory setup. To overcome these problems one can invoke the Taylor hypothesis (Taylor 1938), that allows defining the spatial correlation via auto-correlation as derived from a single pivot-point pressure measurement; yet, to our knowledge, no work can be found in literature towards this direction.

This chapter presents the results of an experimental study undertaken to evaluate the whole spatial structure of pressure fluctuations, in order to examine the validity of the Taylor hypothesis. Its application needs the definition of a celerity parameter that allows transforming the point auto-correlation in time into the spatial correlation function. Then, the characteristics of the celerity of propagation of the pulsating pressures, as related to the initial velocity, are investigated. A comparison between the Ω coefficients, as measured on instrumented slabs in laboratory, with the ones obtained via Eq. (2.4) using the Taylor hypothesis, highlights the applicability of the proposed approach in the computation of stable slab thickness.

2.2 Experimental setup and procedure

The following experimental procedure is adopted to define the statistical characteristics of the pressure field on the slab surface, while the uplift pressure under the slab is computed numerically (Fiorotto and Caroni 2014), starting from the pressure field along the slab joints.

The experiments were conducted in a horizontal rectangular flume, 0.5 m wide, 0.5 m height and 10 m long, in the Hydraulics Laboratory of University of Trieste, Italy. The flume had a Plexiglas bed and sidewalls and vertical tailgate for controlling the position of the jump along the test area. The water was supplied by a head-tank and the discharge was measured with an inline magnetic flowmeter (Toshiba LF620) with an accuracy of ±2%. The maximum discharge of the flume was 100 l/s and it was controlled by a valve in order to adjust the Froude number of the incident flow. Water entered the flume under a sluice gate that was used to control the hydrodynamic characteristics of the incoming flow (Figs. 2).

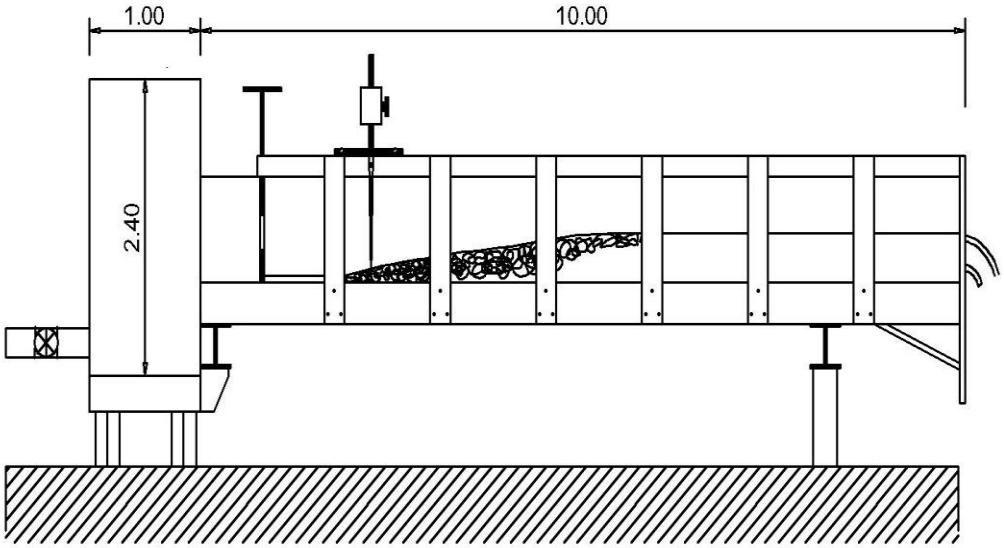

a)

b)

Fig. 2: Schematic of the experimental setup

The test area was 0.4 m wide and 0.5 m long and was located 1.9 m downstream of the sluice gate. Pressure taps with diameter of 2 mm were inserted along the center line of the flume and 12 different cross sections. The tap diameter was established based on the investigations of Fiorotto and Rinaldo (1992b), which show that increasing of the tap diameter reduces the magnitude of the measured fluctuating pressures. It is due to the effect of spatial averaging of a very small scale of turbulence that reduces the variance of the signal and the value of the maximum and minimum fluctuating pressures. The distance between two successive taps was 1 cm in stream wise direction along the center line of the flume, 1 cm in cross-stream direction at the center of test area and 2 cm in other cross-stream sections. The details of taps arrangement in the test area is shown in Fig. 3.

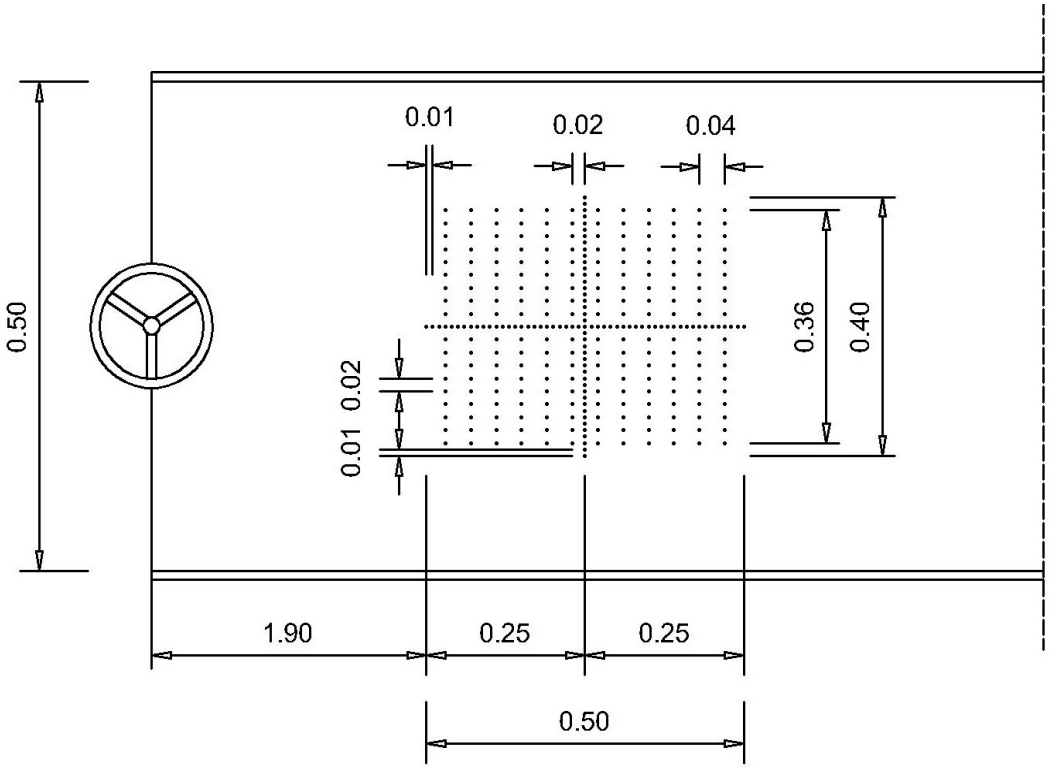

a)

b)

Fig. 3: Plane view of the test area with indication of the tap positioning

The fluctuating pressure was measured by means of AEP TP14 type pressure transducers calibrated in the range of 0-250 mbar. In the linear working range (25-225 mbar) the transient time to the Heaviside function with amplitude of 50 mbar was lower than the microscale time of the pulsating pressure measured in the previous experimental investigations (Fiortto and Rinaldo 1992b). The pressure transducers were connected to the taps by a rigid tube with the inner diameter of 4 mm and length of 0.2 m. A computer was linked to the transducers via a 16-channel capture card (United Electronic Instruments PD2MFH). Sampling was done by dasyLab 6.0 software. Since previous spectra analysis had shown that the dominant frequencies of pressure fluctuations were less than 30 Hz (Bowers and Tsai 1969), a sampling rate of 100 Hz was adopted. The acquisition time was set equal to 20 min to obtain a large enough number of data in order to get accurate evaluations of the spatial correlation functions. The upstream water depth that is needed to compute the parameters of the bulk flow was measured using point gage with accuracy of 0.1 mm at the toe of the jump. Due to the fluctuations of the toe of the jump and cross waves generated by sides of the channel, the upstream mean depth of the flow was measured several times in different points on the inlet section for each run in order to obtain the significant value of average and the standard deviation of jump toe water depth. The errors in the Froude number of the inlet flow and the kinetic head due to the effects of discharge and initial depth were estimated to be lower than 3% and 6% respectively. Special care was taken to avoid from the possible effects of inaccuracy in the transducers signal due to the effect of entrapped air inside the measurement cells and tubes, vibration of the channel floor and non-uniform distribution of the flow across the channel. In the case of air entrainment in the pressure transducers, a decrease in variance is detected. The comparison in the pressure variance between downstream and upstream pressure gages could evidence the phenomena. However, to prevent air entrapment, the pressure gauge chambers were filled by a syringe and connected while water was flowing in the rigid tubes from the pressure taps. The connections were equipped with a bleed valve to allow the removal of any air entrapped during the operation. The distance of the toe of the jump from the gate was in the range of 55-71 times the

sluice gate opening, therefore, the boundary layer can be considered as fully developed (Wilson and Turner 1972). It is important to state here that the definition of fully developed flow is the same as that used by Leutheusser and Kartha (1972), but their criterion of a distance to the jump of 200 times the sluice gate opening was found to be excessive. The boundary layer of the incident flow reached the water surface at a distance of about 50 times the gate opening, which agrees well with the data provided by Wilson and Turner (1972). Undeveloped flow tends to slightly increase the peak value of c_p^- and $c_p^{+'}$ for a given Froude number. These results are comparable to those of Abdul Khader and Elango (1974) and Toso and Bowers (1988).

Table 1 lists the details of the experiments. The inflow Froude number, $Fr = u_1/\sqrt{gy_1}$ = 4.9-10.3, is typically in the range of intermediate to strong range for a hydraulic jump, where g is the gravitational acceleration.

Table. 1. Experimental parameters of the bulk flow

Experiment	Fr	Q (L/s)	u_1 (m/s)	y_1 (mm)	y_2 (mm)
1	10.3	56.4	4.9	23	324
2	7.1	33.8	3.22	21	201
3	4.9	20.1	2.12	19	123

It should be note that the scale effects are investigated by proposed approach in the paper of Hager and Bremen (1989) in order to control the effect of channel geometry and Reynolds number. According to this paper, a hydraulic jump is not influenced by scale effects if $\omega < \omega_L$, where ω is inflow aspect ratio = $y_1\backslash b$ and ω_L is limit value for scale effects. Using Table 1 of the thesis and applying Eq. 30 of Hager and Bremen (1989) the limit condition for scale effect is computed. Fig. 4 shows ω_L as a function of Fr, for various R_1* where R_1* is modified Reynolds number = $Q/(vb)$. The comparison shows that the scale effects do not influence the experiments because $\omega < \omega_L$ in every run.

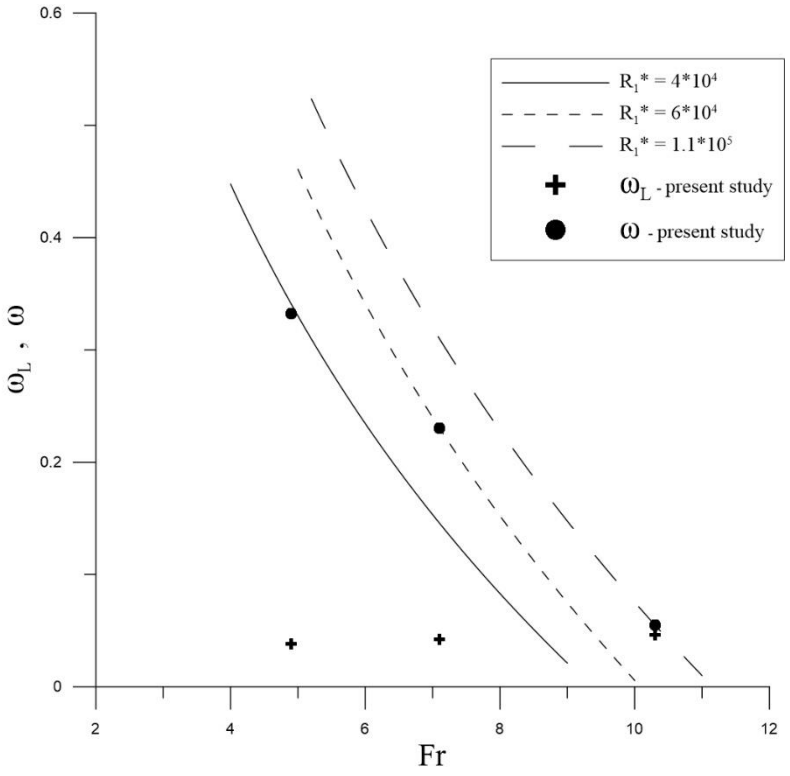

Fig. 4: Limit condition for scale effect, ω_L as a function of Fr, for various R_1*

2.3 Theoretical analysis

With the assumption of stationary in time, the following statistical properties can be evaluated:

The mean value of the pressure:

$$\bar{p}\,(x,y) = \lim_{T\to\infty} \frac{1}{T}\int_0^T p(x,y,t)dt \qquad (2.5)$$

where $p(x,y,t)$ = pressure measurement at time T in (x,y) and T = acquisition time. The space-time covariance function R:

$$R(x,\xi,y,\eta,\tau) = \lim_{T\to\infty} \frac{1}{T}\int_0^T p'(x,y,t)p'(x+\xi,y+\eta,t+\tau)dt \qquad (2.6)$$

where ξ = longitudinal distance from a pivot point in (x,y), η = transversal distance from the pivot point and $p'(x,y,t) = p\,(x,y,t) - \bar{p}(x,y)$. The correlation is σ_p^2 = $R(x,0,y,0,0)$, the auto-correlation is $R(x,0,y,0,\tau)$, and the spatial

instantaneous correlation is $R(x,\xi,y,\eta,0)$. noting that the pressure field is statistically stationary in space in the transversal direction (e.g. Lopardo and Hennings, 1985), the coefficient R is independent of the position of the pivot point in y direction, so that the correlation surface ρ at any pivot point (x,y) as a function of ξ and η, is defined by:

$$\rho(x,\xi,0,\eta,0) = \frac{R(x,\xi,0,\eta,0)}{\sigma_p(x,0)\sigma_p(x+\xi,\eta)} \tag{2.7}$$

while the auto-correlation is given by:

$$\rho(x,0,0,0,\tau) = \frac{R(x,0,0,0,\tau)}{\sigma_p^2(x,0)} \tag{2.8}$$

where σ_p = standard deviation of the pressure fluctuations. The macroscales (integral scale), in x and y direction, define the maximum distance at which, on average, two instantaneous values of fluctuation pressures are considered to be correlated. They are:

$$I_x = \int_0^\infty \rho\,(x_0,\xi,0,0,0)d\xi \quad , \quad I_y = \int_0^\infty \rho\,(0,0,y_0,\eta,0)d\eta \tag{2.9}$$

A relationship between spatial correlation and auto-correlation is provided by the Taylor hypothesis that states $\partial p/\partial t = -c_x\,\partial p/\partial x = -c_y\,\partial p/\partial y$ (Hinze 1959), where c_x and c_y are the celerity of pressure propagation in x and y directions respectively. Therefore, $\rho(x, \xi, 0, \eta, 0) = \rho(x, 0, 0, 0, \tau)$, where $\xi = c_x\tau$, and $\eta = c_y\tau$, implying the similarity between space and time correlations. This is theoretically true in the immediate surroundings of the pivot point and, for practical applications, it must hold true for extensions comparable to the slab length, where spatial stationarity of the pressure field is assumed as well. With reference to the practical application, the phenomena follow the Froude similarity, as a consequence the time, frequency, velocity and celerity are scaled with the square root of the geometrical scale while the pressure is scaled with the geometrical scale (Lopardo et. al. 1982). A first check is hence devoted to control the shape similarity in the correlation structures; subsequently, the proper values of the celerity should be sought with comparing the correlation structure made by experiment data and using Taylor hypothesis.

2.4 Experimental results and discussion

The evaluation of Ω coefficient requires the calculation of the correlation functions of the fluctuating pressures in the plane under hydraulic jumps. The task was done by simultaneous acquisition of pressure field in all the points beneath the jump. The accuracy in the correlation functions was checked by performing three different runs at every points. Eq. (2.7) was used to calculate the values of spatial correlation functions and the maximum error in the correlation functions resulted less than 3%.

Fig. 5 shows the instantaneous spatial correlation with respect to the distance from the pivot point x, dimensionless with the initial depth y_1 for different Froude numbers of incident flow. From the figure one can observe:

1. The distance of the zero crossing-point of the longitudinal correlation function does increase when the distance of pivot point from the toe of the jump increases at constant Froude number.
2. The distance of the zero crossing-point does increase when the Froude number increases at constant distance of the pivot point from the jump toe.
3. The correlation function overall shape at constant Froude number appears to be comparable when changing pivot point location, at least for lengths in the order of the slab size, so that the local homogeneity of the flow field can be applied in slab stability analysis.

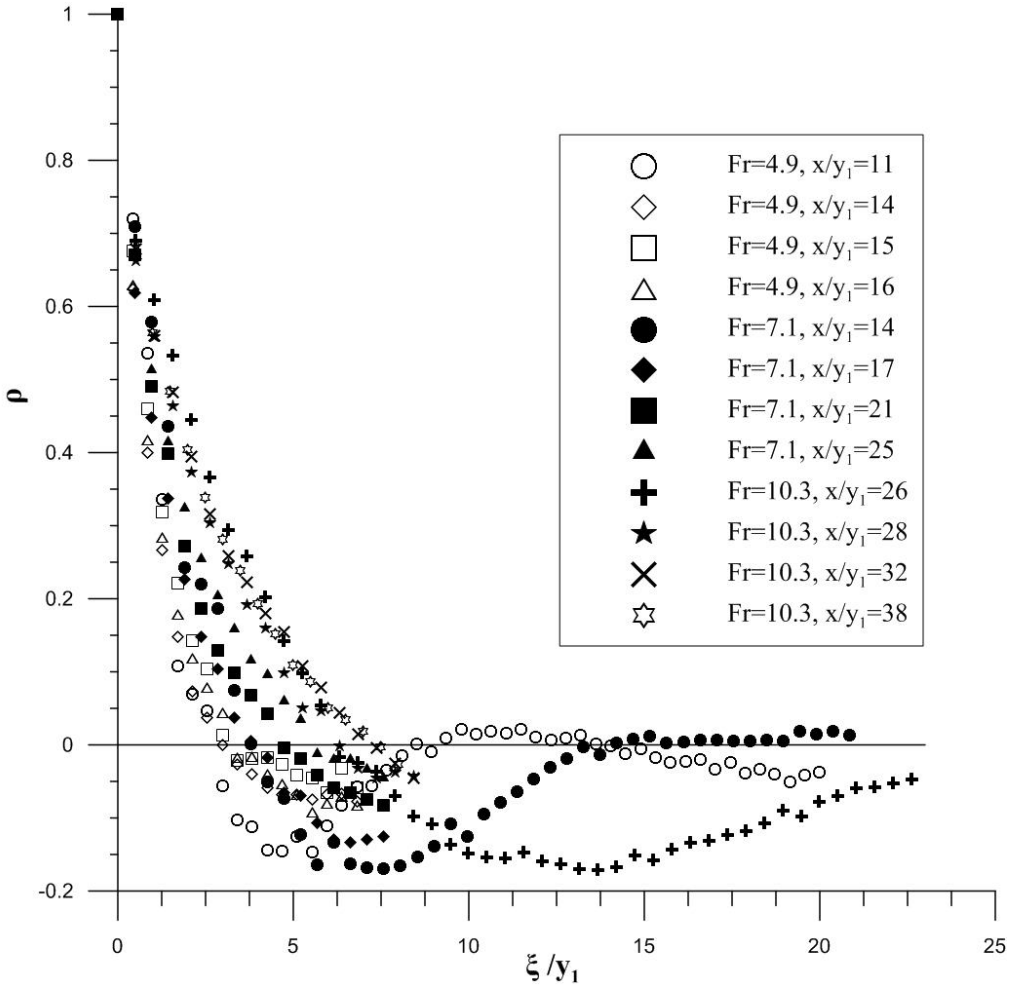

Fig. 5: Longitudinal spatial correlation function, as measured at different pivot point locations x/y_1 and Froude numbers

The value of the integral scale I_x was computed by interpolating the experimental data with a damped sine wave (Fiorotto and Rinaldo 1992b) resulting in the range $0.2 < I_x/y_1 < 2$ and it can be reasonably assumed $I_x \approx 0.2\xi_0$, where ξ_0 = distance between the origin and the first zero crossing of the longitudinal correlation. Fig. 6 reports the value of zero crossing-point ξ_0 as a function of pivot point. The experimental results reported in this figure are in a good agreement with the data of Fiorotto and Rinaldo (1992b) and Lopardo and Henning (1985) thus validating the present experimental setup.

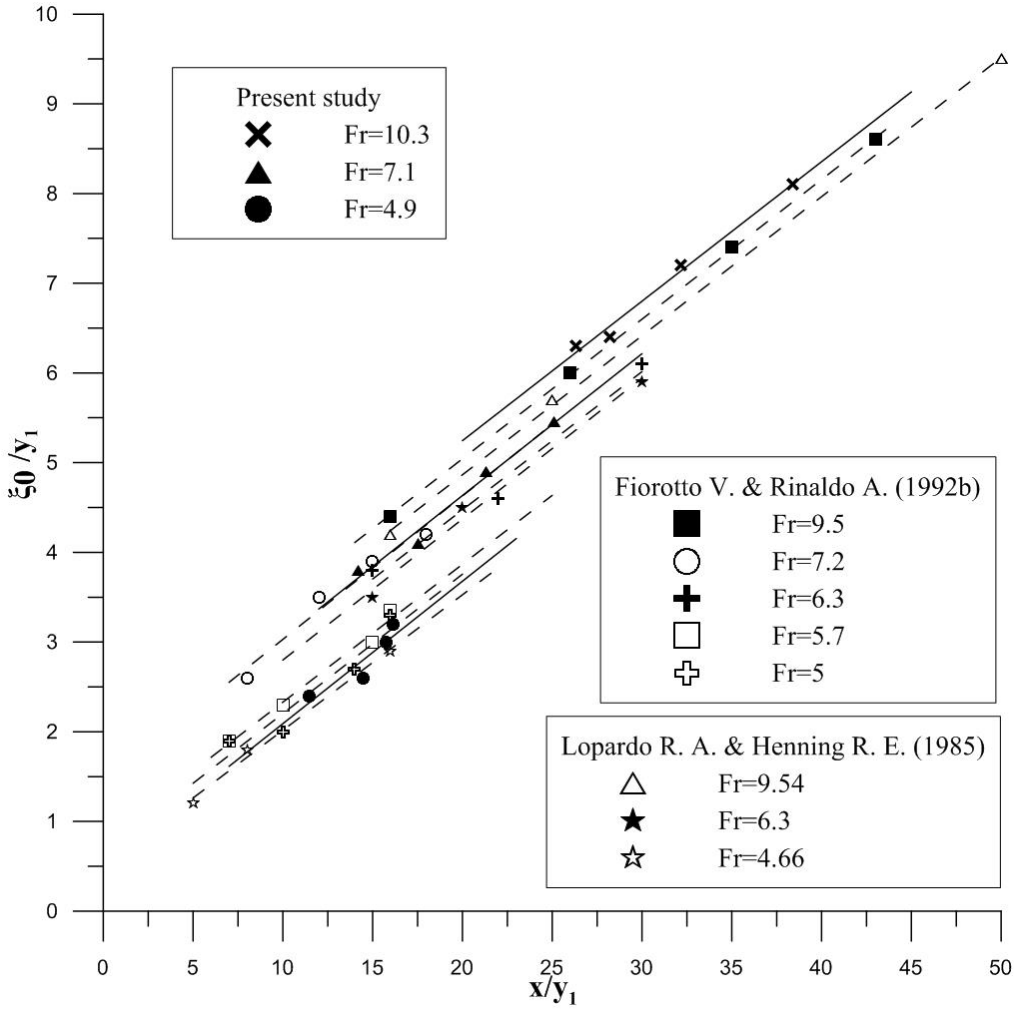

Fig. 6: ξ_0/y_1 versus x/y_1 for different Froude numbers

Fig. 7 shows the transversal correlation function with respect to the η/y_1 for different Froude numbers and pivot locations. It can be note that:

1. The transversal spatial correlation is larger than the longitudinal one.
2. The correlation function in the cross stream direction is stationary in space so that the statistical characteristics of pressure fluctuations do not depend on the y coordinate.
3. In the comparison with literature findings, the measured correlations in the transversal direction are also validated.

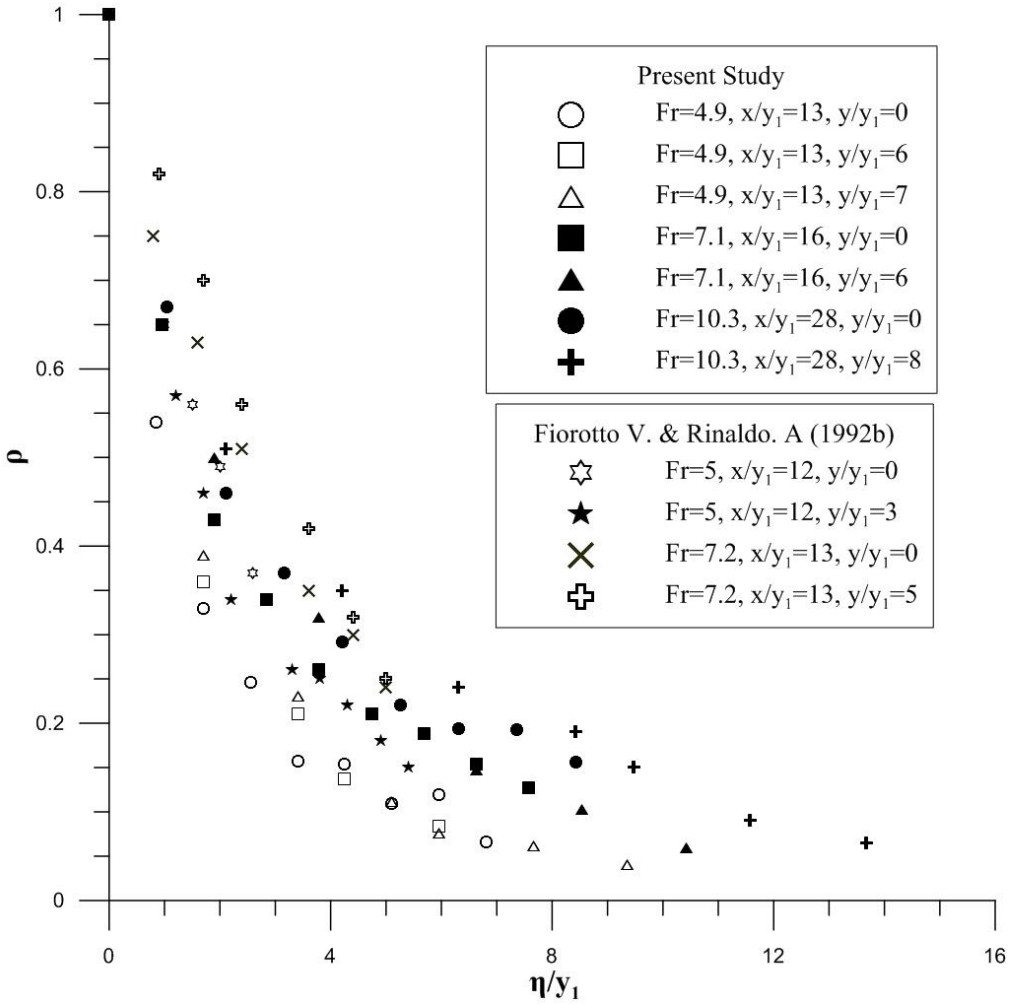

Fig. 7: Transversal correlation function for different Froude numbers (the distance y/y_1 is measured from the flume centerline)

The spatial correlation is anisotropic and the longitudinal correlation length is smaller than the transversal one, so that the largest eddies are much stretched in the cross stream direction.

The value of the transversal integral scale I_y depends on the Froude number of incident flow and the distance from the jump varies in the range of $1.5 < I_y/y_1 < 5$. To compute the Eqs. (2.1) and (2.2), the spatial correlation of the pulsating pressure on the slab is required. When the auto-correlation function at only one point is available, the Taylor hypothesis can help in deriving the instantaneous spatial pressure distribution using the proper values of the celerity.

The evaluation of the Ω coefficient by Eq. (2.4) requires the knowledge of pressure spectra, that is the spectral components $\hat{p}_k$ of the fluctuating pressures

acquired in the pivot point at distance *x* from the hydraulic jump toe. In a locally space-time stationary stochastic pressure field, Eq. 6 – 8 become:

$$\sigma_p^2 = \sum_k \hat{p}_k \hat{p}_{-k} \tag{2.10}$$

$$\rho(x,\xi,0,0,0) = \frac{1}{\sigma_p^2}\sum_k \hat{p}_k \hat{p}_{-k} e^{ik\xi} \tag{2.11}$$

$$\rho(x,0,0,\eta,0) = \frac{1}{\sigma_p^2}\sum_k \hat{p}_k \hat{p}_{-k} e^{ik\eta} \tag{2.12}$$

$$\rho(x,0,0,0,\tau) = \frac{1}{\sigma_p^2}\sum_k \hat{p}_k \hat{p}_{-k} e^{ik\tau} \tag{2.13}$$

where $= \sqrt{-1}$. Via Taylor hypothesis, the Eqs. (2.11) and (2.12) yield:

$$\rho(x,\xi,0,0,0) = \frac{1}{\sigma_p^2}\sum_k \hat{p}_k \hat{p}_{-k} e^{ik(\frac{\xi}{c_x})} \tag{2.14}$$

$$\rho(x,0,0,\eta,0) = \frac{1}{\sigma_p^2}\sum_k \hat{p}_k \hat{p}_{-k} e^{ik(\frac{\eta}{c_y})} \tag{2.15}$$

The celerity *c* between two points, 0 and 1, with distance x_1, where the spectral component $\hat{p}_k^0$ and $\hat{p}_k^1$ are known, can be computed by maximizing the following equation with reference to the variable *t*, that is:

$$R = \sum_k \hat{p}_k^0 \hat{p}_{-k}^1 e^{ikt} = maximum. \tag{2.16}$$

Having obtained *t*, the mean celerity $\bar{c}$ between the two points is derived as $\bar{c} = x_1/t$. From a physical point of view, this proves the validity of Eqs. (2.14) and (2.15) when, assuming the homogeneity of the pressure field that means the pressure fields have the same spectra, one obtains $\hat{p}_k^0 = \hat{p}_k^1$. Obviously, the values of the mean celerity in longitudinal and transversal directions must be assumed equal to: $\bar{c}_x = \frac{\xi}{t}$ and $\bar{c}_y = \frac{\eta}{t}$ that depends on the pivot point position in the hydraulic jump and by the length of the separator vectors ξ and η.

Here, the applicability of the Taylor hypothesis is checked experimentally. For three Froude numbers, Fig. 8a shows the comparison of the longitudinal spatial correlation as measured and as derived from the auto-correlation function by use of a proper value of celerity of propagation of pressure fluctuation aimed at obtaining a best fit. From the figure one can observe:

1. The comparison of the measured spatial correlation with the one made by auto-correlation show the overall similarity in shape and congruence in values.

2. The longitudinal correlation structure is well represented, at least up to the first zero crossing point, that is, in the region of most relevance for the computation of the Ω coefficient.

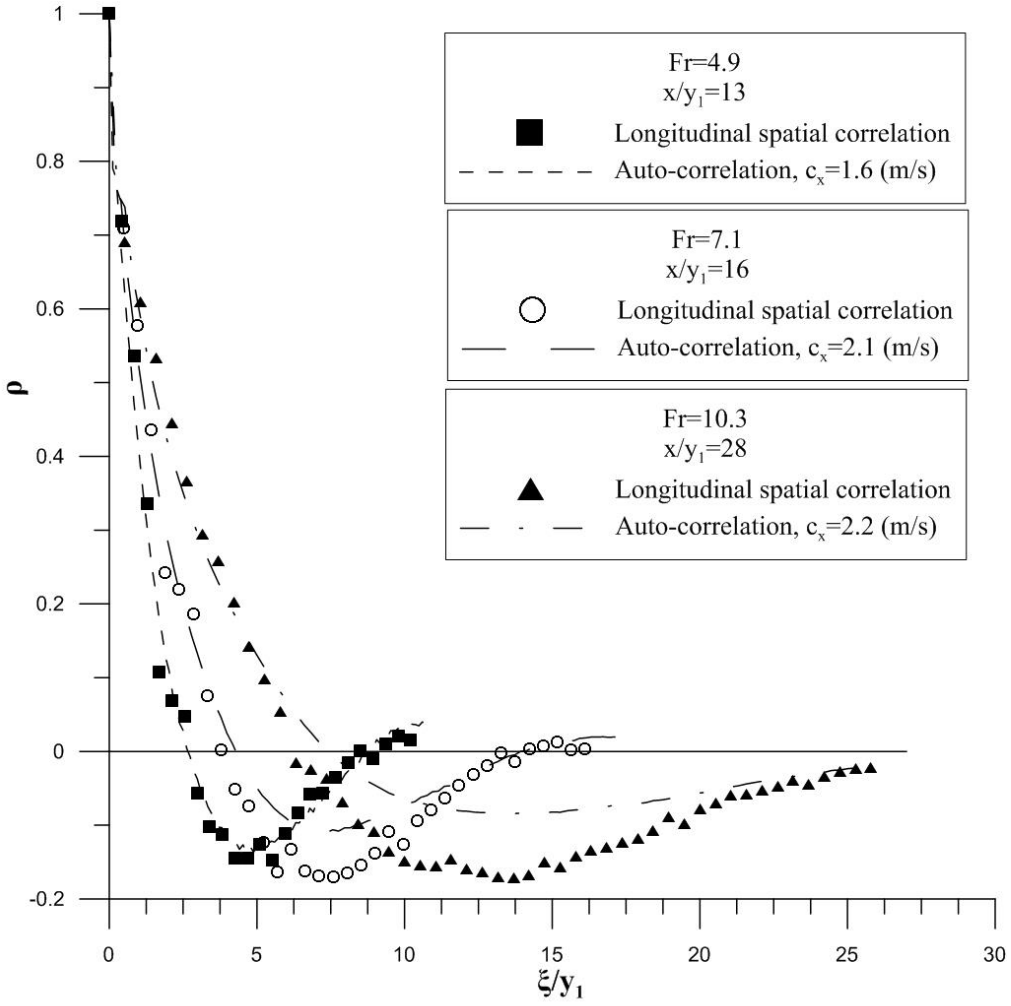

a)

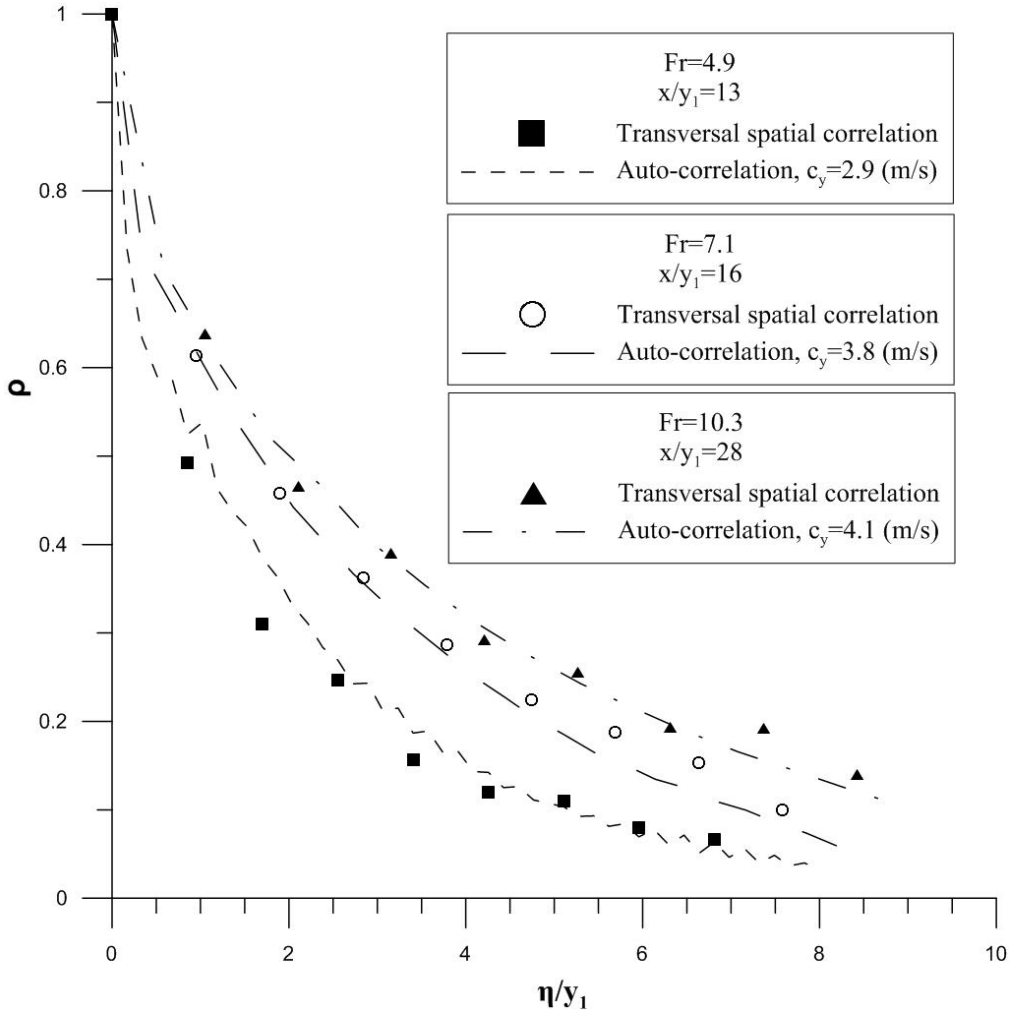

b)

Fig. 8: Comparison of a measured spatial correlation and spatial correlation made by using celerity in for Fr = 4.9, 7.1 and 10.3 **a)** Longitudinal direction **b)** Transversal direction

Some discrepancies can be found for distances larger than 8 – 10 times y_1. Past the first zero crossing point, the correlation function presents small values with some degree of variability, also in the comparison among literature data from different experiments (e.g. Abdul Khader and Elango 1974; Lopardo and Henning 1985; Vasiliev and Bukreyev 1967; Fiorotto and Rinaldo 1992b).

However, hydraulic jump stilling basins are typically made up of multiple concrete slabs separated by construction joints and the length of each slab is smaller than 10 – 12 m (this maximum length of the slab between the expansion

joints is needed in order to avoid the crack problem in the slab due to the retreat of the concrete and thermal effect) while y_1 is of the order of 1 m, so that the maximum ratio between slab length and the hydraulic depth at jump toe can be considered smaller than 10. In this context, the Taylor's hypothesis can be applied assuming a celerity value constant in every direction depending only by the pivot point distance from the hydraulic jump toe. In order to reproduce the pressure field beneath hydraulic jump accurately, the distance between measurement points is of the order of 8 times y_1 along the flow direction. Fig. 8b shows the measured transversal spatial correlation with the one made by single point auto-correlation using proper values of celerity for three different Froude numbers. The comparison in the transversal direction is always satisfactory and shows the accuracy of the Taylor hypothesis in order to evaluate the spatial correlation structure.

In Fig. 9, the behavior of the celerity c_x measured at different points, dimensionless with initial velocity u_1 is shown with respect to dimensionless distance x/y_1. The values of celerity in this figure are computed according to eq. (16) where x_1 is the distance between two taps in the surroundings of the measurement point x. From this figure one can note:

1. At a constant Froude number, longitudinal celerity values do decrease while the distance of the pivot point from the toe of the jump increases.
2. In the case of similar Froude number, the values of c_x/u_1 are in agreement with the data of Wang et. al(1984).
3. The comparison between the values of the longitudinal celerity and u_m, where u_m is the maximum velocity in the shear layer at different points downstream of the jump toe, shows a similar decay and strong relation among them.

Fig. 9 shows the relationship between point celerity and maximum velocity at different distance x/y_1. From the figure one can note that the celerity is practically equal to the maximum velocity in the shear layer velocity profile close to the bottom with reference to the data of Rajaratnam (1965). For the application of the Taylor hypothesis one must evaluate the mean celerity along

a distance starting from pivot point that is the separating vector. This celerity is close to the maximum flow velocity, as evaluated at the pivot point.

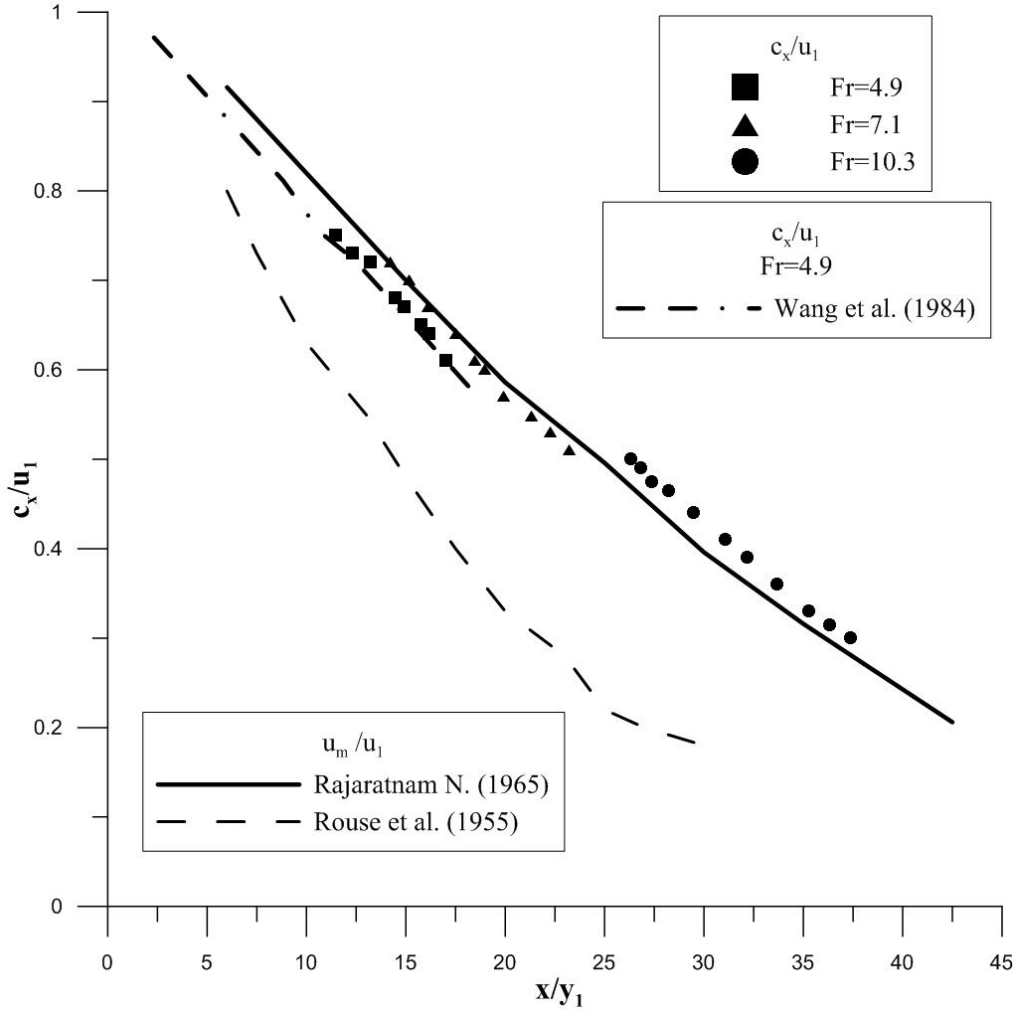

Fig. 9: c_x/u_1 versus x/y_1 for different Froude numbers

The analysis of the mean celerity $\bar{c}$ using Eq. (2.16), at changing distance from the pivot point, is performed in Fig. 10. Here, the variation of the longitudinal mean celerity $\bar{c}_x$ and transversal mean celerity $\bar{c}_y$ normalized by u_m at each pivot point along the hydraulic jump region is summarized. Due to the strong relation between celerity values and maximum velocity under the hydraulic jump, as shown in Fig. 9, the values of $\bar{c}_x/u_m$ and $\bar{c}_y/u_m$ lie on linear lines. In the longitudinal direction the values of $\bar{c}_x/u_m$ do decrease, while the distance from the pivot point increases. The rate of decrease is about a 10% for x/y_1 and it is

due to the non-homogeneity of the flow field in the longitudinal direction. Due to small variation of the value of $\bar{c}_x/u_m$the linear equation $\bar{c}_x/u_m$ = -0.02ξ/y_1 +1.1 can be used to computed the values of the longitudinal mean celerity at different distances from the toe of the jump, knowing the values of maximum velocity at each pivot point in the hydraulic jump zone. In the transversal direction the values of $\bar{c}_y/u_m$ do not change when the distance from the pivot point increases, that is due to the homogeneity of the flow field in the transversal direction. The linear equation $\bar{c}_y/u_m$ = 1.83 is proposed to estimate the values of the transversal mean celerity.

In this way, using Rajaratnam (1965) data to evaluate the velocity at a pivot point (Fig. 9), the linear equations shown in Fig. 10 allow to compute the values of the mean celerity.

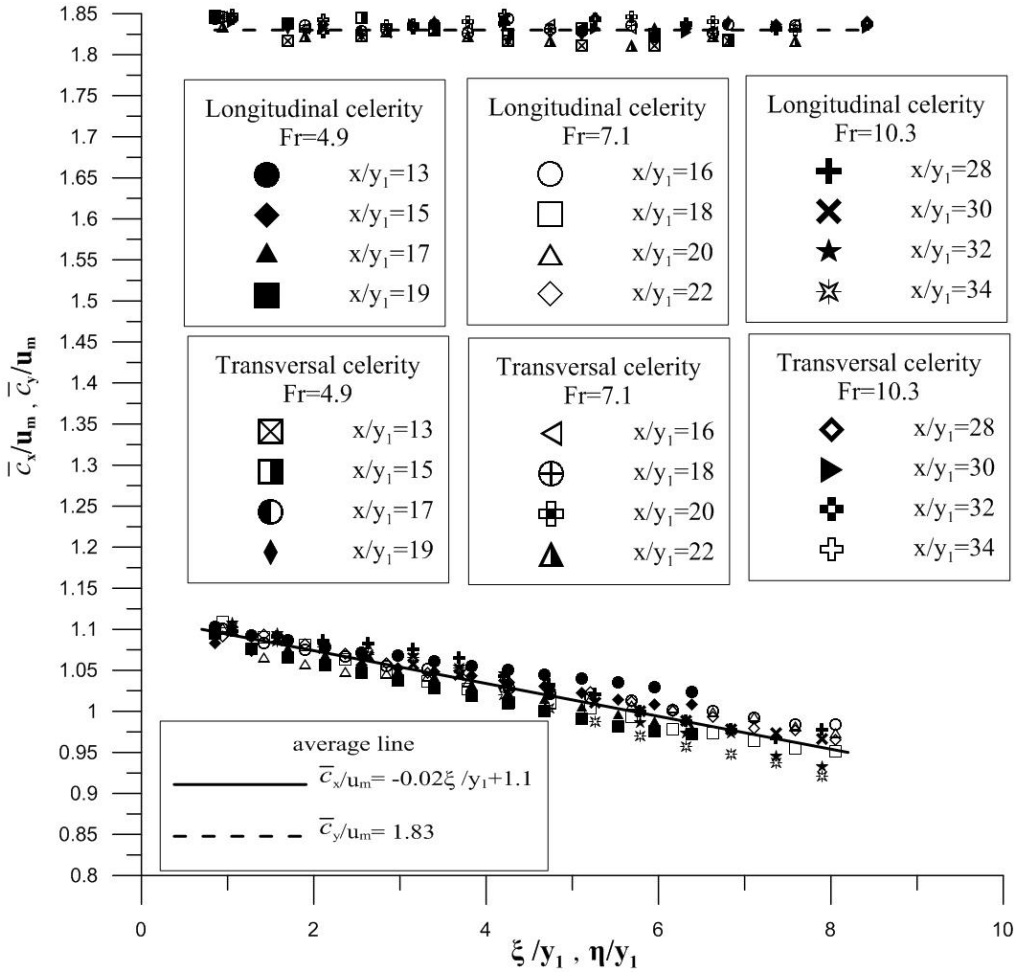

Fig. 10: $\bar{c}_x/u_m$ - $\bar{c}_y/u_m$ versus ξ/y_1 - η/y_1 for different distances from toe of the jump and different Froude numbers

Since the estimation of the maximum velocity at each pivot point under the hydraulic jump could be a difficult task, for design purpose the values of the $\bar{c}_x$ and $\bar{c}_y$ normalized with initial velocity u_1 respect to the dimensionless distance from the pivot point for different Froude numbers of the incident flow and different distance from the toe of the jump are shown in Fig. 11 and Fig. 12 respectively. These values are computed using Eq. (2.16) within the slab size. From Fig. 11, one can observe that, at constant Froude number, the values of the mean celerity do decrease when the values of x/y_1 increase, Because with reference to the Fig. 9 a relationship between celerity and velocity is highlighted, decreasing the velocity decreases the celerity. The velocity decreases when x/y_1 increase. Due to the small reduction of mean celerity when increasing the distance from the pivot point, one can consider an average of these values for each dimensionless distance x/y_1. The analysis of Fig. 12 shows that, at constant Froude number, the values of the mean celerity in the transversal direction do decrease when the distance from the toe of the jump increases.

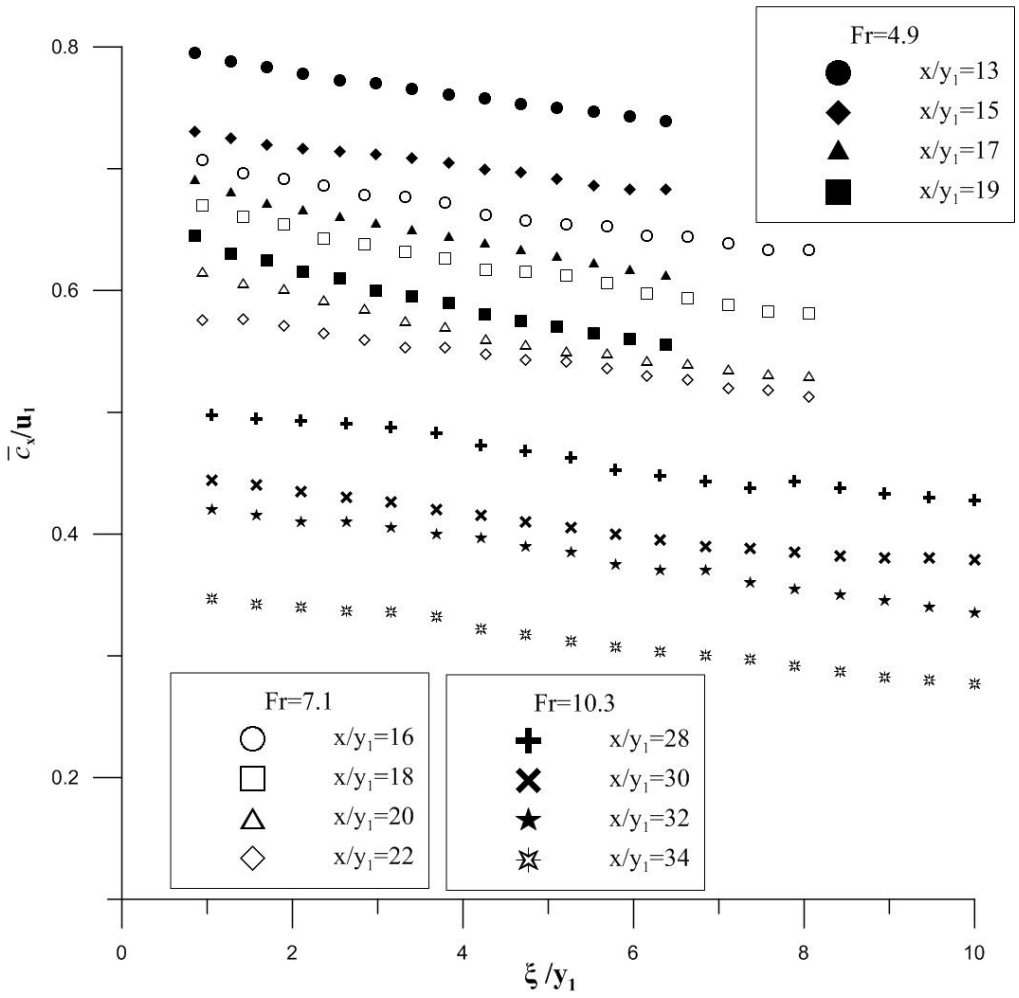

Fig. 11: $\bar{c}_x/u_m$ versus ξ/y_1 for different distances from toe of the jump and different Froude numbers

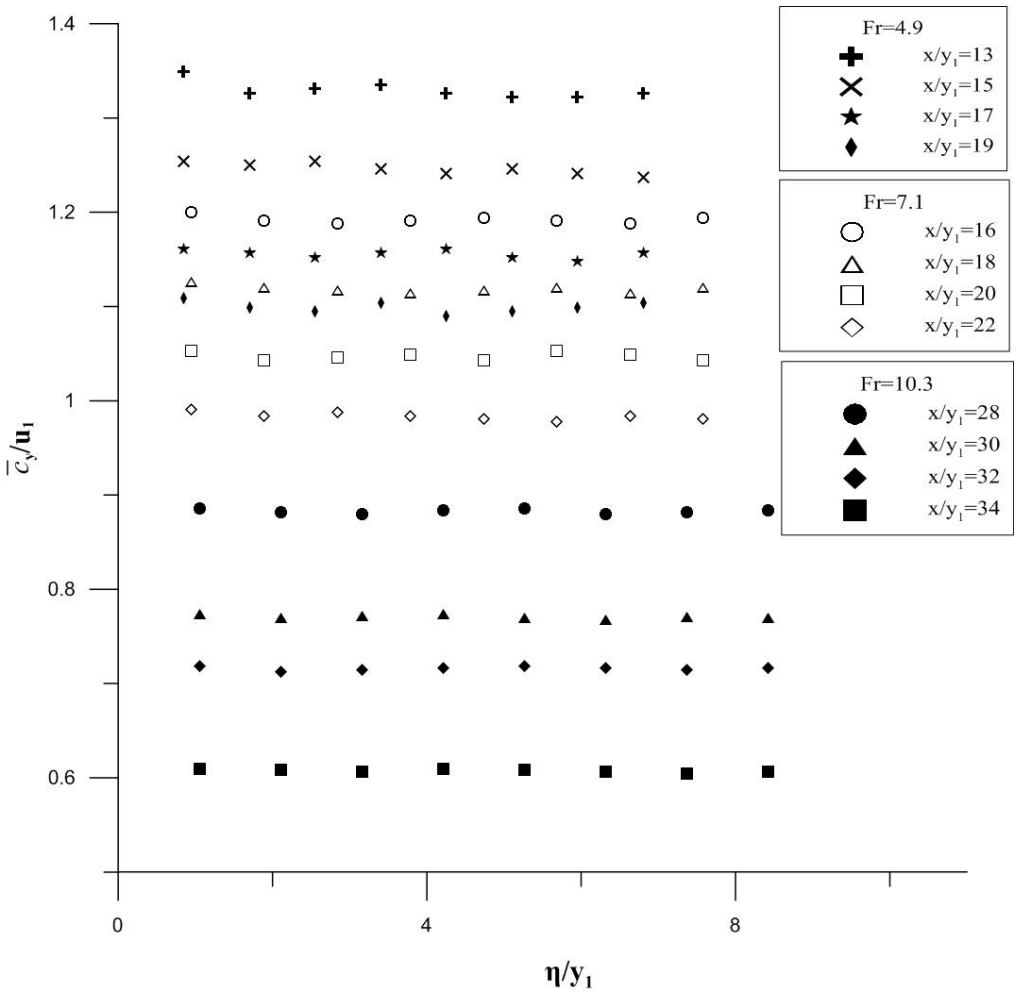

Fig. 12: $\bar{c}_y/u_m$ versus η/y_1 for different distances from toe of the jump and different Froude numbers

Based on taps arrangement, the mean celerity for oblique directions can be computed using Eq. (2.16). The same procedure, as presented for the transversal and longitudinal directions, is used to assess the mean celerity along an oblique direction. The average values of the mean celerity $\bar{c}_\alpha$, dimensionless with the initial velocity, as a function of the incidence angle, as evaluated for different distances from the toe of the jump are reported in Figs. 13 to 15, at changing Froude numbers. The solid curves have been obtained using the following function:

$$\bar{c}_\alpha/u_1 = \sqrt{(\bar{c}_x/u_1 \cos\alpha)^2 + (\bar{c}_y/u_1 \sin\alpha)^2} \qquad (2.17)$$

From the Figures one can note that the solid curves well interpolate the experimental points.

From a practical point of view, when mean celerity is known, as shown in Figs. 13 to 15, the measurement of single point fluctuating pressures on the slab center allows to define all the parameters needed for slab stability analysis. In fact, the pressure coefficients c_p^+ and c_p^- are directly obtained from extremes out of a long acquisition time series, significantly larger than the expected flood duration when scaled according to Froude similarity.

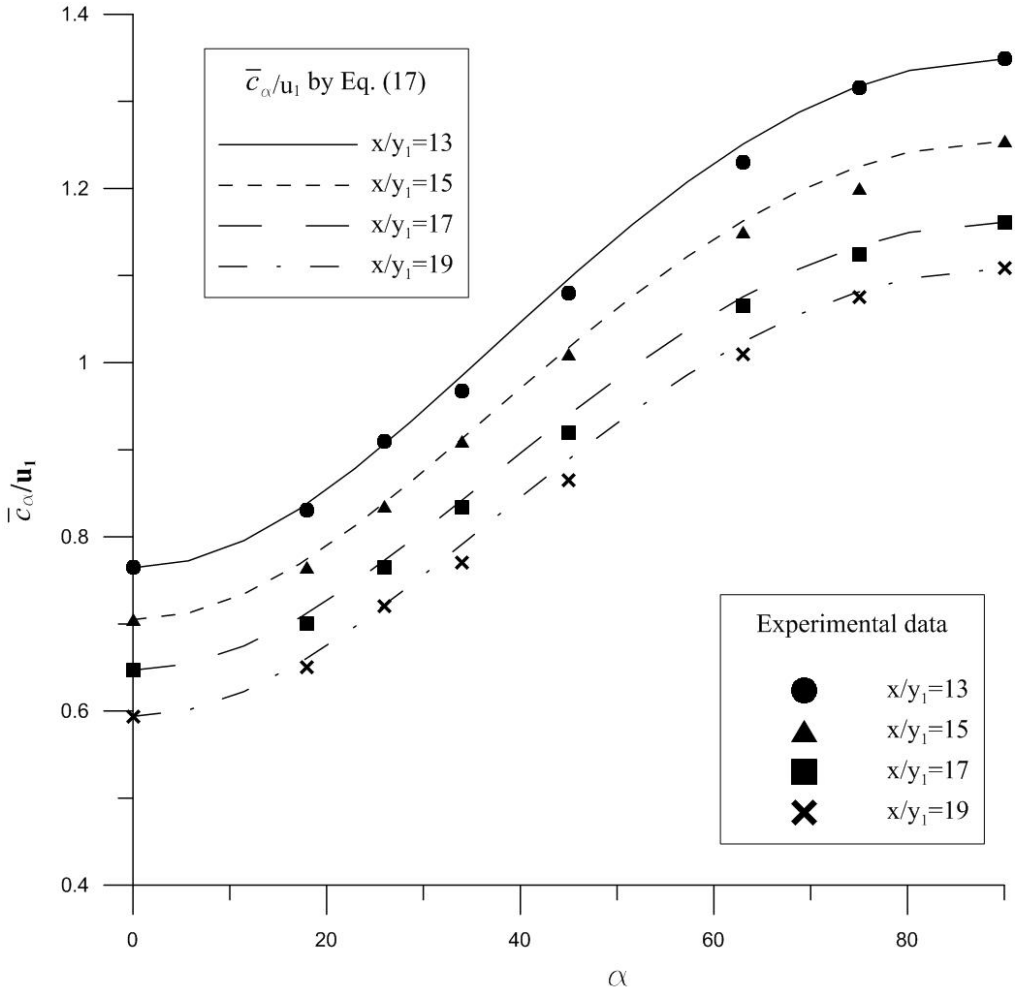

Fig. 13: Values of $\bar{c}_\alpha/u_1$ for different angles and distance from the toe of the jump at Froude number 4.9

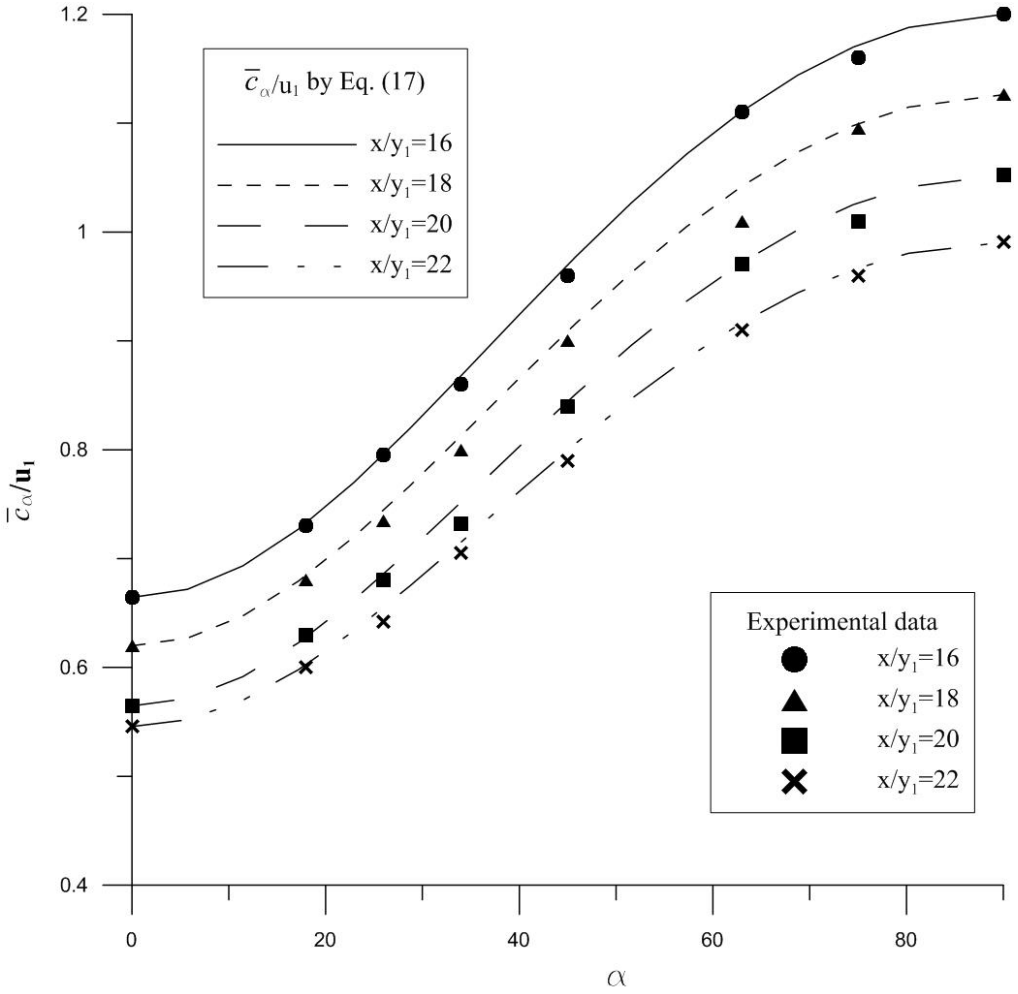

Fig. 14: Values of $\bar{c}_\alpha/u_1$ for different angles and distance from the toe of the jump at Froude number 7.1

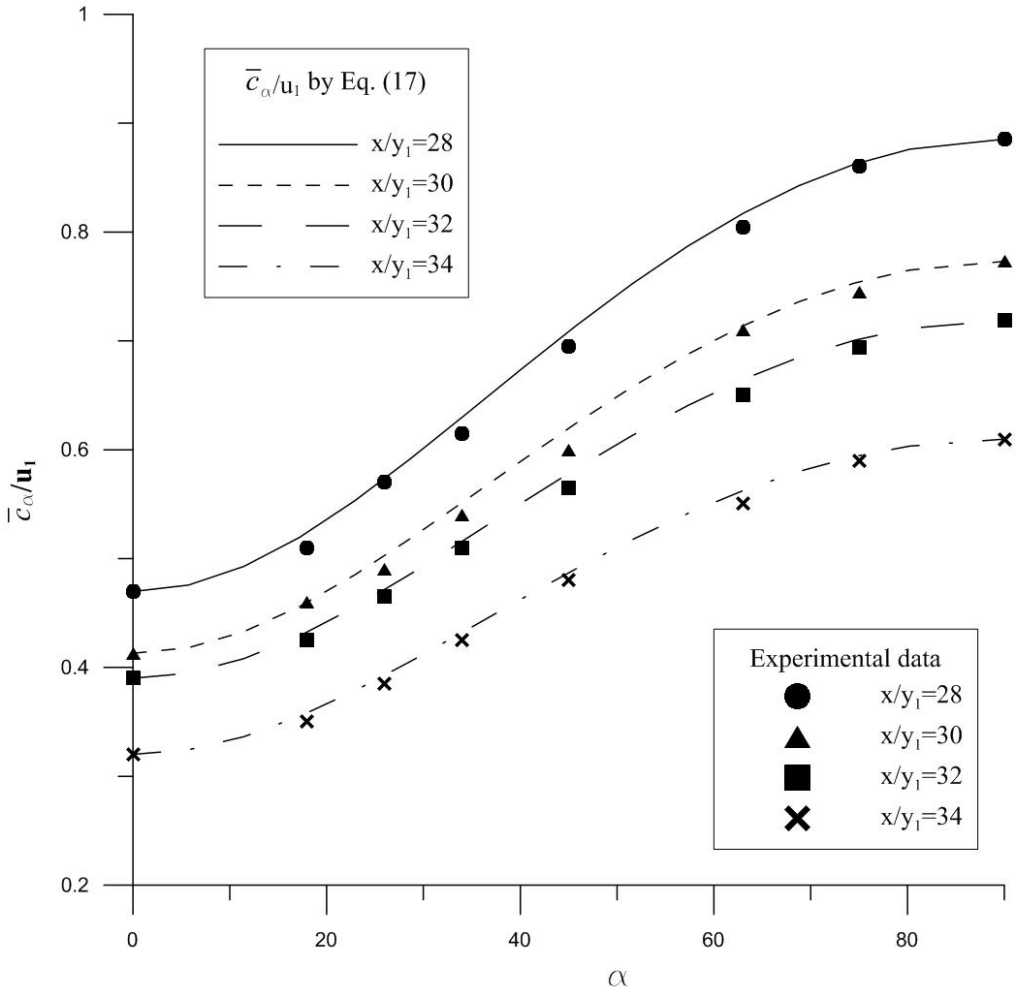

Fig. 15: Values of $\bar{c}_\alpha/u_1$ for different angles and distance from the toe of the jump at Froude number 10.3

Eq. (2.17) is proposed to obtain the value of the mean celerity in any direction $\alpha = arctan\ (\eta/\xi)$. Via the Taylor hypothesis, when $\bar{c}_\alpha$ is known, the spatial correlation function can be computed as:

$$\rho(x,\xi,0,\eta,0) = \frac{1}{\sigma_p^2}\sum_k \hat{p}_k \hat{p}_{-k} e^{ik\sqrt{\xi^2+\eta^2}/\bar{c}_\alpha} \tag{2.18}$$

Eq. (2.18) allows to compute the Ω^* and Ω coefficients using the single point pressure measurements.

2.5 Slab stability analysis via the Taylor hypothesis

The findings of the present study can be used in practical applications. The goal of the study is to compute the Ω coefficient, which is required in the evaluation of slab thickness, using the Taylor hypothesis via single point pressure acquisition. To the scope, the accuracy of the Taylor hypothesis is examined by comparing the values of the Ω coefficient, as computed by the present theoretical approach, with the results of Bellin and Fiorotto (1995), where a direct experimental evaluation was performed.

To reproduce the results by Bellin and Fiorotto (1995), it must be noted that, in their experiments, pressure propagation occurs in a thin water film underneath the slab. In these conditions, the propagation equation is the Laplace equation that can be solved in spectral terms via a finite difference scheme (Fiorotto and Caroni 2014). The boundary conditions consist in posing $\hat{p}_k$ = 1 at the $k1$ location along the slab boundary and $\hat{p}_k$ = 0 at the other ones. As a solution, the terms $\alpha^*_{k,k1,i}$ in Eq. (2.4) can be computed.

From direct at-point pressure measurements at the slab center, the spectral components $\hat{p}_k$ are derived by using the F.F.T. algorithm. Hence, the pressure terms in Eq. (2.4) can now be derived by the relationship:

$$\hat{p}_{k,k1}\hat{p}_{-k,k2} = \hat{p}_k\hat{p}_{-k}e^{ik\sqrt{\xi^2+\eta^2}/\bar{c}_\alpha} \tag{2.19}$$

where (ξ, η) is the separation vector between points $k1$ and $k2$, with distance $\sqrt{\xi^2+\eta^2}$ and angle α = arctan(η/ξ) respect to the mean flow direction.

The pressure celerity along the flow and the transversal directions can be easily extracted from Fig. 11 and Fig. 12 respectively, when eq. (2.17) gives the celerity in any other direction. In this way, all terms in Eq. (2.4) are computable and the Ω coefficient, can be derived for any slab size in the range of the Froude numbers here explored.

The comparison between the Ω coefficients, as computed from Eq. (2.4) using the Taylor hypothesis, is in a good agreement with the ones of Bellin and Fiorotto (1995), as shown in Figs. 16 and 17. In the present study, the physical phenomena was simulated numerically while in the Bellin and Fiorotto (1995) the results are related to the direct force measurement.

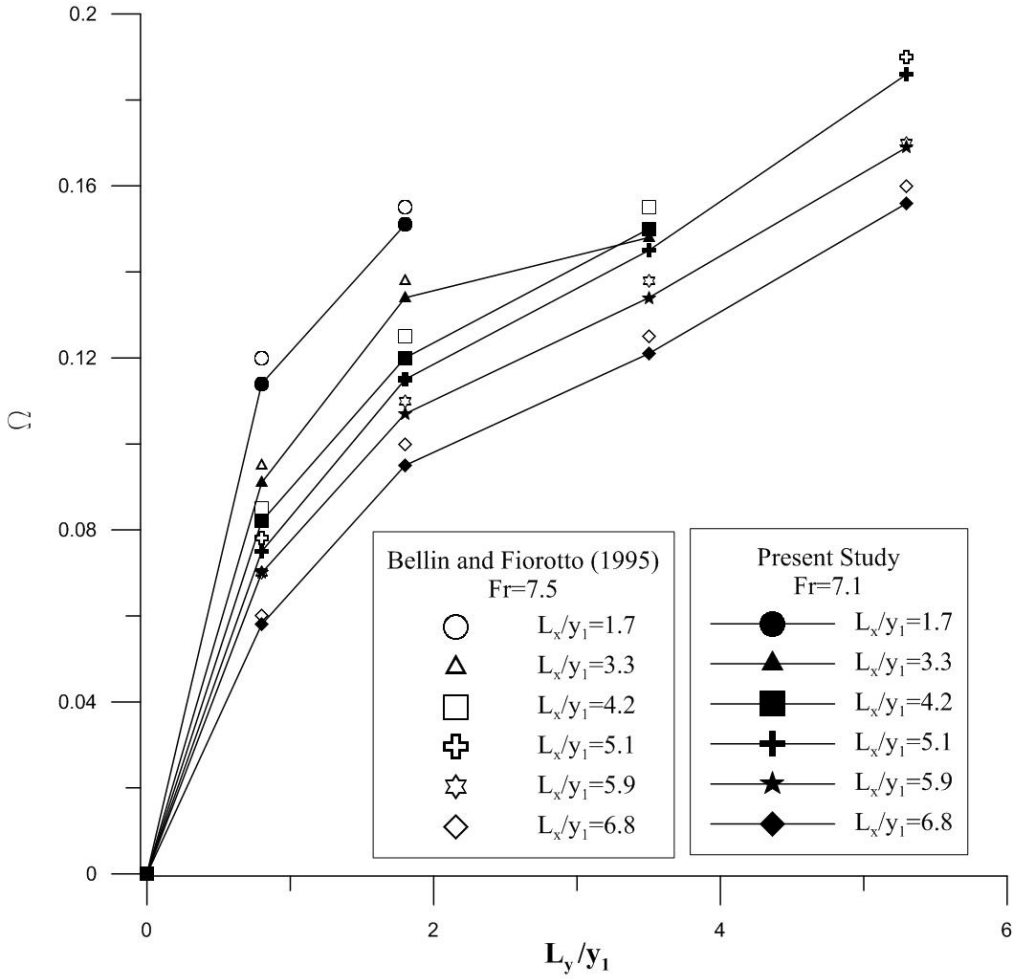

Fig. 16: Uplift coefficient Ω computed by Eq. (4) for Froude number 7.1

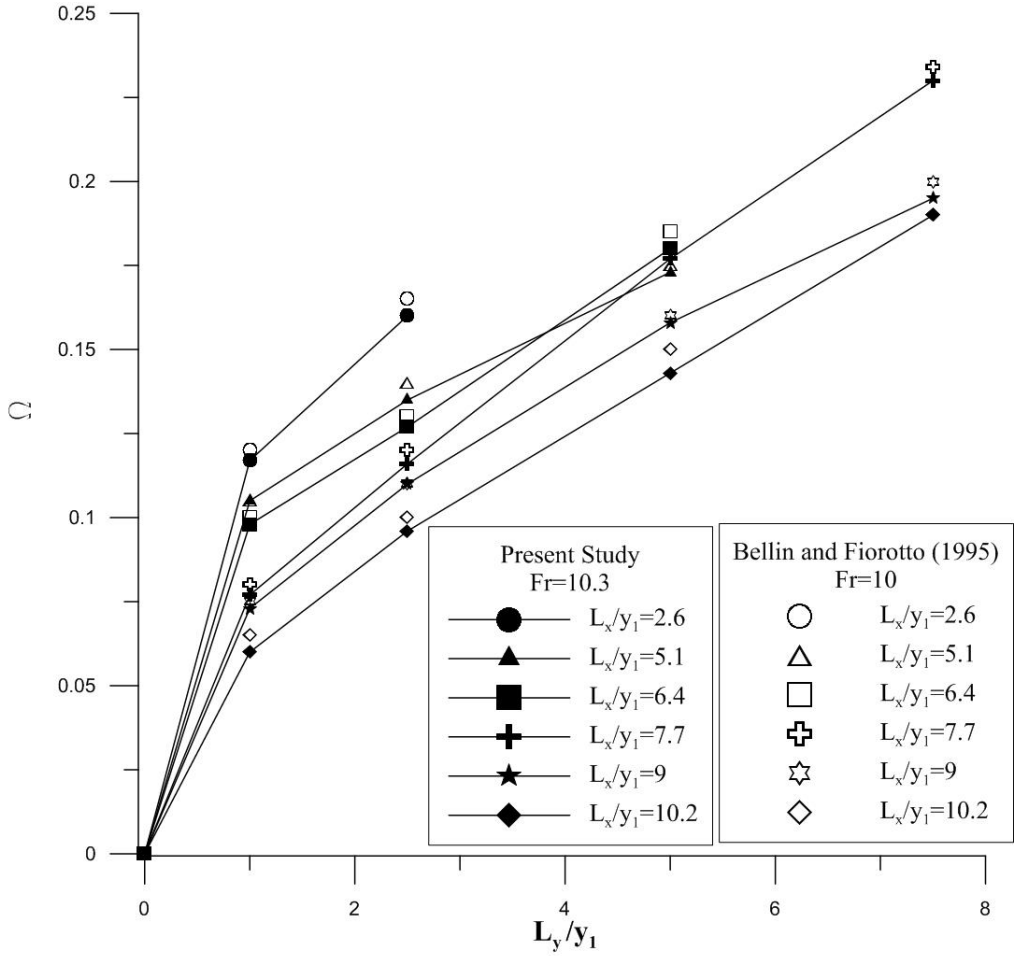

Fig. 17: Uplift coefficient Ω computed by Eq. (4) for Froude number 10.3

The difference between the experimental and computed values of Ω results is less than 3% and the standard deviation of the errors is equal to 1.5%, so that, from a statistical point of view, a maximum error of 6% can be assumed; this figure lies in the range of the expected measurement error in so complex experimental setup and it is felt unimportant with reference to real life applications, where a proper safety coefficient must be applied, as common.

In the case of sealed joints, the reduction factor Ω^* can be computed via Eq. (2.3) that corresponds to the first term of Eq. (2.4). Thus, the validation of the present approach in computing the Ω coefficient validates also its suitability

when computing the Ω^* coefficient, because the evaluation of the α^* coefficients in the second and third term of Eq. (2.4) is independent of the pressure field.

2.6 Design example

For the purpose of illustration the design of a stilling basin with unsealed joints is presented in the following. The depth and velocity of the incident flow are assumed equal to 1.82 m and 30 m/s, respectively. The resulting Froude number is 7.1. The stilling basin is built with 10 m width and 4 m long concrete slabs. so $l_x/y_1 = 6.6$ and $l_y/y_1 = 2.1$. The maximum c_p^+ and c_p^- values are assumed equal to 0.5 (Fiorotto and Rinaldo 1992b). By measuring the pressure at a point in the center of slab, the auto-correlation of the pressure can be computed. Using the Figs. 11 and 12 the mean celerity values in the longitudinal and transversal direction are found. From Eq. (2.17) the values of the celerity in all the directions can be computed and then Eq. (2.18) gives the whole spatial correlation function under the hydraulic jump region. By using the Eq. (2.4) we obtain $\Omega = 0.1$ (Fig. 16). The equivalent thickness of the lining is given by Eq. (2); assuming the ratio $\gamma(\gamma_s-\gamma)$ equal to 0.66 we obtain $s \sim 3$ m. It should be noted that in the presence of the baffle blocks in stilling basins the spatial statistical homogeneity of the flow field is lost and the Taylor hypothesis can not be applied. It is noteworthy that application of physical model results to prototype conditions in hydraulic jump does not deserve attention, with reference to air concentration. The consideration about the air effect on the pressure fluctutions under the hydraulic jump could not be found in litreture. From Fig. 1 in Chanson (2007) and the study of Castro and Hager (2009) one can see that the effect of the air is mostly in the roller of the jump and does not affect significantly the pressure fluctuations under the hydraulic jump, on the contrary the air effect in important for both nappe jets (e.g. Castillo et al., 2014b) and ski jump jets (e.g. Pfister et al., 2014; Schmoker et. al., 2008). This is not only with reference to the mean dynamic pressure, but also for the fluctuating pressures that in some cases could be larger respect to the unaerated condition typically in physical scale models.

2.7 Conclusions

In this chapter the evaluation of lining stability under hydraulic jump is investigated. The study was carried out experimentally, providing a data set suitable to test the Taylor hypothesis, whose application can greatly simplify the evaluation of the spatial correlation structures, needing only single point pressure measurements. The following conclusions can be drawn from the present study:

- At constant Froude number, the values of the mean celerity in the longitudinal direction do decrease when the distance from the pivot point increases, which is due to the non-homogeneity of the flow field in the flow direction.
- At constant Froude number, the transversal mean celerity values do not change while the distance from the pivot point increases, which derives from the homogeneity of the flow field in the cross-stream direction.
- The analysis of the experimental results shows that the at-point celerity of propagation of pressure fluctuations in the longitudinal direction is congruent both in values and shape with the maximum velocity in the flow direction. Based on this strong relation $\bar{c}_x/u_m$ = -0.02ξ/y_1 +1.1 for longitudinal celerity and $\bar{c}_y/u_m$=1.83 for transversal celerity are proposed as general equations for computing the celerity at each point in the hydraulic jump region, knowing the maximum velocity profile under the hydraulic jump at the pivot point. This velocity can be derived from Rajaratnam (1965).
- The mean celerity in a general oblique direction can be derived via Eq. (2.17) that shows the mean celerity to follow a quadratic behavior with angle α.
- The Ω coefficients, as computed in the present study by use of the Taylor hypothesis, show a good agreement with the ones computed by direct experimental evaluation by Bellin and Fiorotto (1995) and verify the validity of the Taylor hypothesis in this context.

The approach presented in this chapter avoids the rather awkward devices for direct assessment of slab stability and can be useful in the structural design of stilling basin linings in the case of both sealed and unsealed joints.

This chapter is published in Journal of Hydraulic Engineering (ASCE).

Barjastehmaleki, S., Fiorotto, V., and Caroni, E. (2016). "Spillway Stilling Basins Lining Design via Taylor Hypothesis." *J. Hydraul. Eng.*, 10.1061/(ASCE)HY.1943-7900.0001133.

3

Pressure under slabs

3.1 Introduction

The analysis of propagation of the pulsating pressures underneath the slab over a thin film layer of water was developed by Fiorotto and Rinaldo (1992a) using transient flow and seepage models. Liu and Li (2007) studied the pressure propagation within the joints in a one dimensional (1D) thin film approach using three different models, namely: (1) transient flow, (2) seepage, and (3) vibrating flow. Fiorotto and Caroni (2014) presented a theory, based on transient seepage that unifies the three models discussed by Liu and Li (2007) and is capable to account for the effect of finite thickness porous media underside the slab. This is the case where slabs lie on the bedrock with an interposed drain in gravel or an important alluvial layer. Weirs of run-of-river power plants, concrete dams founded in bedrock underneath an important alluvial layer and, generally, rock-fill and earth dams are the examples of this case.

While the previous work (Fiorotto and Caroni, 2014) in 2D highlighted the importance of finite thickness foundation layers in evaluation of the pressure underneath the slab, in order to have an applicable design criteria a new 3D model based on unsteady flow analysis of seepage through porous media is proposed in this chapter. By using this model, the pulsating pressure propagation underneath the slab is evaluated considering the three dimensionality of the flow under the slab for different size and shape of the slab as well as different characteristics and thickness of foundation layers and the effect of width of slab is pointed out. The presented 3D model is able to overcome the concept of thin film that was used as an approximation in physical model in previous studies, being applicable in a realistic way to finite thickness

mediums underneath the slab. This is not only the case where slabs lie on the bedrock with an interposed drain in gravel or an important alluvial layer, but the case where the slabs lie directly on the compact rock also. This is understandable taken into account the seepage flow into the roughness in the interface between rock and slab.

The uplift force is computed using experimental data by Barjastehmaleki et. al (2015), related to the case of hydraulic jump in stilling basins. The results are compared to the data of Bellin and Fiorotto (1995) in which direct experimental evaluation of the uplift force, in thin film underpressure propagation, are reported; and with the 2D model (Fiorotto and Caroni, 2014). The comparison shows the importance of 3D model.

3.2 3D unsteady seepage

Transient flow, seepage and vibrating flow models were analyzed by Fiorotto and Caroni (2014) and the advantage of the unsteady seepage model was highlighted. Particularly, it was shown by Fiorotto and Caroni (2014) that the unsteady seepage analysis is more suitable to interpret the physical phenomenon in respect to transient flow and it makes it possible to consider finite thickness saturated layers.

It should be note that the seepage approach presents limits of applicability, considering that the Darcy law is established for steady-state flows (de Marsily 1986). In unsteady flow conditions, and particularly in the case of an oscillating fluid motion, a transient term must be added to the Darcy law (de Marsily 1986), having the same role in the equation as the external forces. Considering also the tortuosity parameter T^* according to Bear and Sorek (1990), Krylov et al. (1996), the transient state seepage equation is:

$$U = -\frac{K}{g\rho_w}\left(\text{grad}\, p + g\rho_w\, \text{grad}\, \mathcal{Z} - \frac{T^*\rho_w}{\phi}\frac{\partial U}{\partial t}\right) \tag{3.1}$$

where U is the seepage Darcian velocity, K is the Darcy permeability coefficient, ρ_w is water density, p the fluid pressure, $\mathcal{Z}$ is vertical elevation, ϕ

porosity and T^* is the tortuosity parameter. The role of the inertial term $\partial U/\partial t$ can be further analyzed by coupling Eq. (3.1) with the continuity equation

$$\mathrm{div}(\rho U) - \frac{S}{g}\frac{\partial p}{\partial t} = 0 \tag{3.2}$$

where S is the specific storage coefficient. By solving the system constituted by Eqs. (3.1) and (3.2) in the 3D case of a porous layer under the slab, one can obtain

$$K\left(\frac{\partial^2 p}{\partial x^2} + \frac{\partial^2 p}{\partial y^2} + \frac{\partial^2 p}{\partial \mathcal{Z}^2}\right) - \frac{KT^*S}{\phi g}\left(\frac{\partial^2 U}{\partial x \partial t} + \frac{\partial^2 U}{\partial y \partial t} + \frac{\partial^2 U}{\partial \mathcal{Z} \partial t}\right) = S\frac{\partial p}{\partial t} \tag{3.3}$$

Deriving Eq. (3.2) in time leads to the mixed derivative of the seepage velocity. By substituting the mixed derivative into Eq. (3.3) and neglecting nonlinear terms, the following expression can be drawn in terms of the piezometric head h:

$$K\left(\frac{\partial^2 h}{\partial x^2} + \frac{\partial^2 h}{\partial y^2} + \frac{\partial^2 h}{\partial \mathcal{Z}^2}\right) - \frac{KT^*S}{\phi g}\frac{\partial^2 h}{\partial t^2} - S\frac{\partial h}{\partial t} = 0 \tag{3.4}$$

To perform the unsteady seepage analysis in 3D, considering the length L_x and width L_y of the slab as well as the thickness Z of the sediment layer between the slab's lower face and bedrock, a numerical approach is carried out to solve the following equation. By substituting $x = L_x x'$, $y = L_y y'$, $\mathcal{Z} = Z\mathcal{Z}'$ and $h = Hh'$, where H is mean pressure head at slab extremities, into Eq. (3.4), a dimensionless equation is obtained

$$\left(\frac{\partial^2 h'}{\partial x'^2} + \frac{{L_x}^2\partial^2 h'}{{L_y}^2\partial y'^2} + \frac{{L_x}^2\partial^2 h'}{Z^2\partial \mathcal{Z}'^2}\right) - \frac{T^*S{L_x}^2}{\phi g}\frac{\partial^2 h'}{\partial t^2} - \frac{S{L_x}^2}{K}\frac{\partial h'}{\partial t} = 0 \tag{3.5}$$

By assuming the pulsating pressure head as $h'(x', y', \mathcal{Z}') = \sum_k \hat{h}_k(x', y', \mathcal{Z}')e^{ikt}$ Eq. (3.5) becomes

$$\left[\frac{\partial^2 \hat{h}_k(x',y',z')}{\partial x'^2} + \frac{{L_x}^2}{{L_y}^2}\frac{\partial^2 \hat{h}_k(x',y',z')}{\partial y'^2} + \frac{{L_x}^2}{Z^2}\frac{\partial^2 \hat{h}_k(x',y',z')}{\partial \mathcal{Z}'^2}\right] + k^2\frac{T^*S{L_x}^2}{\phi g}\hat{h}_k(x', y', \mathcal{Z}') - ik\frac{S{L_x}^2}{K}\hat{h}_k(x', y', \mathcal{Z}') = 0 \tag{3.6}$$

Substituting $a = \sqrt{g\phi/ST^*}$, $R = g\phi/KT^*$, $Z' = Z/L_x$ and $k' = kL_x/a$ into Eq. (3.6), where a is celerity and R is resistance factor, one first obtains

$$\left[\frac{\partial^2 \hat{h}_k(x',y',z')}{\partial x'^2} + \frac{{L_x}^2}{{L_y}^2}\frac{\partial^2 \hat{h}_k(x',y',z')}{\partial y'^2} + \frac{1}{Z'^2}\frac{\partial^2 \hat{h}_k(x',y',z')}{\partial \mathcal{Z}'^2}\right] + k'^2\hat{h}_k(x', y', z') - ik'\frac{RL_x}{a}\hat{h}_k(x', y', \mathcal{Z}') = 0 \tag{3.7}$$

that in finite difference form, reads

$$\frac{\hat{h}_k(i-1,j,m)+\hat{h}_k(i+1,j,m)-2\hat{h}_k(i,j,m)}{\Delta x'^2}+\frac{L_x{}^2}{L_y{}^2}\frac{\hat{h}_k(i,j-1,m)+\hat{h}_k(i,j+1,m)-2\hat{h}_k(i,j,m)}{\Delta y'^2}+$$

$$\frac{1}{Z'^2}\frac{\hat{h}_k(i,j,m-1)+\hat{h}_k(i,j,m+1)-2\hat{h}_k(i,j,m)}{\Delta Z'^2}+\left(k'^2-ik'\frac{RL_x}{a}\right)\hat{h}_k(i,j,m)=0 \qquad (3.8)$$

where *i,j,m* are mesh point indexed along the *x′*, *y′* and $\mathcal{Z}'$ direction, respectively, displaced at intervals $\Delta x'$, $\Delta y'$ and $\Delta \mathcal{Z}'$ in a computation domain $0 \le x' \le 1$, $0 \le y' \le 1$ and $0 \le \mathcal{Z}' \le 1$.

Eq. (3.8) forms the unsteady seepage model and defines the uplift contribution due to pressure transmission underneath slab joints in stilling basins. This comprehensive formulation summarizes all the propagation models that were analyzed by Liu and Li (2007). It can be noted that from Eq. (3.5), multiplying the right and left terms by $L_y{}^2/ L_x{}^2$, one obtains, for rectangular slabs with $L_x >> L_y$:

$$\left(\frac{\partial^2 h'}{\partial y'^2}+\frac{L_y{}^2\partial^2 h'}{Z^2\partial \mathcal{Z}'^2}\right)-\frac{T^* S L_y{}^2}{\phi g}\frac{\partial^2 h'}{\partial t^2}-\frac{S L_y{}^2}{K}\frac{\partial h'}{\partial t}=0 \qquad (3.9)$$

so that, the 3D model collapses into a 2D model with the characteristic length equal to L_y. This fact is true from a physical point of view because the seepage flow for $L_x \to \infty$ propagates only along *y* direction between the slab boundaries.

3.3 Computational field:

To solve Eq. (3.8) the boundary condition and mesh size must be assigned. Boundary conditions were set as follows: periodicity in *x* and *y* direction, impermeability in the foundation layer bottom $\mathcal{Z}$ direction and pulsating pressure at the slab joints. Eq. (3.4) is numerically solved for every dimensionless wave number $k' = kL_x/a$ and the pressure heads acting under the slab p_u is computed. By integration of these pressure heads along *x′* and *y′* in (0,1), the spectral components of the force due to under pressures are evaluated. Different mesh resolutions were tested, to cope for best performances in precision/computational time, obtaining grid dimensions $\Delta x'$, $\Delta y'$ and $\Delta \mathcal{Z}'$ equal to 0.05 as an optimum. The error in modulus of the spectral components of the force F'_K due to under pressures using smaller mesh size (0.005 and 0.0005) resulted lesser than 1%.

3.4 Results and discussion

Fig. 18 shows the resulting modulus of the force F'_K, that is the integral of the pressure acting under the slab computed according to Eq. (3.8), on the dimensionless wave number k' for different dimensionless resistance parameter RL_x/a and different shape of the slab L_x/L_y varying the relative thickness Z'. In Fig. 18 the results of modulus of the force F'_K in 3D case is compared with the 2D one (Fiorotto and Caroni, 2014). Fig. 18(a), for RL_x/a = 1, and Fig. 18(b), for RL_x/a = 4 compare the modulus of the force F'_K in the 3D case with L_x/L_y = 4 with the 2D one. From the figures one can note that:

1. In both Figures the comparison of the 3D case for a rectangular slab with 2D one shows the overall similarity in shape and congruence in values as expected with reference to Eq. (3.9). This proves that in the 3D case of a rectangular slab with L_x/L_y = 4 the pressure acting under the slab has the same pattern as the 2D case, changing L_x with L_y for sake of congruence between the two models. From a physical point of view, it can be noted that in the case of elongated slab, a 2D model can be used instead 3D model, considering the L_y as the characteristic length with a remarkable simplification in the computation.
2. In Fig. 18(a) a shift of the first peak value in F'_K toward lower dimensionless wave numbers with a reduction in peak values is observed. This fact is congruent with an increment of the dimensionless resistance coefficient and can be related to an increment in seepage pathline length, when increasing Z'; and
3. In the second case [Fig. 18(b)], a reduction in F'_K is shown at fixed k', again corresponding to an increment of the dimensionless resistance coefficient and can be related to an increment in seepage pathline length, when increasing Z' .

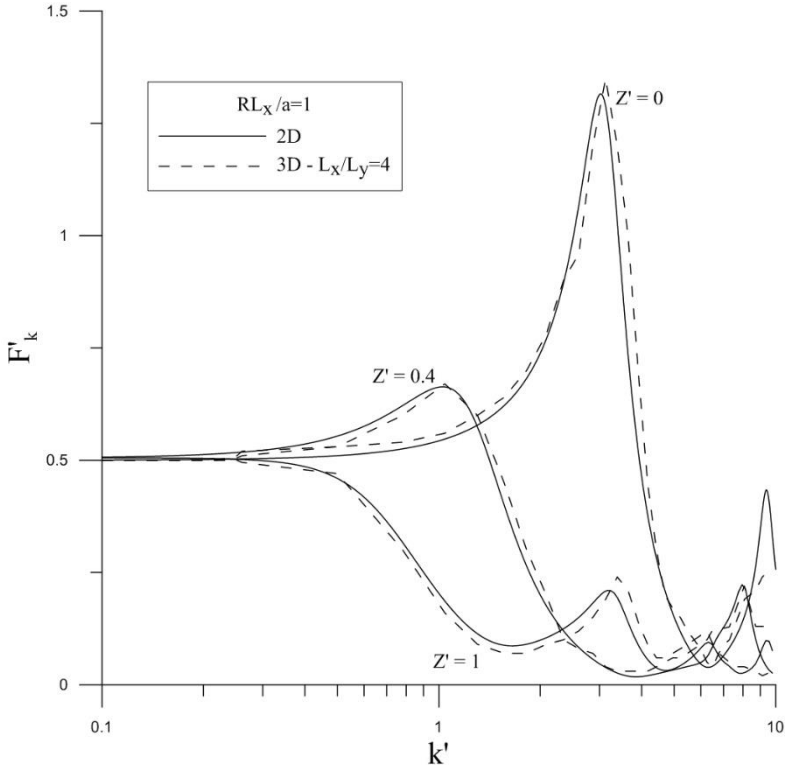
1.5
1
0.5
0
F'k
RLx /a=1
2D
3D - Lx/Ly=4
Z' = 0
Z' = 0.4
Z' = 1
0.1
1
10
k'

(a)

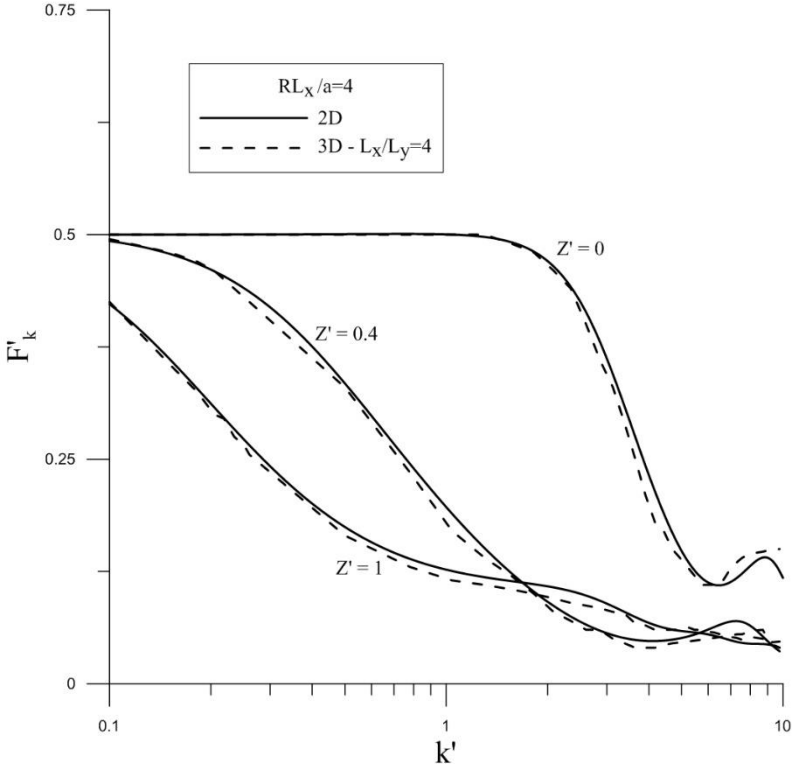
0.75
0.5
0.25
0
F'k
RLx /a=4
2D
3D - Lx/Ly=4
Z' = 0
Z' = 0.4
Z' = 1
0.1
1
10
k'

(b)

Fig. 18: Comparison of modulus of the underpressure total force F'_K on dimensionless wave number k' varying the foundation layer thickness Z' for 2D and 3D case: (a) $RL_x/a = 1$ and $L_x/L_y = 4$; (b) $RL_x/a = 4$ and $L_x/L_y = 4$

In Fig. 19(a) and 19(b), the modulus of the force F'_K in 3D case with $L_x/L_y = 1$ is compared with the 2D one for $RL_x/a = 1$ and $RL_x/a = 4$, respectively. The analyses of the Figures show that:

1. An increment in the values of the modulus of the force F'_K is observed in 3D case with a square slab ($L_x/L_y = 1$) respect to the 2D case in both Figures. This shows that in the square slab the pressure acting under the slab is bigger than the one in 2D case and highlights the importance of effect of transversal direction in this matter, which 2D model can not consider it. This can be justified comparing Eq. (3.9) with Eq. (3.5). The difference in the results is due to the effect of the first term in the parenthesis of Eq. (3.5) that considered the propagation of the flow along L_x; and
2. The results of 3D study in Fig 19(a) show a shift of the peak value in F'_k towards lower dimensionless wave numbers with respect to 2D case. In Fig. 19(b), an increment in F'_K at fixed k' is observed in 3D result in compare with the 2D in the range lower wave numbers that is of the most interest in the slab stability computation. Both these effects might be due to the increment of the pathline length in the foundation layer, respect the 2D case when increasing Z'.

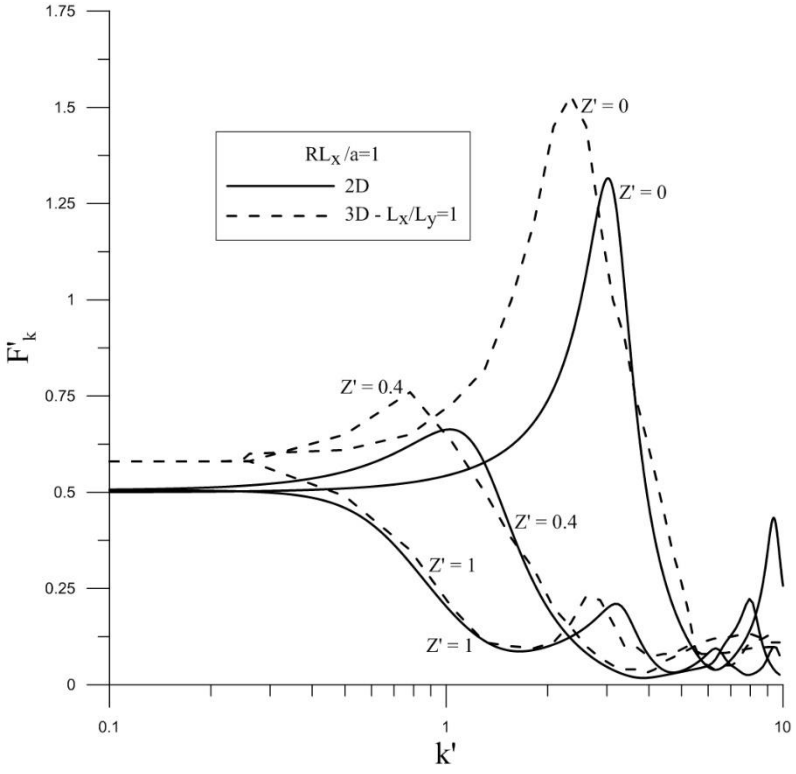
RL$_X$/a=1
2D
3D - L_X/L_y=1
Z' = 0
Z' = 0
Z' = 0.4
Z' = 0.4
Z' = 1
Z' = 1
F'_k
k'
1.75
1.5
1.25
1
0.75
0.5
0.25
0
0.1
1
10

(a)

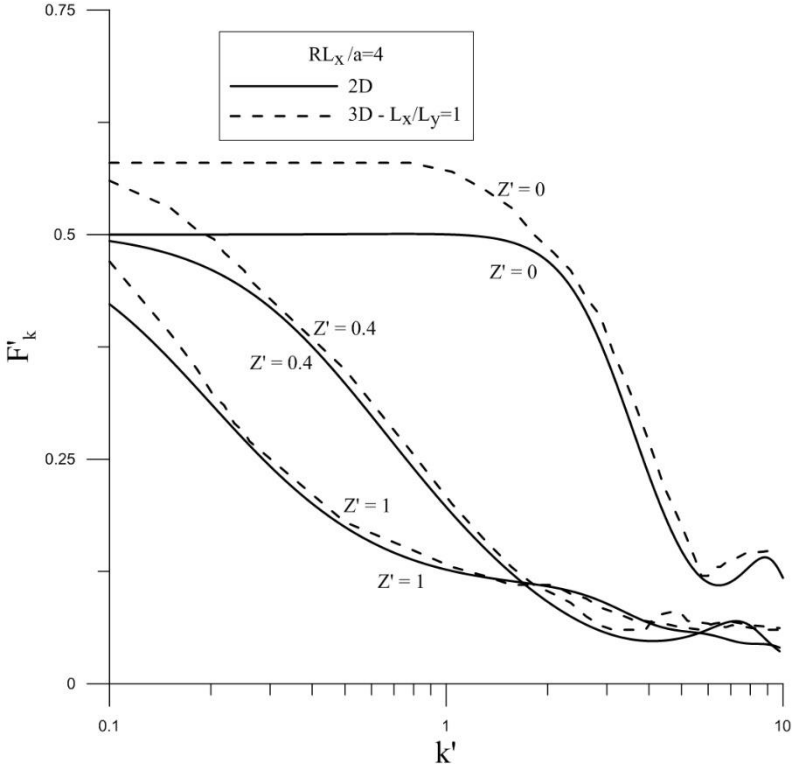
RL$_X$/a=4
2D
3D - L_X/L_y=1
Z' = 0
Z' = 0
Z' = 0.4
Z' = 0.4
Z' = 1
Z' = 1
F'_k
k'
0.75
0.5
0.25
0
0.1
1
10

(b)

Fig. 19: Comparison of modulus of the underpressure total force F'_K on dimensionless wave number k' varying the foundation layer thickness Z' for 2D and 3D case: (a) $RL_x/a = 1$ and $L_x/L_y = 1$; (b) $RL_x/a = 4$ and $L_x/L_y = 1$

Comparison of modulus of the underpressure total force F'_K on dimensionless wave number k' varying the foundation layer thickness Z' for 2D and 3D case: (a) $RL_x/a = 1$ and $L_x/L_y = 1$; (b) $RL_x/a = 4$ and $L_x/L_y = 1$

The comparison between Figs. 18 and 19 highlights the effect of the slab shape in the underpressure total force. The square slab increases the total force underpressure as it is highlighted by larger F'_K respect to the rectangular one. Furthermore, the square slab tends to bring peaks in F'_k towards lower wave numbers respect to the rectangular one, where the spectral components of the fluctuation of the pressures present larger energy rates (Fig. 1). These two facts concur to increase the uplift force in square slab condition. The first effect is underlined by the force underpressure variance also. With reference to Eq. (2.4) the force undepressure variance is

$$\sigma_U^2 = \frac{1}{N_b^2}\sum_k \sum_{i=1}^{N_s}\sum_{j=1}^{N_s}\sum_{k1=1}^{N_b}\sum_{k2=1}^{N_b} \alpha^*_{k,k1,i}\,\alpha^*_{-k,k2,j}.$$

Fig. 20 shows the variance of the pressure acting under the slab σ_U^2 with respect to the relative thickness Z' for different dimensionless resistance parameter RL_x/a and different shape of the slab L_x/L_y. From Fig. 20 one can observe that:

1. The value of the variance of the pressures underneath the slab does increase when the value L_x/L_y decreases at a constant thickness Z'; and
2. The value of the variance of the pressures acting under the slab does decrease when thickness Z' decreases at a constant value of L_x/L_y.

These considerations are congruent with the F'_K behavior reported in Figs. 4 and 5. From a quantitative point of view, according to Eqs. (2.2) and (2.4), increasing σ_U^2 results an increment in Ω and as a consequence in slab thickness s.

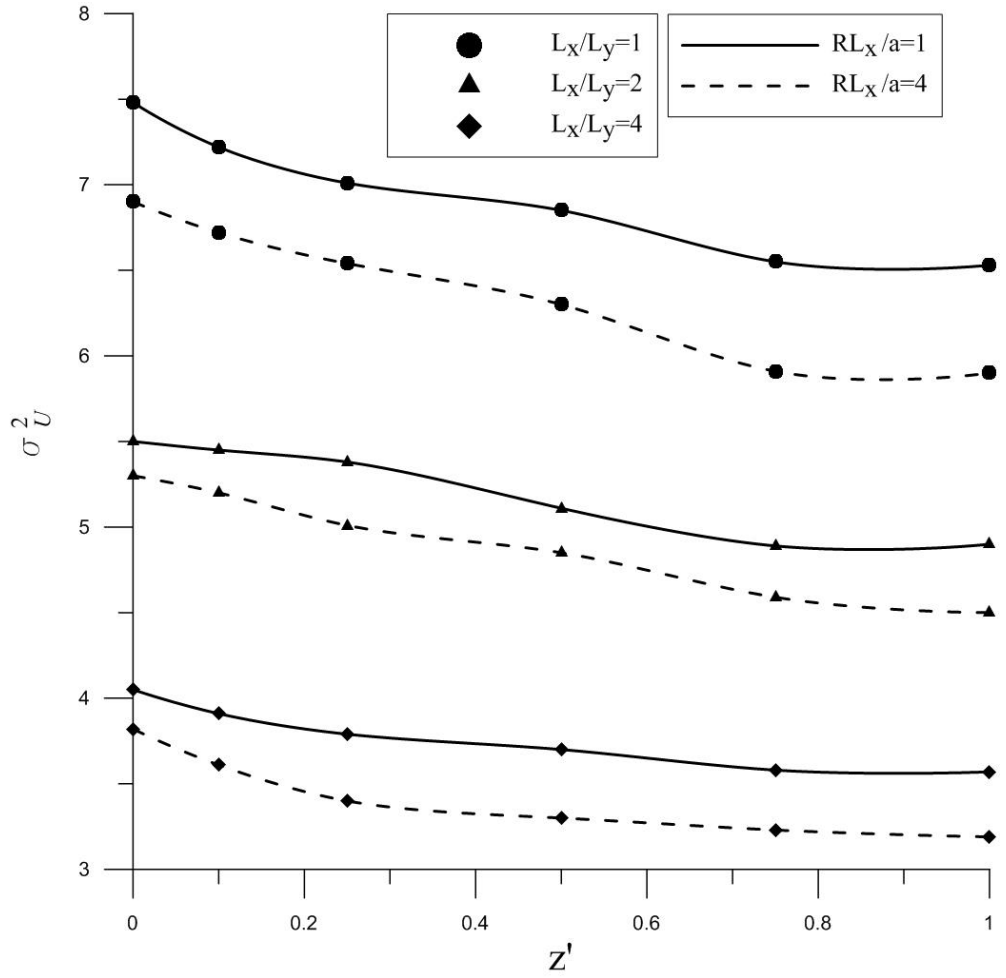

Fig. 20: The variance of the pressure acting under the slab σ_U^2 with respect to the relative thickness *Z'* for different dimensionless friction parameter RL_x/a and different shape of the slab L_x/L_y.

3.5 Stability Analysis of Protection Slabs

In the analysis of slab stability with unsealed joints, via Eq. (2.2), the reduction factor Ω plays a key role. From a physical point of view, the Ω coefficient takes into account the pressure distribution at the upper and lower slab surfaces (*p* and p_u in Fig. 1). In order to compute Ω using Eq. (2.4), the spatial correlation structure of the pressure fluctuations on the slab is required. As reported in background of the work section, this can be obtained from at-point single pressure measurements by evaluation of the autocorrelation function in time and use of the Taylor hypothesis with proper values of the mean celerity. Then,

pressure distribution at the lower slab surface is computed using Eq. (3.8) that takes into account the 3D flow field and the effects of the foundation layer.

In Fig. 21, values of Ω in 3D case are reported as a function of the relative thickness Z', for different values of the soil hydraulic parameter and slab shape and it is compared with the 2D case (Fiorotto and Caroni, 2014). For reference, also the Ω values produced by considering the thin film layer condition in laboratory (where the celerity a tends to infinity and one obtains (RL_x/a; $k' \rightarrow 0$)), are shown. From the figure with reference to the 3D case, one can note that at a constant ratio of L_x/L_y, the values of the Ω coefficient can be larger than the one computed in laboratory conditions for (RL_x/a; $k' \rightarrow 0$). In 3D case, when increasing Z', the value of Ω decreases. Results in this figure shows that with increasing ratio of L_x/L_y, maintaining constant Z' and RL_x/a, the value of Ω decreases. Comparison of the results in 3D case with the 2D one shows that at a constant value of thickness Z' and dimensionless parameter RL_x/a, the values of the Ω are smaller in 3D cases than the 2D ones. It can be concluded that by considering the slab shape in 3D context, a non-negligible reduction in the value of Ω coefficient can be pointed out; this results in a realistic and more precise evaluation of slab thickness. Furthermore, the laboratory results can not assure the safety design and need a correction in order to taken into account the foundation response especially for smaller value of Z'.

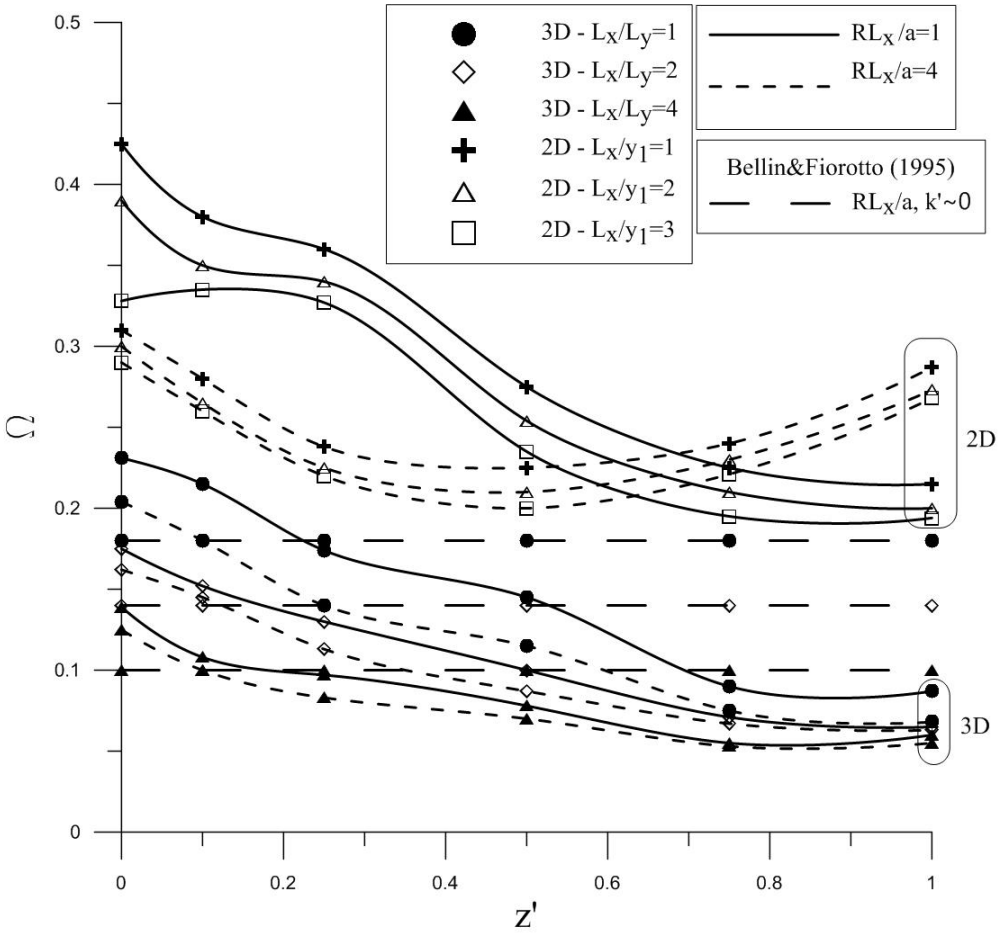

Fig. 21: Evaluation of the Ω coefficient using 3D unsteady seepage model varying slab shape L_x/L_y, foundation soil characteristics Z' and RL_x/a for unsealed joints.

In the case of sealed joints, values of Ω* in Eq. (2.1) are evaluated by use of Eq. (2.3). It is worth noting that Eq. (2.3) corresponds to the first term of Eq. (2.4) only, being related to the pressure fluctuations over the slab, since under the slab the pressure is constant related to the downstream water depth y_2. In Fig. 22, the values of Ω* and Ω in 3D condition, for different slab dimensions are compared. From the figure one can note that:

1. At a constant slab dimension, the values of Ω* are much higher than the value of Ω, in the range of slab size compatible with practical application.
2. The value of Ω* decreases when the value of L_y/y_1 increases at a constant L_x/y_1; and
3. The value of Ω increases when the value of L_y/y_1 increases at a constant L_x/y_1.

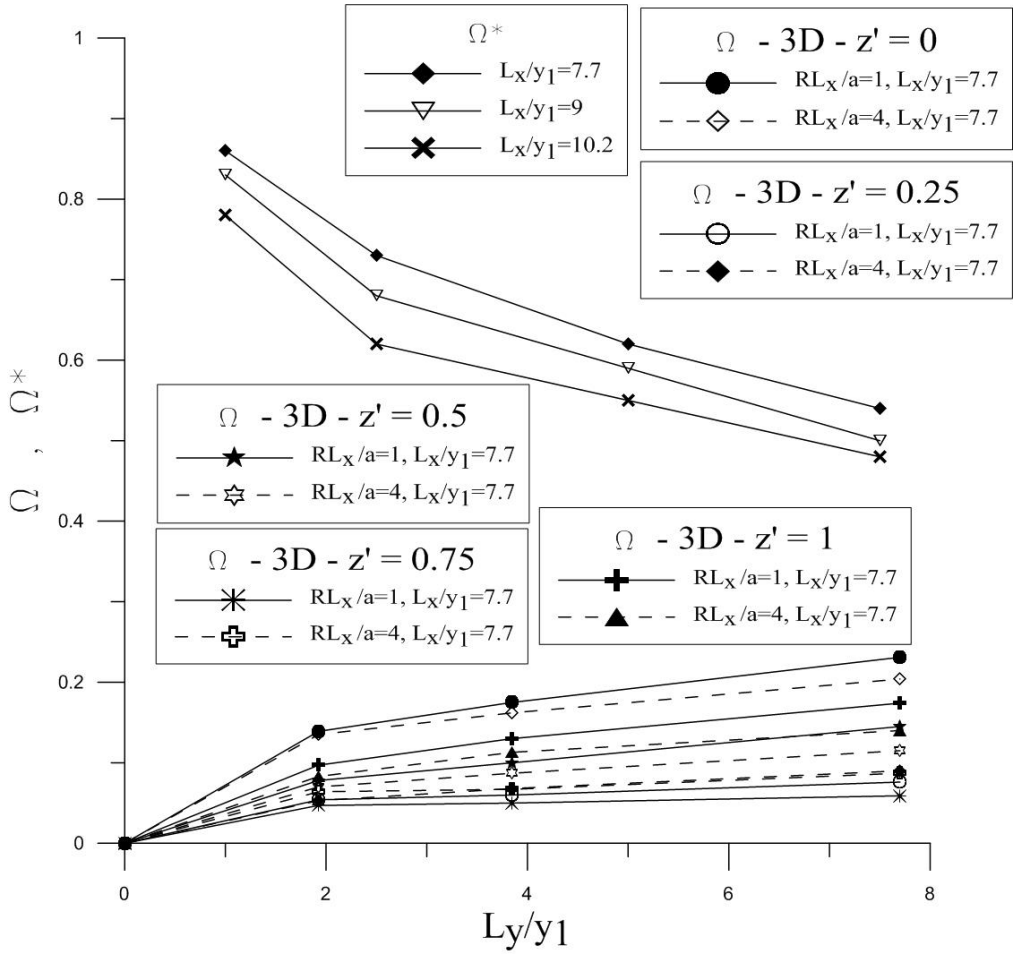

Fig. 22: Comparison of Ω and Ω* for unsealed and sealed joints conditions respectively.

In Fig. 22 the differences in the physical process that is related to the slab stability analysis in the two cases is pointed out. In the case of open joints, the total uplift force is given by the difference between the instantaneous pressure field on the slab and the underpressure, caused by the propagation of the pressure under the slab through the joints. Decreasing the ratio of L_y/y_1, the pressure field on and under the slab become more correlated so that a decrement in the total uplift force is expected (Bellin and Fiorotto, 1995). In the case of sealed joints, the pressure under the slab is constant. The decrease in the uplift force is related to statistically independent of uncorrelated spots of negative and positive fluctuating pressures with area of the order of pressure Taylor macroscale size. So that, a decrease of Ω* is expected, increasing the slab area; as a consequence Ω* tends to zero when the slab area tends to infinity.

3.6 Design example

With reference to a physical model, the design of a stilling basin with sealed and unsealed joints is presented in the following. The depth and velocity of the incident flow are assumed equal to 1.3 cm and 3.7 m/s, respectively. The resulting Froude number is 10.4. The stilling basin is paved with 10 cm long and 5 cm width concrete slabs, therefore, $L_x/y_1 = 7.7$, $L_y/y_1 = 3.8$ and $L_x/L_y = 2$. The maximum c_p^+ and c_p^- values are assumed equal to 0.5 (Fiorotto and Rinaldo 1992b). By measuring at-point pressure at the slab center, the pressure autocorrelation can be computed. Using Eq (2.17). and Fig. 11, values of celerity in all directions are obtained, so that Eq. (2.19) furnishes the whole spatial correlation function in the hydraulic jump region.
In the case of slabs with sealed joints, from Eq. (2.3) one can obtain $\Omega^* = 0.7$ (Fig. 22). The equivalent thickness of the lining is given by Eq. (2.2); assuming the ratio $\chi(\gamma_c\text{-}\gamma) = 0.66$, $y_2 = 18.5$ cm and $y_m = 7.6$ cm, it results $s \sim 23.3$ cm. It should be noted that, passing from the physical model to the prototype scale, one should consider the effect of cavitation also, that provides a limit in the maximum negative fluctuation pressure with a reduction of the slab thickness as obtained from the physical model.

In the case of slabs with unsealed joints, according to the physical model (where $RL_y/a \approx k' \to 0$), one obtains $\Omega = 0.14$ and a slab thickness $s \sim 6.4$ cm (Eq. 2.2). In the prototype scale of 1:50, the slab thickness of $s \sim 3.2$ m can be evaluated. If the slab is posed on a fissured rock layer with a significant depth, so that $Z' > 1$ and one obtains $RL_y/a = 1$ (see Table 1 in Fiorotto and Caroni, 2014). From Fig. 21 one can obtain $\Omega = 0.07$ and a slab thickness of $s \sim 1.6$ m. This is the case of Mignano Dam, Italy; the executed project is reported in Belicchi et al. (2008), while in Caroni et. al (2002) the design criteria is described.

The present example highlights the important effect of the foundation layer in the design of slab thickness, in comparison with results from laboratory experiments, where seepage cannot be properly modeled. At the same time, the convenience in adopting unsealed joint slabs is evidenced.

3.7 Conclusions

The following conclusions can be drawn from the theoretical and numerical analysis of pressure under the slab using unsteady seepage model:

- A 3D unsteady seepage model can define the pressure propagation under the slabs considering a finite thickness foundation layer.
- The computation of pressure distribution under the slab using 3D unsteady seepage model gives a more accurate result, in the evaluation of Ω coefficient, than the 2D unsteady seepage model, when the effect of transversal direction is not considered.
- When accounting for the foundation layer thickness, the under pressure force can increase with respect to the case of thin film layer.
- By increasing the ratio of L_x/L_y and maintaining constant Z' and RL_x/a, the value of Ω decreases.
- The reduction factor for sealed joint slabs, Ω*, does decrease when the slab size increases; by converse, for unsealed joint slabs, Ω does increase when the slab size increases.

This chapter is accepted for publication in journal of Hydraulic Engineering (ASCE).

Barjastehmaleki, S., Fiorotto, V., and Caroni, E. (Accepted-Corrections ongoing). "Sealed and unsealed joints in stilling basins lining design." *J. Hydraul. Eng.*

4

Anchored Slab

4.1 Introduction

The design criterion based on Eq. (2.2) is valid when slab stability is ensured only by its weight. However, if a fraction of the uplift force is sustained by anchors, the dynamic behavior of the system (slabs plus anchors) has to be considered. In this chapter, the dynamic behavior of anchored slabs is investigated.

4.2 Theoretical analysis

To study the dynamic behavior of anchored slab, the concrete slab inertia and the steel bar elastic properties must be introduced in a dynamic analysis based on the Newton law as applied to unit slab surfaces, that is:

$$(\rho_s s + m_a)z''(t) = -\frac{E_a A_a}{L_a} z(t) + C_e z'(t) + F(t) - F_s \qquad (4.1)$$

where ρ_s = concrete density, s = slab thickness, m_a = added mass, $z(t)$ = slab displacement, E_a = steel elastic modulus, L_a = effective anchor length, A_a = steel area per slab surface unit, C_e = equivalent damping of the system, $F(t)$ = force on the slab and F_s = concrete slab stabilizing force. The validity of Eq. (4.1) is depended on the elastic behavior of the system, and is valid only for positive displacements, $z(t) > 0$, Otherwise due to the presence of the foundation layer, it is $z(t) \approx 0$. The concrete slab stability force F_s for the case of unsealed joint is:

$$F_s = (\gamma_s - \gamma)s \tag{4.2}$$

whereas, in the case of sealed joints, it is:

$$F_s = (y_2 - y_m)(\gamma - \gamma_s)s \tag{4.3}$$

In the case of a slab with unsealed joints, most of the pressure on the slab is absorbed by the weight of the slab F_s so that, pressure peaks of $F(t)$ are only equilibrated by anchors (see Fig. 1 in Fiorotto and Salandin, 2000). The persistence time of these pressure peaks in the prototype are less than 1 sec (Fiorotto and Salandin, 2000), and in safety condition this peak can be outline as a square wave; as result the area of steel computed by the equivalent thickness criterion (Fiorotto and Rinaldo, 1992a) should be doubled. It is different in the case of sealed joint where the mean pressure force for unit of surface is not equilibrated by the slabs weight. So that, the anchors are stressed for long time as show in Fig. 23.

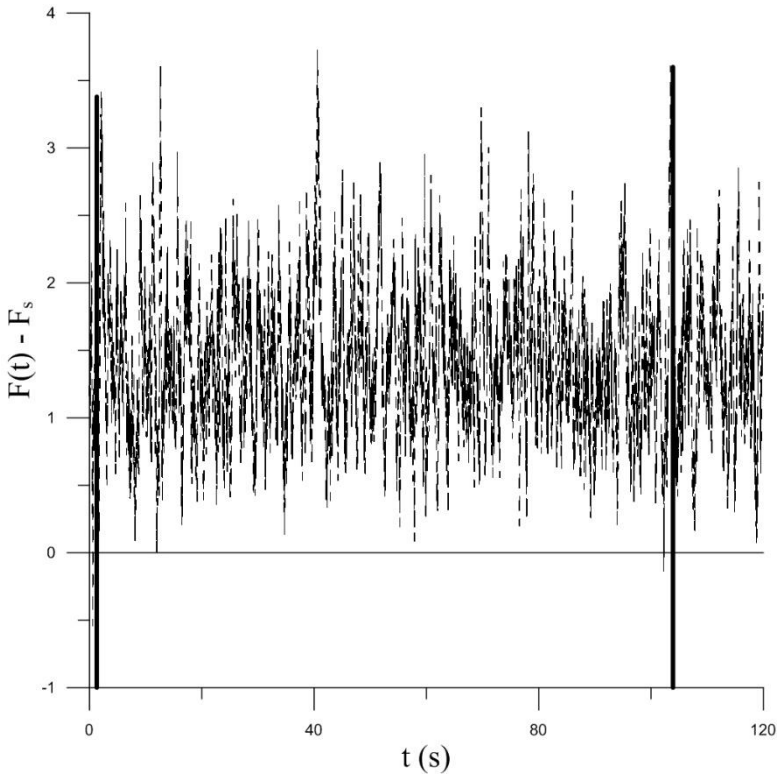

Fig. 23: Anchor force dimensionless with the submerged slab weight on the time (sec).

From Fig. 23 one can note that, in prototype condition, the anchors are stressed for time of the order of 100 sec or more. For this reason the persistence time concept as used by Fiorotto and Salandin (2000) is not suitable in this case. On the contrary, a vibrating analysis concept must be adopted, windowing the force time series where the slab displacements is larger than zero (Bendat and Piersol, 1971). Via spectral analysis, Eq. (4.1) become:

$$-(\rho_s s + m_a)k^2 z_k + \frac{E_a A_a}{L_a} z_k - c_e ikz_k = F_k \tag{4.4}$$

where z_k = the spectral components of slab displacement and F_k = the spectral components of the force acting on the slab. In static conditions, Eq. (4.4) becomes:

$$\left|\frac{z_k}{F_k}\right|^s = \frac{L_a}{E_a A_a} \tag{4.5}$$

while, in dynamic conditions, Eq. (4.4) yields:

$$\left|\frac{z_k}{F_k}\right|^d = \frac{1}{-(\rho_s s+m_a)k^2+\frac{E_a A_a}{L_a}-c_e ik} \tag{4.6}$$

By dividing Eq. (4.6) by Eq. (4.5), one obtains the amplificatory factor as a function of the wave number:

:

$$\frac{\left|\frac{z_k}{F_k}\right|^d}{\left|\frac{z_k}{F_k}\right|^s} = \frac{\frac{E_a A_a}{L_a}}{-(\rho_s s+m_a)k^2+\frac{E_a A_a}{L_a}-c_e ik} \tag{4.7}$$

4.3 Results and discussion

Fig. 24 shows the behavior of $\left|\frac{z_k}{F_k}\right|^d / \left|\frac{z_k}{F_k}\right|^s$ as a function of f/f_r, where f = frequency and $f_r = \sqrt{E_a A_a / \left[L_a(\rho_s s + m_a)\right]}$ resonance frequency. Two

different lines in Fig. 24 (termed "with" and "without C_e") outline the influence of the equivalent damping effect.

Fig. 26 shows the variations in $\left|\frac{z_k}{F_k}\right|^d / \left|\frac{z_k}{F_k}\right|^s$ when changing f/f_r, where f = frequency and the resonance frequency $f_r = \sqrt{E_a A_a / -(\rho_s s + m_a)}$. Two different lines (termed "with" and "without C_e") outline the influence of neglecting the equivalent damping effect.

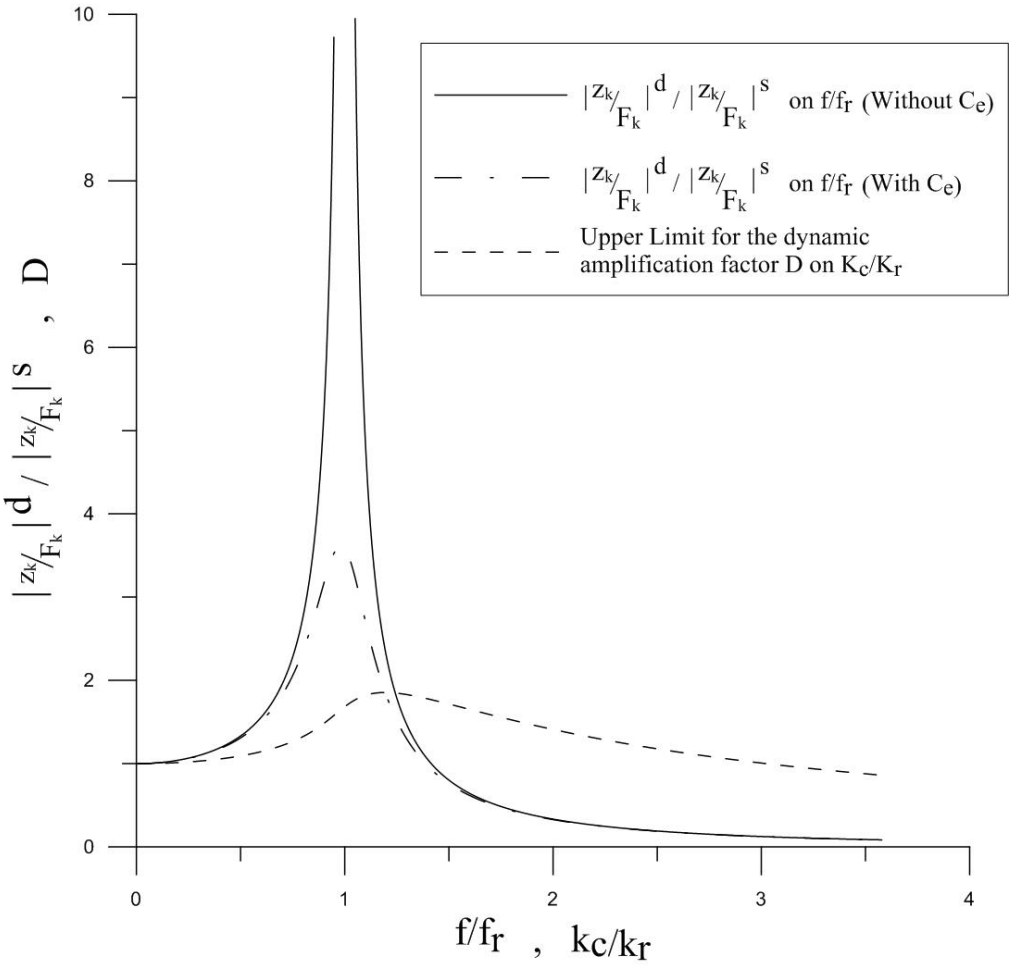

Fig. 24: Variation of $\left|\frac{z_k}{F_k}\right|^d / \left|\frac{z_k}{F_k}\right|^s$ with f/f_r and D with k_c/k_r

According to Mahzari and Schleiss (2010), using non-linear dynamic analysis, equivalent damping of the system can be obtained as ξ_d = 10.6%, corresponding to O(10π rad/s) average frequency. In Fig. 24 one can observes the range of resonance dimensionless with system resonance frequency. This can be useful

in the anchor design, since the resonance should be outside the energetic part of the force spectrum. In Fig. 24 assuming $F_k = 1$, the upper boundary of the force dynamic amplificatory factor $D = \sum_{k_c} \left|\frac{z_k}{F_k}\right|^d / \left|\frac{z_k}{F_k}\right|^s$ on the bandwidth wave number k_c dimensionless with the resonance wave number k_r is reported. The maximum value of $D = \sigma_s / \sigma_d$ is closed to 2, where σ_s is tension in static condition and σ_d is tension in dynamic condition .

In this context, an experimental analysis was carried out in order to define the force dynamic amplification factor. Simultaneous acquisition of pressure, with a sampling frequency of 500 Hz, was done in 9 points along the center line of the flume with reference to the experimental setup of Barjastehmaleki et. al., (2016). The distance between two successive taps was 1 cm. Considering a Froude model scale of 1/50, a prototype slab length is equal to 4.5 m. A maximum steel tension in static conditions equal to 300 N/mm^2 was considered. The steel area was supposed constant equal to 3.14 cm^2/m^2; the concrete slab thickness were assumed equal to 2, 3 and 4 m and the anchor effective length equal to 10 and 5 m. Using experimental data for $F(t)$, by integration of Eq. (4.1), via finite difference with time step equal to 1/500 sec, the amplificatory factor D was computed for every case (Table 2). The resonance frequency is also reported in the table.

Table 2. The values of amplification factor D

Test	Fr	s	A_a	L_a	σ_s (N/mm^2)	σ_d (N/mm^2)	$D = \sigma_s / \sigma_d$	f_r
1	10	2	3.14	10	300	370	1.23	6
2	10	2	3.14	5	300	410	1.37	8
3	10	3	3.14	10	300	350	1.17	5
4	10	3	3.14	5	300	460	1.53	7
5	10	4	3.14	10	300	350	1.17	4
6	10	4	3.14	5	300	480	1.6	6

From the table one can note that, in the limits of the present work with one hour acquisition time, the dynamic amplification factor of the pressure is about 1.6 close to 1.8 its maximum theoretical value. With the same slab thickness, an increase on the amplificatory factor is detected when the resonance frequency

increases. This means that in the range of variation of the resonance frequency the force spectral components are still quite important (Fig. 24). By adding some safety coefficient, a maximum value of the dynamic amplification factor equal to 2, as defined by Mahzari and Schliess (2010) and Fiorotto and Salandin (2000), can be reasonably assumed in both cases of sealed and unsealed joints.

4.3 Design example

Generally in the case of unsealed joints the anchors could be not necessary if the slabs are properly design because the thickness of the slabs is of the order of few meters. Otherwise, in the case of sealed joint slabs require anchors; with reference to the design example in chapter 3 the concrete thickness should be equal to 12 m in the prototype scale 1:50.

Using concrete slabs with thickness equal to 3 m the equivalent concrete slab thickness equal to 8.5 m multiply for the dynamic amplificatory factor $D \approx 1.2$ for anchor with effective 10 m in length (table 2) must be assigned to the steel. This amplificatory factor was computed with steel bars having area of 3.14 cm^2 for meter square. In this case a maximum stress equal to 480 N/mm^2 is obtained; this is compatible with GEWl® Plus S670/800 Threadbar anchors assuming a proper safety factor.

4.4 Conclusions

In the case of sealed joints the anchors design is analyzed theoretically with the support of experimental data. The theoretical difference in the analysis between the case of unsealed and sealed joint is highlighted. In the case of sealed joint the anchors must be properly design with reference to the resonance frequency of the system and to the spectra of the fluctuating pressure in order to not overstress the steel bars.

This chapter is accepted for publication in Journal of Hydraulic Engineering (ASCE).

Barjastehmaleki, S., Fiorotto, V., and Caroni, E. (Accepted-Corrections ongoing). “Sealed and unsealed joints in stilling basins lining design.” *J. Hydraul. Eng*.

5

Stability analysis of plunge pool linings

5.1 Introduction

The stability of concrete slabs or rock blocks at plunge pool bottom depends on the instantaneous pressure field (e.g. Bollaert and Schleiss, 2003; Melo et al., 2006, Pinheiro and Melo, 2008, Federspiel, 2011). This pressure propagates under lining elements in the case of open or failed joints or cracks developing across the slab thickness, generating an uplift force that can lead to dislodging or structural failure of the lining (Fig. 29). This instability can be investigated separately with reference to the mean dynamic pressure and to the fluctuating components. According to the conclusions by Melo et al. (2006), the mean value of the hydrodynamic forces determines the stability of plunge pool slabs, being small the value of the force fluctuations. For these reasons, an accurate description of the jet behavior must be sought, with reference to the distribution of the mean pressure at the bottom.

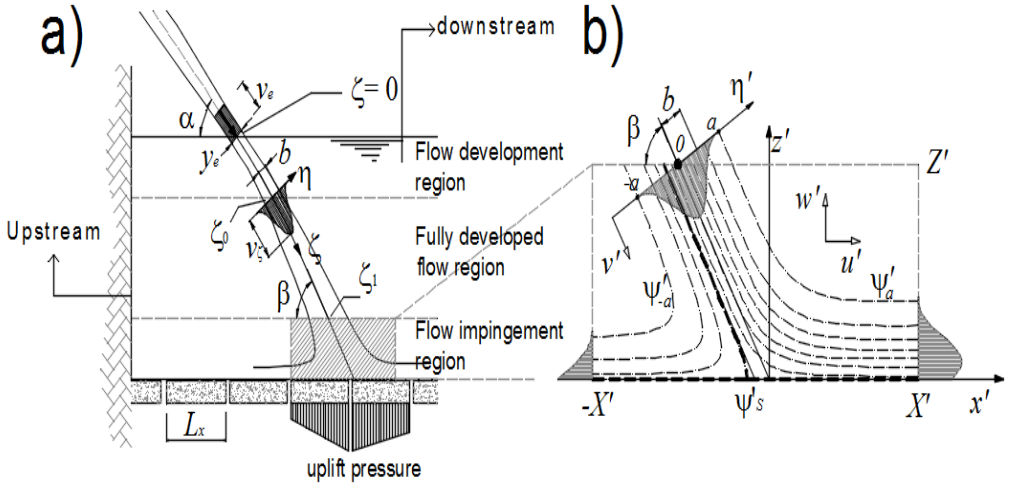

Fig. 25: Sketch of a plunge pool and notation: a) jet evolution and b) jet impingement region

The aim of the chapter is to extend the work by Melo et al. (2006), referred to a vertical two dimensional jet in an unconfined two dimensional pool, to the case of real plunge pools being characterized by inclined jets entering a pool that is confined upstream by the presence of the drop structure, so that the discharge can flow only in the downstream direction. Successively an analysis of the effect of the pressure fluctuating components in the stability of concrete slab with open joints is analyzed with the purpose to highlight their relative role, as evidenced experimentally in the Esaro Dam plunge pool physical model (Marson et al., 2007).

The first task is accomplished by dividing the flow field into a region where the submerged jet diffuses and, subsequently, a region of impingement at the plunge pool bottom. Separate solutions for these two flow regions can be found, that, once coupled, can provide an overall solution. The advantage of this approach is that each region may be represented by models closely related to the physics of the problem, in order to derive the relevant quantities needed for engineering purposes in plunge pool design.

After impingement, the flow behaves like a submerged wall jet, where the main flow diffuses rapidly along the pool floor and a large recirculating flow region is formed (Liu et. al., 1998). This region is often referred to as the wall-jet zone (e.g. Beltaos and Rajaratnam, 1973). Here the mean dynamic pressure becomes

more and more negligible (e.g. Beltaos and Rajaratnam, 1973, Tu and Wood, 1996) so that it will not be considered in the following.

The study is mostly addressed to Froude scale models in fully developed jets plunging in quite deep pools, where, due to scale effects, aeration and pressure propagation under the lining are not properly taken into account; in order to apply model results to prototype conditions also in deep pools in the case of high head, large scale applications, some considerations on these effects are also reported (Mahzari et al. 2002; Mazhari and Schleiss. 2010).

5.2 Preliminary analysis: jet evolution in an unbounded domain

A schematic plunge pool is shown in Fig. 29a: a free falling two dimensional nappe, plunging through the atmosphere, enters a plunge pool or water cushion. The diffusion of the free jet in the pool dissipates the inflowing energy with attenuation of pressures and velocities at impingement with the pool floor.

5.2.1 Free fully developed jets

The free jet analysis in fully developed conditions is here performed following Kotsovinos and Angelidis (1991) that furnish a comprehensive treatment of the phenomenon, consistent with experimental evidences.

Once a compact jet of fairly constant velocity enters the water cushion, the sharp discontinuity between the jet velocity and the surrounding fluid that produces mass entrainment, decelerates the jet. A constant-velocity core within the jet decreases in lateral extent, while both the flow rate and the overall width of the jet increase in magnitude. When the constant velocity core vanishes for $\zeta_0 = 6$ y_e (Cola, 1965; Tu and Wood, 1996), the jet becomes fully developed, showing self-similarity in the mean velocity transverse distribution, of Gaussian type. This distribution is parameterized via parameter b, the distance from the jet axis, where velocity is at maximum, to the point where velocity halves its maximum value. The jet diffusion causes a reduction in momentum due to two factors: i) the induced pressure field; ii) the induced velocity field in the plunge pool.

The jet at pool entrance is defined by its thickness, y_e, and velocity, v_e, providing the specific discharge $q_e = y_e\, v_e$ and the inflow momentum M_e. The momentum along the jet axis ζ, having origin at the jet pool entrance (Fig. 29a), in the fully developed region at a distance $\zeta > \zeta_0 = 6\ y_e$ (Fig. 29a) is (Kotsovinos and Angelidis, 1991):

$$M(\zeta) = 0.974\, M_e (\zeta_0/\zeta)^{0.071} \tag{5.1}$$

From a comprehensive analysis of experimental data by several authors, Kotsovinos (1976, 1978b) derives the following formula for the parameter $b(\zeta)$:

$$b(\zeta)/y_e = 0.228 + 0.0913\,\zeta/y_e + 5.101\cdot 10^{-5}(\zeta/y_e)^2 + 3.31\cdot 10^{-7}(\zeta/y_e)^3 \tag{5.2}$$

Due to self-similarity in the velocity distribution, Eq. (5.1) and (5.2) provide a complete description of the jet evolution in the plunge pool. In particular, the Gaussian distribution of velocity, as a function of a dimensionless abscissa $\eta' = \eta / b$ orthogonal to the jet axis, can be approximated in the form (e.g. Rubel, 1980)

$$v' = v(\eta', \zeta)/v_\zeta = \left[1 - \tanh^2(C\eta')\right] \tag{5.3}$$

where v_ζ is the maximum centerline velocity at jet length ζ and $C = \operatorname{arc\,tanh}(1/\sqrt{2}) = 0.881$. Here, the momentum is $M(\zeta) = 4\rho\, b\, v_\zeta^2 / (3C)$, with ρ = water specific mass, so that the maximum velocity is given by

$$v_\zeta = \sqrt{\frac{3C\, M(\zeta)}{4\rho\, b(\zeta)}} \tag{5.4}$$

By integration of Eq. (5.3) over η', the jet specific discharge is found:

$$q = 2 b v_\zeta / C \tag{5.5}$$

Equations (5.1) to (5.5) define a direct solution of the jet characteristics in the fully developed flow region, representing the inflow boundary condition for the impingement region. One can note that Eq. (5.5) is obtained by integrating Eq. (5.3) in η' from minus infinity to plus infinity. As observed by Kotsovinos (1978a) this is an acceptable approximation with the following limits: i) from a physical point of view, an interface between the jet and the surrounding flow field appears in laboratory evidences; ii) from a theoretical point of view the jet volume flux is not correctly represented. For these reasons, finite limits in the integration in η' must be imposed. With limits in the integration of $\eta' = a$

equal to ±3 (Fig. 29b) one obtains an error of 1% in discharge, as evaluated according to Eq. (5.5).

5.2.2 Jet impingement in an unbounded domain

Rubel (1980) studied the impingement of an oblique jet inclined at an angle β (Fig. 29b) using an inviscid rotational model, by numerical integration of dimensionless Poisson type equation, in terms of stream function ψ' and vorticity function ω'.

$$\frac{\partial^2 \psi'}{\partial z'^2} + \frac{\partial^2 \psi'}{\partial x'^2} = -\omega' \tag{5.6}$$

The dimensionless variables in Eq. (5.6) are scaled with the relevant quantities at the inlet of the impingement region, at the depth ζ_1 (Fig. 29a), namely: velocities, with the maximum jet velocity v_1 (Eq. 5.4), distances with b_1 (Eq. 5.2) and pressures with the total pressure at the jet centerline, equal to $p_1 = \rho v_1^2 / 2$.

The dimensionless mean pressure is determined from an auxiliary Bernoulli equation

$$p' + u'^2 + w'^2 = f(\psi') \tag{5.7}$$

that implies that the total pressure is conserved along a streamline. Eqs. (5.6) and (5.7) complete the impingement problem formulation, allowing to compute the pressure and velocity fields at the plunge pool bottom, when solved with the proper boundary conditions in a domain Z'=5 and X'=10 (Fig. 29b). Larger integration domains were tested, as shown in Fig. 30, obtaining the same results at impingement.

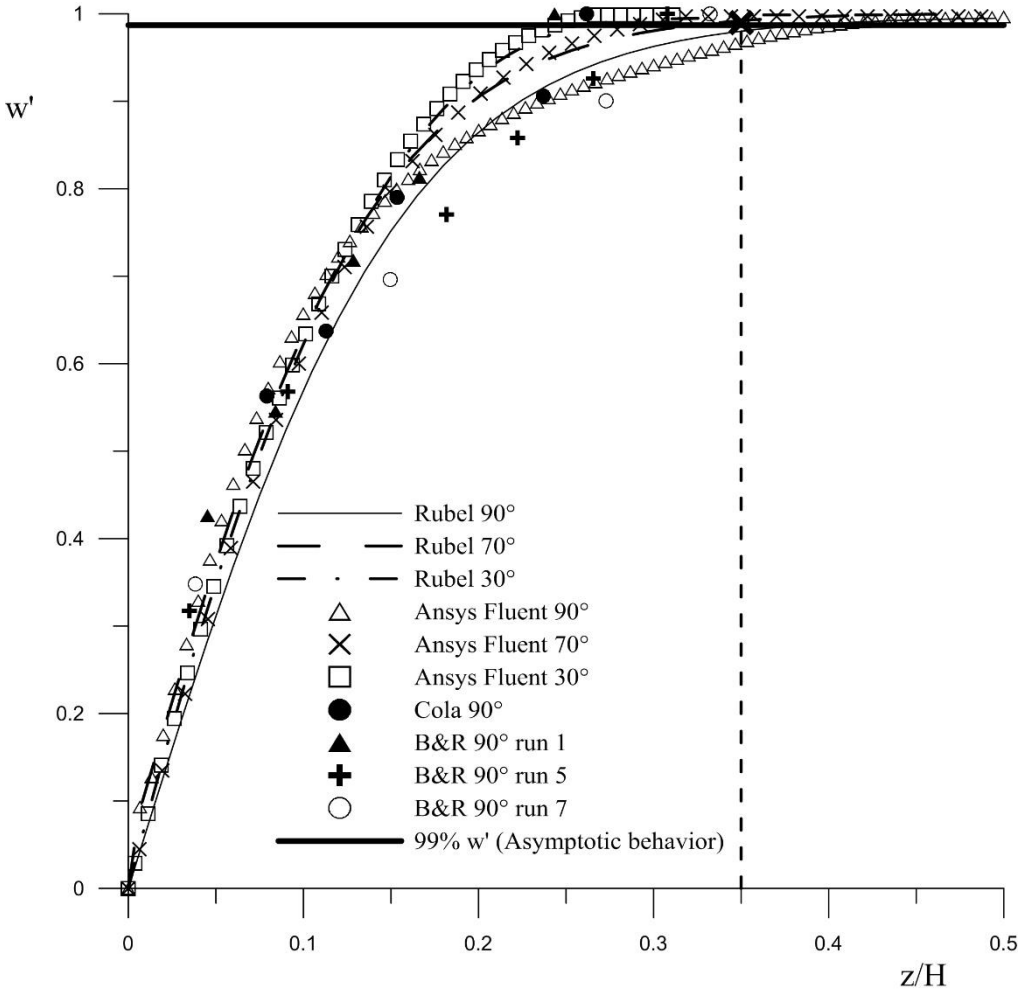

Fig. 26: Dimensionless vertical velocity component along an impinging jet centerline as a function of the distance *z* from the bottom and of the impinging angle in a pool of depth *H*; symbols refer to experimental data by Beltaos and Rajaratnam (1973) and Cola (1965) and to numerical results

The boundary conditions to be imposed are (see Fig. 29b):

i) at the floor, $\psi'(x',0) = \psi'_s$, where ψ'_s is the value of the streamline function at stagnation; ii) at the two side boundaries, parallel outflow, $\partial\psi'/\partial x' = 0$; iii) at the jet inflow, the velocity v' according to Eq. (5.3) that, in terms of dimensionless streamline functions, reads

$$\psi'(\eta') = 1/C \tanh(C\eta') \tag{5.8}$$

The vorticity at the inflow boundary is conserved along each streamline; then, from Eq. (5.8), the vorticity function, ω' in Eq. (5.6), becomes:

$$\omega' = -2C^2\psi'\left(1 - C^2\psi'^2\right) \tag{5.9}$$

The bottom boundary condition, $\psi'(x',0) = \psi'_s$, needs the definition of the streamline function value at stagnation. This can be performed via momentum balance in the x' direction, as applied to the control volume of Fig. 29b:

$$2\cos\beta\int_0^{\psi'_a} v'd\psi' = \int_{\psi'_s}^{\psi'_a} u'\,d\psi' + \int_{\psi'_s}^{\psi'_{-a}} u'd\psi' \tag{5.10}$$

where v' and u', as expressed in terms of streamline functions, are $v' = u' = 1 - C^2\psi'^2$ (Rubel, 1980). For $\eta' = a \geq 3$ (Fig. 29b) practically all the inflow discharge is enclosed between the two streamline $\psi'_{\pm a}$, so that one obtains $\psi'_{\pm a} \cong \pm 1/C$. Thus, from Eq. (5.10), it results

$$\cos\beta = 3/2\, C\psi'_s\left(1 - C^2\psi'^2_s/3\right) \tag{5.11}$$

that allows the computation of the bottom boundary condition $\psi'(x',0) = \psi'_s$ as a function of β.

Using Eq. (5.9) in Eq. (5.6), the latter can be expressed in terms of streamline functions only, so that it can be solved according to the very efficient numerical procedure suggested by Rubel (1980) in a rectangular computational domain (obtained via a proper coordinate transformation), with evident advantages in the numerical procedure and accuracy in the solution.

The bottom pressure field is reported in Fig. 31 at varying impingement angle β in the range from 30° to 90°, at 10° intervals.

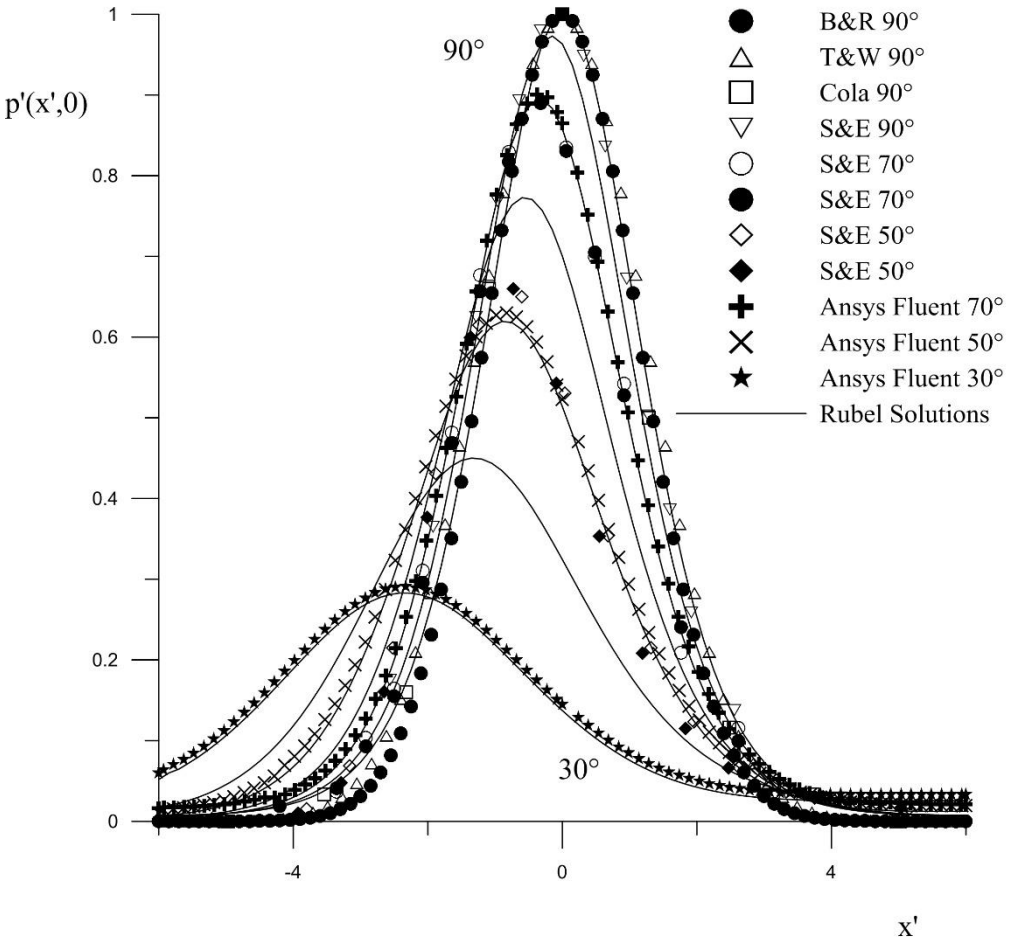

Fig. 27: Rubel (1980) bottom pressure solution varying impingement angles. Symbols are referred to: experimental results by B&R Beltaos and Rajaratnam (1973), T&W Tu and Wood (1996), Cola (1965), S&E Schauer and Eustis (1963); numerical results: Ansys Fluent

In Fig. 31, the experimental pressure distribution obtained by Beltaos and Rajaratnam (1973), Tu and Wood (1996), Schauer and Eustis (1963) and Cola (1965) are reported. Experimental results are in mutual agreement even if measurements by Beltaos and Rajaratnam (1973) show a slight difference with the other ones. While Beltaos and Rajaratnam (1973) evidence the Gaussian distribution of their experimental data, Tu and Wood (1996) observed that bottom pressures do not follow exactly a Gaussian distribution and proposed an additive correction function that becomes effective at the distribution tails, in order to improve the interpolation of their experimental data. The Rubel solution shows a pressure distribution slightly different respect to the Gaussian that,

particularly at low pressure values, fits the experimental data by Tu and Wood (1996), Schauer and Eustis (1963) and Cola (1965).

For oblique jets, in Fig. 31, the experimental pressures as measured by Schauer and Eustis (1963) for impingement angles of 70° and 50° are reported. While the theoretical solution is in good agreement with measurements at 70°, some differences can be appreciated at 50°, yet in the order of 5%. To complete this task, numerical simulations with Ansys Fluent were conducted using a turbulence SST model, showing a good agreement with the solution obtained via the inviscid rotational model for impingement angles of 70°, 50° and 30°.

With reference to Fig. 29a, the free jet region is confined between the water surface and the top of the impingement region; hence, the evaluation of the length ζ_1 requires the definition of the impingement region height. In this context, further experimental results by Beltaos and Rajaratnam (1973) and Cola (1965) are useful to define the extension of the impingement region by the analysis of the velocity distribution along the stagnation streamline when approaching the bottom. The limit between the free jet region and the impinging region is posed by Beltaos and Rajaratnam (1973) at a height of about 0.3 of the total pool depth H from the bottom for a vertical jet. With reference to Rubel (1980) the impingement region extension Z' is assumed equal to 5 b_1. Assuming $b_1 \approx 0.1\ \zeta_1$ (Kotsovinos, 1978b) one obtain the limit between the free jet and impingement region at a distance z from the bottom equal to $H/3$.

In Fig. 30, the vertical velocity along the stagnation streamline is reported as a function of the relative height over the bottom for jet inclination of 90°, 70° and 30°. For orthogonal jets, the vertical velocity obtained from Rubel is in agreement with experimental results and numerical simulations. For oblique jets, the SST numerical simulation is in agreement with the inviscid rotational model.

From Fig. 29, one can observe that the impingement region height is independent of the jet inclination and, congruently with experimental results, it is assumed equal to 35% of the plunge pool water depth, close to the 33% ratio that is reported by Rubel (1980). This choice is validated by the results presented in the numerical analysis section.

In conclusion, the inviscid rotational approach is able to furnish the flow pattern in the impingement zone and the bottom pressure, as confirmed in the comparison with experimental evidences and numerical simulations.

5.3 Theoretical analysis jet impingement in a plunge pool

From Fig. 31, the influence of the β angle in the bottom pressure can be appreciated. When decreasing the β angle, a decrement in pressure is evident: profiles differ sensibly from the one obtained in the 90° impingement condition. In the case of an impinging free-jet in an unbounded domain, as studied by Melo et al. (2006), the angle β is theoretically equal to the inflowing jet grade α (Fig. 29a). However, this is no longer true for the plunge pool case, where the upstream outflow is null due to the presence of the fall structure (Fig. 29a) and the discharge separation in the upstream and downstream components is therefore constrained. In this case the impingement angle β must be evaluated adding the mass balance condition to the momentum equation (Eq. 5.11).

The impinging jet discharge q (Eq. 5.5) is composed by two terms: i) the inflow discharge q_e; ii) the upstream and downstream entrained discharges along the free jet boundary, q_r, that are equal due to symmetry. The symmetry in the fully developed region (Fig. 29a) was checked in Liu et al. (1998) that report direct velocity measurements via hot wire anemometer in the hydraulic model of the Xiluodu Dam plunge pool. In their experiment, the jet has an impact inclination of 65° and a 3H distance from the upstream wall at impact; the measurements show a Gaussian (symmetrical) velocity distribution at different depths in the fully developed region, so that the symmetry in the recirculating discharge q_r is assured. Generally, in large dam plunge pools (e.g. Sa Stria Dam, Ursino et al., 2003; Esaro Dam, Marson et al., 2007) the jet impingement distance from the upstream wall is larger than 3 times the plunge pool water depth; this prevents wall effects affecting the free jet velocity profile. In the next chapter, via numerical analysis, the effect of the wall distance from the impact will be investigated in order to check the limits in theory.

The inflow discharge q_e is equal to the downstream outflow discharge, while the entrained discharges constitute the recirculation fluxes $q_r = (q-q_e)/2$. From Fig. 29b, one can observe that the stagnation streamline, ψ'_s, subdivides the inflow velocity distribution in two parts: the one flowing upstream, $q_U = q_r$, and the one flowing downstream $q_D = q_e + q_r$, with a ratio to the total flow

$$\begin{aligned} q_U/q &= (\psi'_a - \psi'_s)/(\psi'_a - \psi'_{-a}) \\ q_D/q &= (\psi'_s - \psi'_{-a})/(\psi'_a - \psi'_{-a}) \end{aligned} \tag{5.12}$$

Any of the two can be used to obtain the value ψ'_s that, introduced in Eq. (5.9), furnishes:

$$\beta = \cos^{-1}\left[\frac{3}{2}\frac{q_e}{q}\left(1-\frac{1}{3}\frac{q_e^2}{q^2}\right)\right] \tag{5.13}$$

In conclusion for confined pools, the impingement angle β results independent from the impact angle α at the plunge pool surface, being related to the mass balance condition at impingement.

In Fig. 32, the ratio $\frac{q_e}{q} = \frac{q_d - q_u}{q_d + q_u}$ is shown as a function of β according to Eq. (5.13). This relationship can be fairly approximated by the linear function $\frac{q_e}{q} = 1 - 0.011\beta$. For completeness, the maximum values of pressure at the plunge pool bottom, as a function of β, are reported, playing a relevant role in lining stability. From the figure, one can observe that, for β = 90° the solution q_e = 0 is derived. In plunge pools, this condition is physically unfeasible, because the presence of the upstream wall implies the impossibility to have an outlet discharge in the upstream direction other than zero.

In fully developed conditions, the ratio q_e/q can be estimated, in first approximation, by neglecting the reduction of momentum flux and assuming $b \approx 0.1\zeta_1$. Via Eqs. (5.4) and (5.5) the relationship $q_e/q \approx \sqrt{Cy_e/(0.3\zeta_1)}$ is obtained. For pools with $\zeta_1/y_e \geq 14$ one obtains $q_e/q \leq 0.45$ and, as a consequence, $\beta \geq 50°$; in this range, corresponding to most real life situations, the validity of the inviscid rotational model is experimentally confirmed. The limiting case for a fully developed jet (Fig. 29a) is $\zeta_1 = \zeta_0 = 6\ y_e$, so that q_e/q = 0.7; this corresponds to a lower limit of 30° for the β angle. As a

consequence, the minimum impingement angle in fully developed condition in a plunge pool is about 30°.

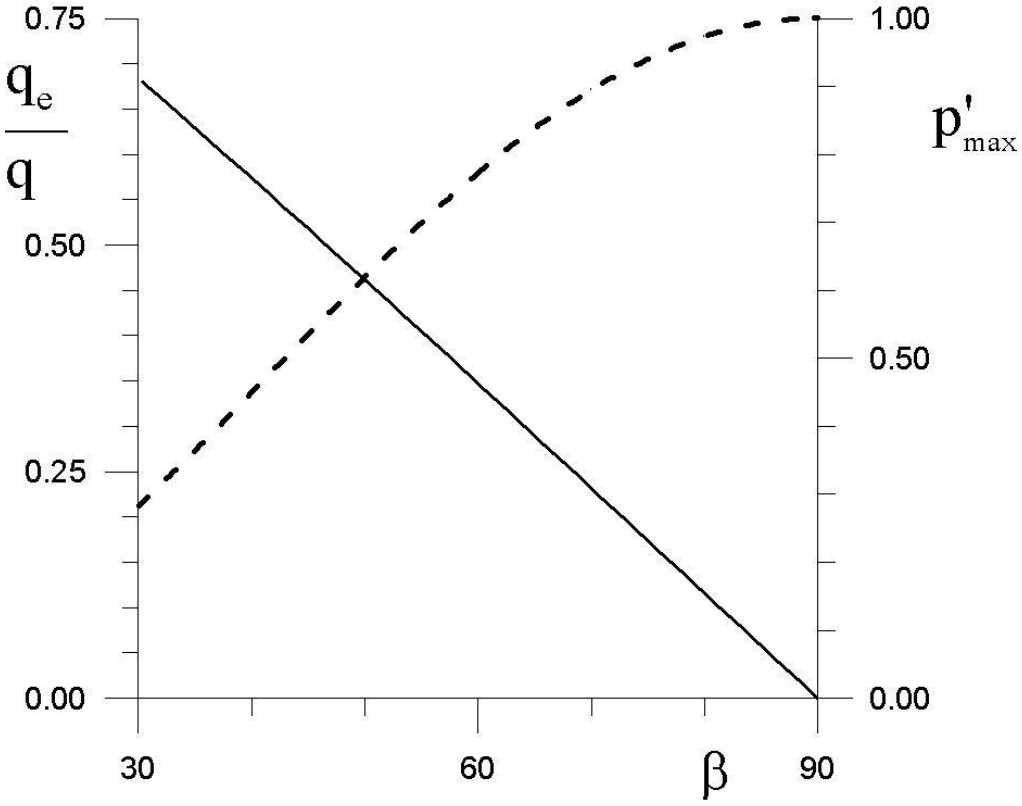

Fig. 28: Flow repartition (solid line) as a function of the impingement angle β (degrees); maximum pressure at the stagnation point (dashed line) is also indicated

5.4 Numerical analysis of jet impingement in plunge pool

In the former analyses, some results are not adequately documented by literature experimental outcomes. In particular, the following issues must be considered: i) the bottom pressure distribution for impingement angles lesser than 50°; ii) the thickness of the impingement region for non-orthogonal impact angles, which is important in the definition of the ζ_1 length along the free jet axis (Fig. 30) ; iii) the bottom pressure distribution when the distance of the upstream wall from the jet impact is lesser than 3*H*.

To these issues, a numerical model, using the ANSYS Fluent 14.0 code, was developed in order to support the theoretical analysis.

Castillo et al. (2014a) and Castillo and Carrillo (2011) tested different turbulence models in the falling jet case. In their work, the SST turbulence model was selected as the most adequate, because it takes into account the accuracy of the k-ω model in the near-wall region and the free stream independence of the k-ε model in the outer part of the boundary layer.

In the present work the SST model was used to represent the evolution of an oblique jet in a plunge pool. The mesh size was chosen according to Castillo and Carrillo (2015) and Epely et al. (2014) in 0.1 y_e. Preliminary runs at decreasing mesh size showed the obtained solutions to be mesh-independent.

In Fig. 33, the streamlines in a plunge pool, changing the jet impact angle α at the free surface, are shown. The numerical simulation was performed in a plunge pool physical model, with water depth H equal to 1.5 m, y_e = 0.04 m and velocity v_e equal to 5 m/s. The jet inclination at the pool entrance α was assumed equal to 90° and 70°.

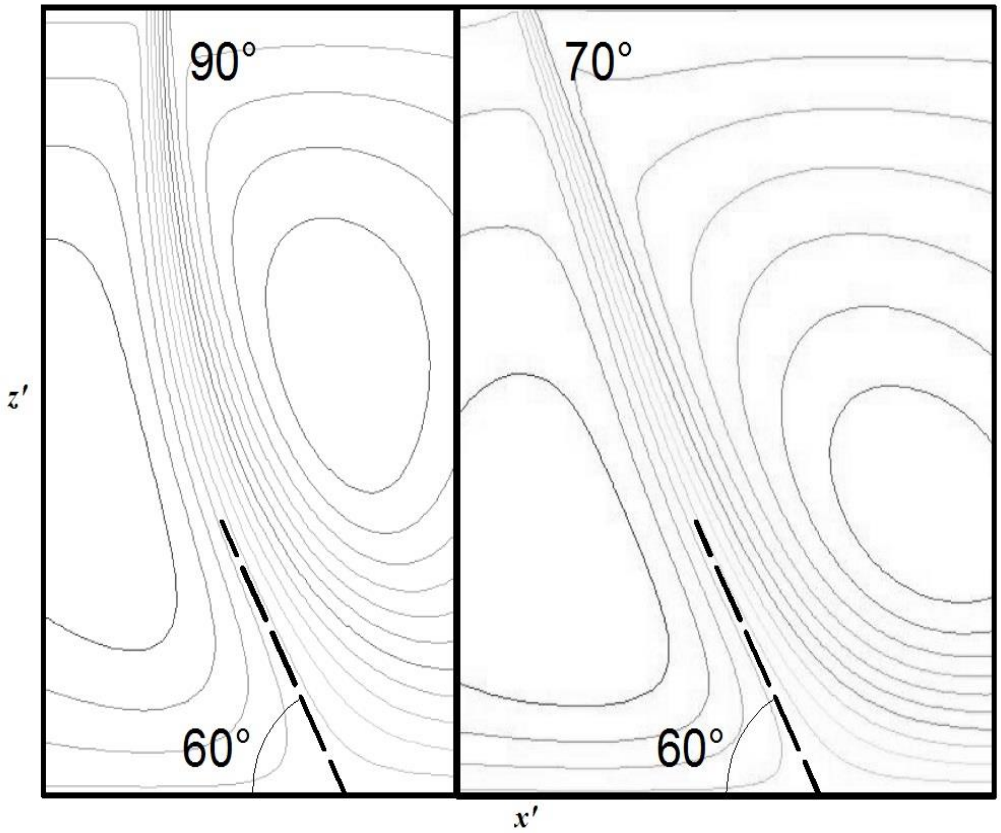

Fig. 29: Numerical simulation: streamlines at impingement for α = 90° and α = 70°

The drop structure in the upstream direction is located at a distance equal to 3*H* from the impact of the jet in the plunge pool water surface while the free flow condition was imposed in the downstream direction at a distance equal to 6 *H*, larger than the downstream vortex system extension in the plunge pool.

Streamlines allow defining the impingement angle β. For α = 90°and α = 70°, practically, a same angle β is obtained, close to 60°.

By observing (Fig. 34) that the mean dynamic pressure, as derived from the numerical model, is independent of α and fits the Rubel solution, the general theoretical framework here presented results to be adequate, at least for engineering purposes.

The streamlines in Fig. 33 allow estimating the discharge ratio q_e/q: at the upper limit of the impingement region this ratio is equal to 0.35 that, from Fig. 32, gives an estimation of the β angle close to 59°, in agreement with the ones

derived graphically from the streamline shape. This supports the issue that the impingement angle β is independent from α.

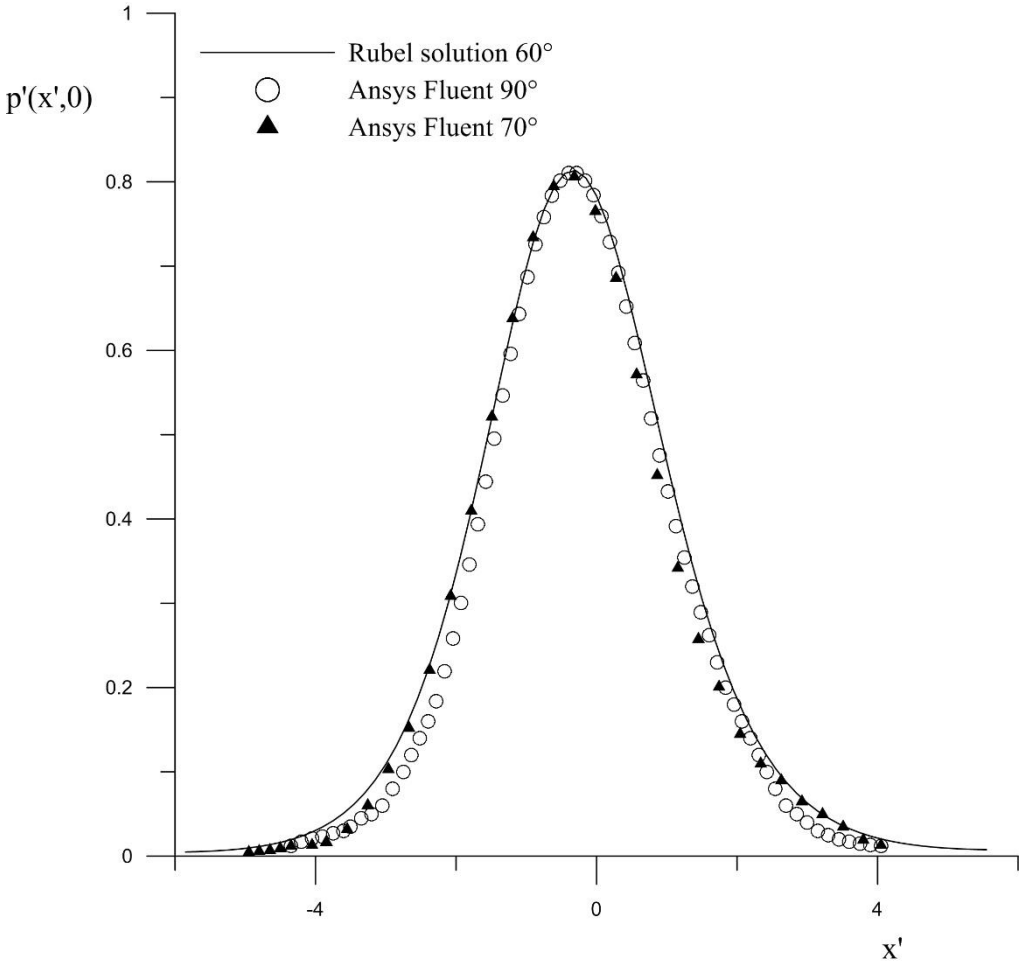

Fig. 30: Numerical simulation: pressure at the bottom for α = 90° and α = 70°

The computation, according to the theoretical framework, gives the following results. In the case of vertical jet (Fig. 33) assuming $\zeta_1 = 0.65$ H=0.975 m one obtains by Eq. (5.1) a momentum $M(\zeta_1)$ = 882 N/m and, from Eq. (5.2), b_1 = 0.10 m. Via Eqs. (5.4) and (5.5) one obtains the discharge q at ζ_1 equal to 0.54 $m^3/s/m$, larger than the inflow discharge of 0.20 $m^3/s/m$. The ratio q_e/q is equal to 0.37. According to Eq. (5.13) a β angle of 58.2° is computed in good agreement with the numerical simulations. In the case on inclined jet of 70° (Fig. 33) one obtains $\zeta_1 = 0.65$ $H/\sin(70°)$ =1.04 m; via the same procedure, a β angle of 59.0° degree is computed.

The SST model allows defining the bottom pressure behavior when decreasing the impingement angle in an unbounded domain, for which cases experimental data are not sufficiently exhaustive. In Fig. 31, for β = 70°, 50° and 30°, the numerical results are compared with the Rubel solution. One must consider that, in numerical results, the effect of bottom shear stress is included; in particular, the numerical bottom shear stress was checked with the experimental results by Tu and Wood (1996) in an unbounded orthogonal impingement condition that brought to a good agreement, giving evidence of accuracy in the reproduction of turbulent stress gradients by the SST model. From Fig. 31, one can note that the Rubel solution proves adequate to be used in a range of β > 30° compatible with the fully developed jet condition.

The numerical results reported in Fig. 33 were obtained posing the upstream wall at a distance of three times the water depth from the jet impact as it was reported in the experiments by Liu et al. (1998). When decreasing this distance, a departure from the free jet behavior is expected due to the wall effect. For the same case as α = 70° in Fig. 33, in Fig. 35, the bottom pressures are reported, as computed posing the upstream wall at a distance 3*H*, 2*H* and *H* from the jet impact at the water surface. In this figure, the agreement of the Rubel solution with the numerical evaluation at distance 3*H* is evident. In good substance, for distances larger than 3*H*, the jet behaves like an oblique jet in an unbounded domain with impingement angle β computed according to Eq. (5.13). Decreasing the distance of the upstream wall, a slight increase in the maximum pressure is detected. At the same time, the stagnation point, where the maximum pressure occurs, is slightly displaced upstream. Yet, the overall shape of the bottom pressure distribution is preserved and the Rubel solution appears still to be a fair candidate to interpret the actual pressure distribution at the bottom.

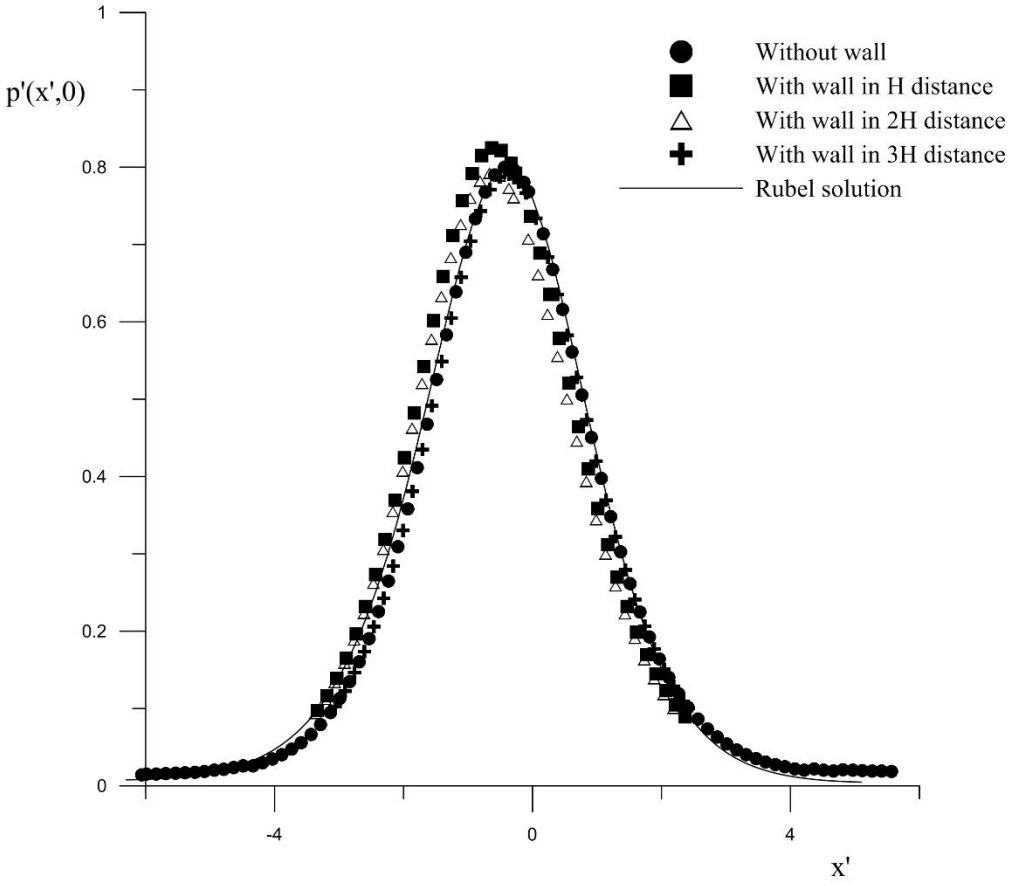

Fig. 31: Effect of upstream wall position on the bottom pressure distribution for the case α = 70° in Fig. 33

5.5 Bottom stability analysis

In the following paragraphs, the plunge pool bottom stability will be analyzed with reference to: β = 90°, a vertical free jet, useful for comparison with literature results; β = 60°, representing a typical impingement angle; β = 30°, close to the lower boundary of the impingement angle in fully developed flow conditions.

The force $F(t)$ acting on the plunge pool bottom is composed by an average force F_0 due to the mean dynamic pressure and a time varying component $F''(t)$ due to pressure fluctuations:

$$F(t) = F_0 + F''(t) \tag{5.14}$$

The mean force, F_0, can be computed from the balance of the mean pressure field over the slab and the uplift force due to the mean pressure transmitted

under the slab through the open joints, in steady state conditions. In particular, pressure under the slab is derived, in steady state seepage conditions, solving Darcy equation (Fiorotto and Caroni, 2014).

In case when a thin, homogeneous, isotropic and horizontal filtration layer between slab and bedrock can be assumed, as it is the case for laboratory conditions, (e.g. Bellin and Fiorotto, 1995, Melo et al., 2006) the Darcy equation for pressure p becomes

$$\frac{\partial^2 p}{\partial x^2} + \frac{\partial^2 p}{\partial y^2} = 0 \tag{5.15}$$

Solving numerically Eq. (5.15), e.g. via a finite difference scheme, with boundary conditions constituted by the mean dynamic pressure along the slab joints, the uplift pressure field is obtained that, by integration over the underside slab area, furnishes the uplift force F_u. Integration over the slab surface of the pressure field due to jet impingement gives the mean stabilizing dynamic force F_s, so that $F_0 = F_u - F_s$. The minimum stable slab thickness s, relative to the mean dynamic force, is given by:

$$s = F_0 / [A(\gamma_c - \gamma)] \tag{5.16}$$

where A is the slab area and γ_c, γ are the specific weights of concrete and water, respectively.

In a 2D scheme, the slab is assumed as rectangular with length L_x along the flow direction and transversal width L_y. The pressure field (Fig. 31) changes only along the flow direction L_x, while is constant transversally.

In Fig. 36 the value of the dimensionless specific force $F_0' = F_0 / \left(A \rho v_\zeta^2 / 2\right)$ is shown as a function of $L'_y = L_y/b_1$ and $L'_x = L_x/b_1$ for jets impinging at 90°, 60° and 30°. In all cases the stagnation point is located at a slab joint (Fig. 29a) and the joints are unsealed. For comparison, the 1D solution is also reported which is congruent with the one by Melo et al. (2006), where waterstop failure at both upstream and downstream joints of an isolated slab is considered.

Only for the 90° case, due to symmetry in the pressure field (Fig. 31), one obtains the same force F_0 for both the downstream and the upstream slab; on the contrary, in oblique impingement, the symmetry is no more met and the two slabs undergo different F_0 forces. In Fig. 36, only the maximum of the two values is reported.

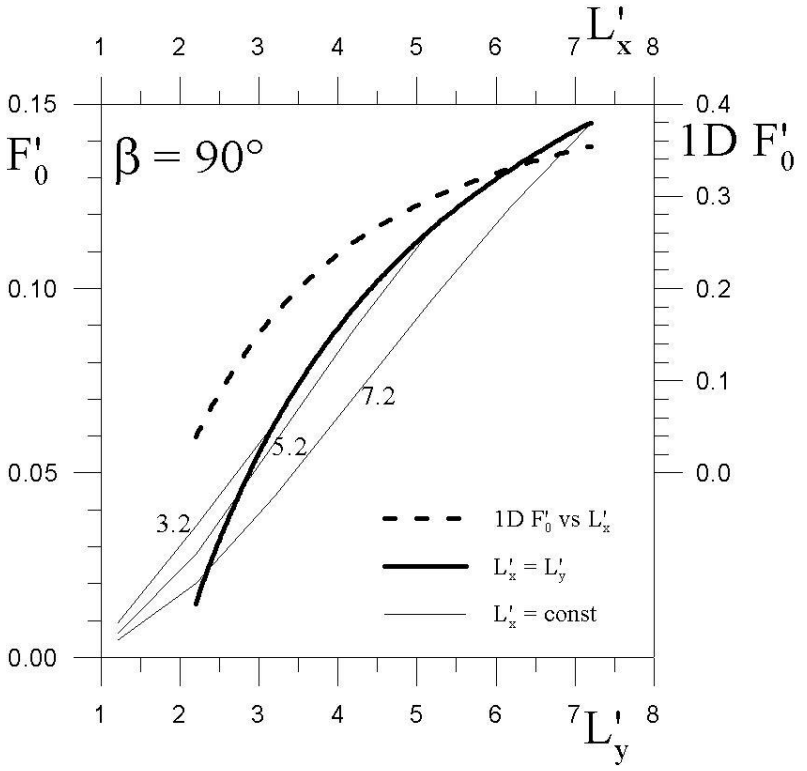
L'x
1 2 3 4 5 6 7 8
0.15
0.10
0.05
0.00
F'0
β = 90°
0.4
0.3
0.2
0.1
0.0
1D F'0
7.2
5.2
3.2
1D F'0 vs L'x
L'x = L'y
L'x = const
L'y

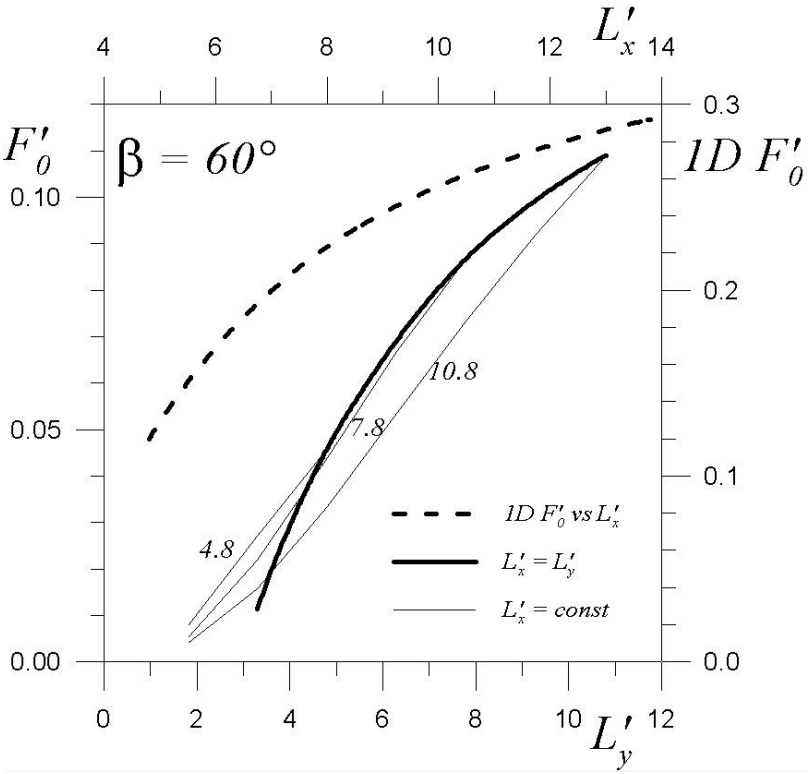
L'x
4 6 8 10 12 14
0.10
0.05
0.00
F'0
β = 60°
0.3
0.2
0.1
0.0
1D F'0
10.8
7.8
4.8
1D F'0 vs L'x
L'x = L'y
L'x = const
0 2 4 6 8 10 12
L'y

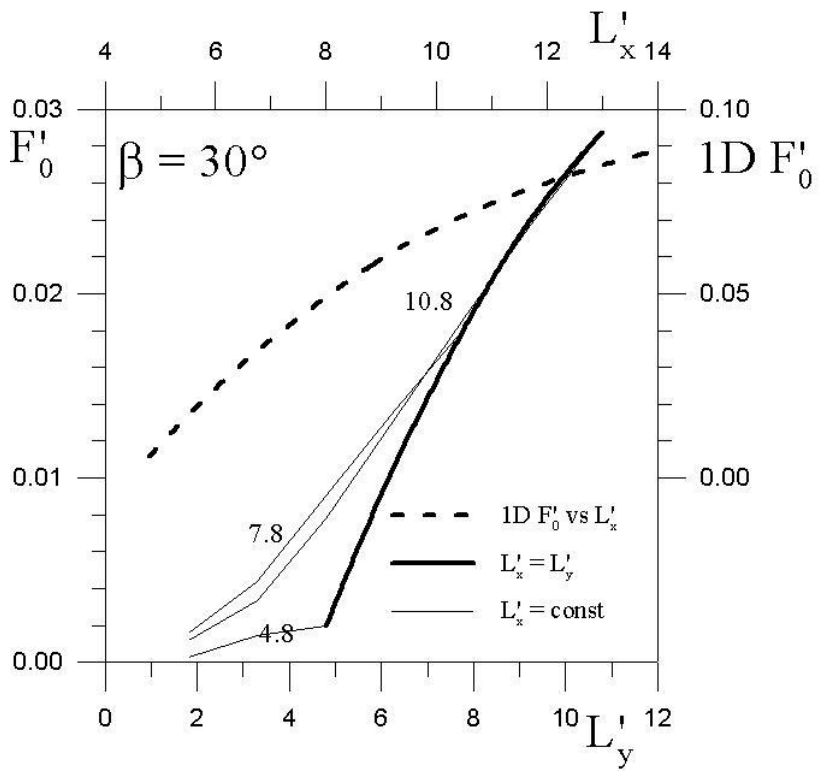

Fig. 32: Dimensionless uplift force *F'0* for different impingement angles *β*, as a function of the dimensionless slab width *L'x* and *L'y*

In Fig. 36, β = 90°, considering square slabs, $L'_y = L'_x$, a decrease in F'_0 is detected at decreasing slab size.

The same considerations apply for rectangular slabs presenting the longer side in the streamwise direction. One can note that, i) decreasing the slab width L'_y at constant L'_x, the total force F'_0 reduces; ii) the force F'_0 tends to 0 for a finite slab size and gives negative stabilizing values for smaller sizes. Both effects can be explained by considering the different pressure fields over and under the slab. Over the slab, the pressure field is Gaussian along the flow direction and constant in the transversal one. According to the 1D scheme, the pressure under the slab is linear between the two extremities where it assumes the value of the pressure at the unsealed joints. In a 2D scheme, the unsealed joints are present along the whole slab boundary and the pressure field under the slab is obtained solving Eq. (5.15) with the pressure along the slab unsealed joints as boundary condition.

With reference to the first effect, since the pressure at the slab upper face is constant in the transversal direction, a reduction in the total uplift force in the 2D case respect to the 1D case is expected, more and more significant when L'_y decreases at constant L'_x, tending towards zero when $L'_y \to 0$.

The second effect is easily explained when considering the 1D case, where the pressure over the slab is Gaussian while the pressure under the slab is linear between the joints. Starting from $L'_x=0$, the difference in pressure over and under the slab is null, and so is the total force. By increasing the slab length, a larger amount of pressures over the slab than under the slab is observed due to the convex form of the Gaussian curve near the maximum, as compared to the linear distribution, so that the total force is negative. Due to the shape of the Gaussian curve, at larger L'_x the amount of the pressure on the slab becomes smaller than the linear one under the slab, giving progressively larger positive values of the total force F_0.

In case of inclined jets, here reported for β equal to 60° and 30°, the same considerations, as developed for the orthogonal impingement, can be drawn from a qualitative point of view.

The maximum force F_0 is detected for the slab lying upstream of the stagnation point, because the dissymmetry induces a larger reduction in the pressure field extension at the upper surface. In Fig. 36, for the 1D case, the uplift force $F_0' = (F_u - F_S)/(L_x \rho v_\zeta^2/2)$ is reported as a function of the unsealed joints at the extremity of the slab length L'_x, at varying impingement angle.

Due to the linear distribution of pressure under the slab between the joints, the maximum force F_0' cannot exceed 0.5 corresponding to a pressure impulse at the impingement joint with $p'_{max}=1$ for $\beta = 90°$.

For $\beta < 90°$, the stagnation pressure p'_{max} is smaller than 1 (Fig. 32), so that the maximum value of the force $F_0' = 0.5\, p'_{max}$ can be obtained using the proper value of the stagnation pressure p'_{max}.

In a 1D scheme, in case of failure of the slab joint at impingement only, the uplift pressure under the slab is constant, equal to the impingement pressure. In this case one obtains $F_0' = (F_u - F_S)/(L_x \rho v_\zeta^2/2) = p'_{max} - F_S/(L_x \rho v_\zeta^2/2)$, with a maximum value of $F_0' = p'_{max}$.

In Fig. 37, the mean dimensionless hydrodynamic force at slab upper and lower faces, for i) open joints at slab extremities (termed *unsealed* in the figure) and ii) sealed joints and waterstop failure at impingement (termed *sealed* in the figure), as measured by Melo et al. (2006) for vertical jet in an unconfined domain are compared to the present theoretical results in terms of the coefficients $C_{F\,up} = F_S / \left(\rho v_e^2 y_e / 2 \right)$ and $C_{F\,low} = F_u / \left(\rho v_e^2 y_e / 2 \right)$. These are shown as a function of the slab dimensionless length L'_x. From the figure, a good agreement is detected for $C_{F\,up}$ and $C_{F\,low}$ for case i). In case ii), some discrepancies can be detected in $C_{F\,low}$, meaning an uplift pressure smaller than its theoretical value, equal to the impingement pressure.

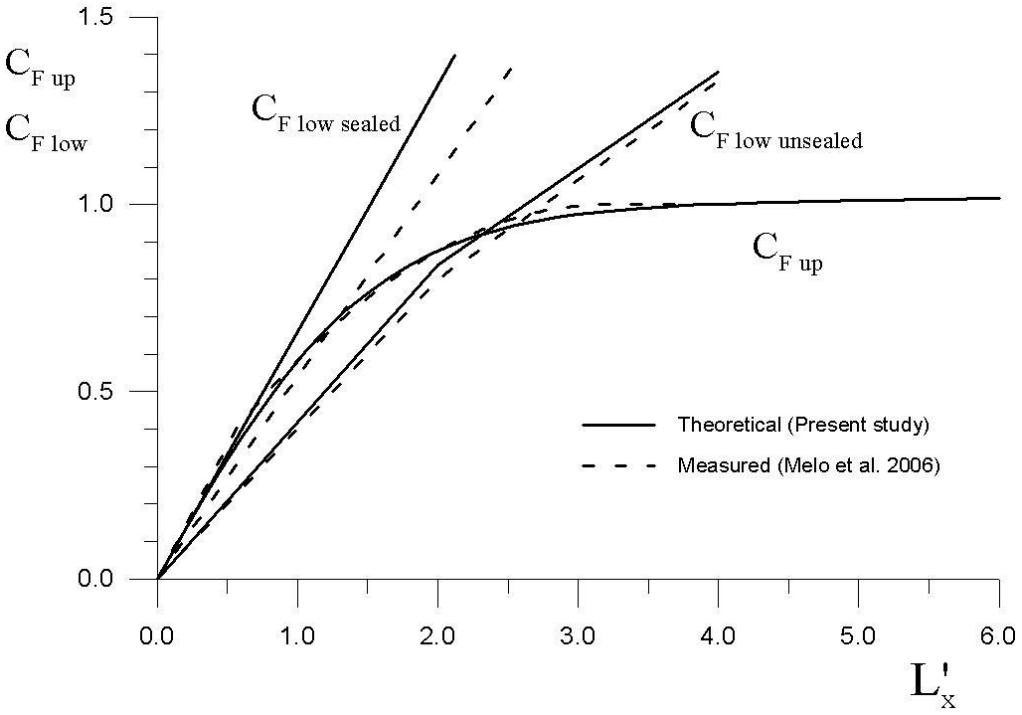

Fig. 33: Comparison between the present theoretical approach (1D) and experimental results (Melo et al., 2006) in terms of force components for vertical jet in an unconfined domain

When accounting for the fluctuating component $F''(t)$ (Eq. 5.14), a thickness s'' related to the fluctuating component must be added to the thickness s (Eq. 5.16). From a theoretical point of view, this analysis is formally the same as applied to slab stability under hydraulic jump (Fiorotto and Rinaldo, 1992a), but it requires the knowledge of the covariance structure of the pulsating pressures at

the bottom (Barjastehmaleki et. al., 2015; Barjastehmaleki et. al., 2016). In literature, the experimental analyses are generally limited to point evaluations of pressure, so that the evaluation of the fluctuating forces is prevented.

Some suggestions on the relative importance of the fluctuating pressures in slab stability can be drawn from the experimental data presented by Melo et al. (2006), Fig. 17. In this figure, the standard deviations of the fluctuating forces at the slab upper face, $s(F'')_{up}$, and under face, $s(F'')_{low}$, are reported, made dimensionless with the quantity $\frac{1}{2}\,\rho\, v_e^2\, y_e$ with reference to a unit width slab. Values are practically independent of the slab length and quite constant in the range 0.05 ÷ 0.1, the first value applying to $L_y/b \sim 5.2 \div 5.9$ and the latter to $L_y/b \sim 1.7 \div 2.0$.

The variance of the fluctuating uplift force, $F'' = F''_{low} - F''_{up}$, is $s^2(F'') = s^2(F'')_{up} + s^2(F'')_{low} - 2\, cov(F''_{up}; F''_{low})$ where *cov* indicates the covariance. Melo et al. (2006) observe that the pressure correlation at the upper face, causing the force F''_{up}, is weak; therefore, also the correlation between the pressure acting on the upper face of the slab and along the joints must be weak. The uplift pressure under the slabs depends on the pressure along the joints that propagates (Eq. 5.15) thus causing the force F''_{low}. As a consequence, the pressures under and on the slab are poorly correlated, as well as the resulting forces F''_{up} and F''_{low}. Therefore, the force covariance term can be neglected and the uplift force standard deviation becomes $s(F'') = \sqrt{s^2(F'')_{up} + s^2(F'')_{low}} \approx \frac{1}{2}\,\rho\, V_e^2\, y_e\, C_L$, with C_L ranging in 0.1 ÷ 0.2, for $L_y/b \sim 5.2 \div 5.9$ and $L_y/b \sim 1.7 \div 2.0$ respectively.

The fluctuating component of the design force F''_{max} is proportional to $s(F'')$ when assuming a two parameter statistical distribution of the pulsating pressures. Experimental analyses (Castillo et al., 2014b) pointed out fluctuating pressure distributions close to the Gaussian one (skewness in the range -1.9 ÷ 0.8 and kurtosis in 2.62 ÷ 2.92). At the prototype scale, the relevant frequencies are in the order of 1 Hz, so that, when evaluating the probability of exceedance during a several days flood, the ratio $n = F''_{max}/\, s(F'')$ attains easily values as large as 5 (Fiorotto and Rinaldo, 1992b), increasing with flood duration. For instance, Castillo et al. (2014b) determine *n* in the order of 5 ÷ 7, close to the

value of 6 which was obtained by Marson et al. (2007) in a long run experiment for the plunge pool lining protection design of the Esaro Dam.

The choice of a suitable value for n is a critical issue for design purposes, since slab stability must be assured for a total flood duration as expected during the structure lifetime; for this reason, n=6 can be considered as a minimum value. As a consequence the maximum force due to the fluctuating pressure is $F''_{max} = ½ \rho V_e^2 y_e 6C_L$.

In Fig. 38, for i) open joints at slab extremity and ii) sealed joints with waterstop failure at impingement, the dimensionless forces $C''_F = F''_{max} / (½ \rho V_e^2 y_e)$ due to the fluctuating pressures and the mean dimensionless dynamic force $C_F = C_{F\,low} - C_{F\,up}$ are reported as a function of L'_x.

From the figure, one can note: i) for the unsealed joint case, the fluctuating forces prevail on the mean dynamic component up to a value $L'_x \approx 5$, corresponding to $L_x \approx 0.5\,H$; when increasing the slab length, the mean dynamic component prevails on the fluctuating component; the latter is anyway significant, accounting for some additional 30% even at $L'_x = 10$ that means $L_x \approx H$; ii) for sealed joints with waterstop failure at impingement, the fluctuating forces prevail on the mean dynamic component only for $L'_x < 1.5$; for larger slabs, the mean dynamic force prevails on the fluctuating component, though the latter still maintains some importance: for instance, at $L'_x = 5$, the fluctuating force accounts for some additional 25% respect to the mean dynamic force.

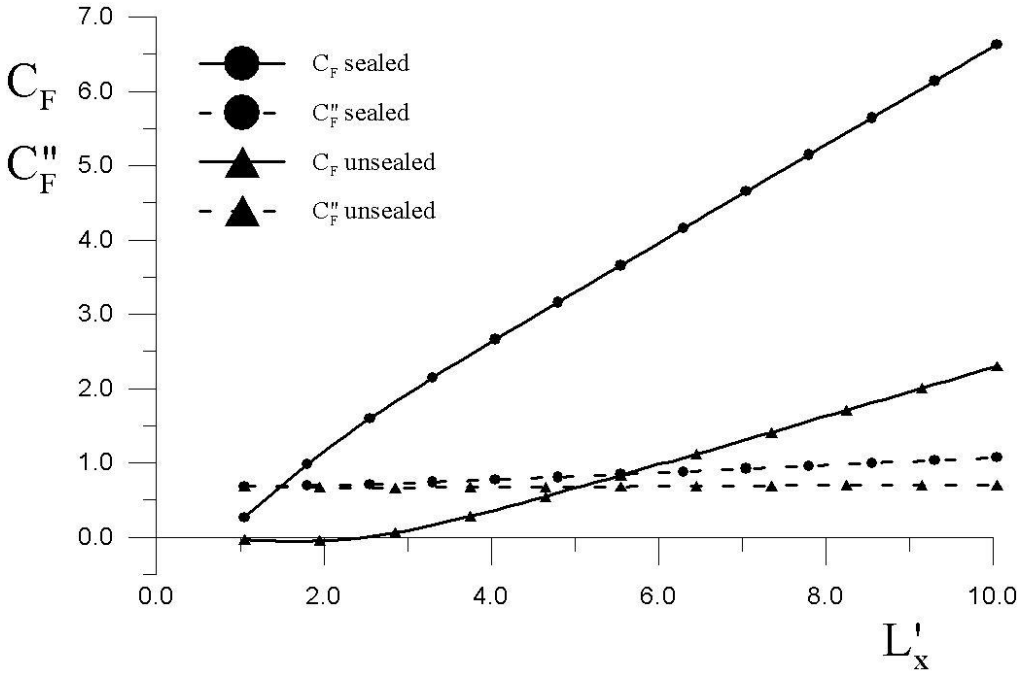

Fig. 34: Dimensionless mean (solid line) and fluctuating (dashed line) pressure forces acting on a slab (1D case)

5.6 Design example and discussion

A design example concerns a Froude scale hydraulic model of the Sa Stria Dam (Italy), as described in Ursino et al. (2003). A ski-jump spillway, followed by a plunge pool, characterizes the dam.

The entering jet velocity is v_e = 37 m/s with a jet thickness y_e = 0.33 m, a specific discharge q_e of 12 m^3/s/m, a momentum *M*e = 452 kN/m and an impact angle α = 38°. The jet length is ζ_1 = 8.5 m.

Close to the plunge pool bottom, via Eqs. (5.1) to (5.5), one obtains a half-width b = 0.86 m, a maximum free jet velocity equal to 17 m/s and a specific discharge q equal to 35 m^3/s/m. The discharge ratio q_e/q is equal to 0.34 that corresponds (Fig. 32) to an angle β close to 60°.

Considering a concrete slab 7 m long and 4.5 m wide, with failed waterstops at both extremity, with a ratio L_x/b = 8.13, and Ly/b = 5.22, one obtains a dimensionless force F_0'=0.25 (1D F_0' in Fig. 36, β=60°). The mean force is F_0 = 0.25×7×4.5×1000×17^2/2 = 1136 kN, whence (Eq. 5.16) a slab thickness s = 2.4 m is computed.

The fluctuating component per unit width is derived by extracting the value $C''_{F\ unsealed}$ = 0.6 from Fig. 37 (with L'_x = 8.13) as F''_{max} = ½ ρ V_e^2 y_e 0.6. For the 4.5 m wide slab one obtains F^*_{max} = 0.5×1000×37^2×0.33×0.6×4.5 = 610 kN, so that the slab thickness s^* associated to the fluctuating force component is equal to s^* = 610/7/4.5/15000 = 1.25 m. The total thickness of the slab is therefore $S = s+s^* \approx 4$ m.

In the case when all joints are open, a relevant reduction in the slab thickness is obtained. For example, considering a prototype slab 7×4.5 m with L_x/b = 8.13, L_y/b =5.22, for an impingement angle of 60° one obtains in turn: from Fig. 35 (β = 60°), a value F'_0 = 0.06; a force F_0 = 0.06×7×4.5×1000×17^2/2 = 273 kN; a thickness s = 0.6 m (Eq. 5.16).

The total thickness of the slab is here S = 0.6 + 1.25 ≈ 2 m

The use of open joint square slabs, 3 m in size, leads to $L_y/b = L_x/b \approx 3.5$ so that, from Fig. 35, the effect of the mean dynamic force F_0 can be neglected, since the resulting equivalent slab thickness is of the order of ten centimeters. With reference to the fluctuating components for $L_x/b \approx 3.5$, one obtains F''_{max} = ½ ρ V_e^2 y_e 0.9. Therefore, it is F^*_{max} = 0.5×1000×372×0.33×0.9×3 = 610 kN and $S \approx s^*$= 4.5 m, larger than the one obtained for the rectangular 7×4.5 m slab. This highlights the importance of the fluctuating pressures in slab stability as a function of slab shape and size.

This fact was proved experimentally in a similar case, related to the Esaro Dam (Italy) (Marson et al., 2007), as shown in Fig. 34 in Marson et al. (2007), where 3 m thick concrete slabs 7×4.5 m were stable while cubic slabs, 3 m in side, were dislodged by the jet.

The use of open joints avoids the risk of joint failure and produces a consistent reduction in slab thickness. In this case, slabs should be rectangular with the larger side along the flow direction; slab transversal width should be kept at a technical minimum in order to obtain a consistent reduction of both the mean (Fig. 35) and fluctuating components of the dynamic force and, therefore, of the concrete thickness S.

In the case of anchored slabs, a dynamic analysis is needed according to Fiorotto and Salandin (2000) and Mazhari and Schleiss (2010). The equivalent inertial effect, accounting for slab thickness, added water mass and elastic characteristic

of the anchor, gives an increase in anchored steel area that can reach two times the area computed in static conditions in terms of equivalent concrete thickness (Fiorotto and Rinaldo, 1992a). The issue is proved experimentally in the previous chapter.

Application of physical model results to prototype conditions deserves some attention, with reference to slab foundation (e.g. Bollaert and Schleiss, 2003; Fiorotto and Caroni, 2014) and air concentration at impact for both nappe jets (e.g. Castillo et al., 2014b) and ski jump jets (e.g. Pfister et al., 2014; Schmoker et. al., 2008). The latter applies to the prototype used in the design section with reference to a physical model example, where a 33 cm thick jet with a velocity of 37 m/s spreads in the air, being no more compact when plunging in the pool. In the example, the ratio between the jet breakup length and the drop height is 1.5; this gives a decrease in the mean dynamic pressure of about 20% and an increase in fluctuating pressures of about 35%, according to Castillo et al. (2014b).

With reference to the slab foundation, Eq. (5.15) is valid when small slabs lie on the channel floor disjointed by a thin water layer thickness, like in physical models. In prototypes, a seepage transient flow model (Fiorotto and Caroni, 2014), must be adopted to take into account hydraulic and geometric characteristics of the foundation layer and, eventually, the effect of air entrance through the open joints, as well as resonance. This allows to define the correction that must be applied to physical model results.

Comprehensive analyses, as reported in Pinheiro and Melo (2008) and Castillo et al. (2014b), account for the presence of air in the jet at impact. Increasing air concentration at the bottom, a progressive reduction of the dimensionless stagnation pressure p'_{max} occurs, as experimentally proved by Pinheiro and Melo (2008). With reference to the pulsating pressures, in Castillo et al. (2014b), Fig. 36, the experimental standard deviation of the pulsating pressure is reported as a function of the water cushion depth / jet thickness ratio; for fully developed conditions, a decrease in the standard deviation is detected, when increasing air concentration.

A further question relating to the application of model results to prototype conditions concerns the jet width parameter *b*; in Castillo et al. (2014b), Fig. 13, the comparison of the mean pressure distribution at the bottom in non-aerated

conditions (Cola, 1965) with the data in aerated conditions shows an increment of *b* at increasing air concentration. In the example, this increment is estimated in 30%.

Adopting a proper value for the impingement bottom pressure (e.g. Pinheiro and Melo, 2008) and for the *b* scale (Castillo et al., 2014b), the results, as above obtained in non-aerated conditions, can be extended to cases when air concentration at bottom is relevant. For the rectangular 7×4.5 m slab in the example, the increment of 30% in *b* increases F'_0 from 0.06 to 0.065. Due to a decrease of 20% of the mean dynamic pressure the thickness *s* decreases to 0.52 m. The increment in the fluctuating components is of 35%, so that $s^* = 1.7$, leading to a slab total thickness S=2.3 m, 0.45 m larger than in non-aerated conditions. In any case, a proper safety coefficient must be assigned, taking into account the uncertainties in foundation response and air concentration effects.

5.7 Conclusions

The following conclusions can be drawn from the present study, addressing the case of fully developed jets.

- The impingement angle β is independent from the impact angle α of the jet at the plunge pool water surface; it depends on the ratio q_e/q and, as a consequence, on the ratio ζ_1/y_e. The minimum impingement angle is larger than 30°.
- The impingement angle β has an important role in the pressure field at the bottom. The pressure distribution (Fig. 31) shows a progressive loss in symmetry at decreasing β, together with a consistent reduction of the maximum pressure at impingement.
- The dimensionless uplift force F'_0 depends on the dimensionless slab lengths L'_x and L'_y (Fig. 36); the same for the dimensionless uplift force F''_{max}, as highlighted in Fig. 38 and in the design example. The relative importance of these two forces depends on the slab size as proved experimentally in the physical model of the Esaro Dam. For this reason, it cannot be said a priori whether the mean dynamic force prevails on the fluctuating component in plunge pool slab stability analysis.

- In case when open joints are used, as in the case of the Esaro Dam, the risk of joint failure is avoided and a consistent reduction in slab thickness is obtained. In this case, slabs should be rectangular with the larger side placed along the flow direction; width of the slab in the transversal direction should be kept at a technical minimum.

This chapter is published in Journal of Hydraulic Engineering (ASCE).

Fiorotto, V., Barjastehmaleki, S., and Caroni, E. (2016). "Stability Analysis of plunge pool Linings." *J. Hydraul. Eng.* 10.1061/(ASCE)HY.1943-7900.0001175.

6

Conclusions

The design of concrete thickness of the spillway stilling basins and plunge pools linings is investigated. In this thesis pioneering approaches to evaluate the slab protection are reported. In particular, in the case of stilling basins, a simplified approach based on the Taylor hypothesis is used to assess the pressure field acting on the slab, while the pressure propagation at the lower surface of the slab is evaluated using a 3D model based on unsteady flow analysis of seepage through porous media. By this approach, it is possible to consider the effect of finite thickness foundation layers, typical in the case of earth dams, rock-fill dams and in other dam types. Slabs with unsealed joints are considered and compared to the case of sealed joints. The dynamic behavior of anchored slabs is also investigated. In the case of Plunge pool, the slab stability under the impact of an impinging jet is theoretically and numerically analyzed, with reference to the mean characteristics of the flow field. The followings are the main achievements of the work presented in this thesis.

Pressure on slabs via Taylor hypothesis

In chapter 2, the evaluation of structure of whole pressure fluctuations under hydraulic jumps is investigated. To the scope, a consistent experimental work is generally required in order to obtain the relevant correlation structures which are needed to compute the reduction factors Ω^* and Ω. Such computation leads to more realistic results than direct assessment of slab stability in unsealed joints scale models whenever the foundation layer behavior cannot be properly simulated by lab setups. For sealed joints, the present evaluation avoids the use of rather awkward devices for direct assessment of slab stability.

Much simplification is obtained by making at point pressure measurements and by deriving spatial correlation structures from the autocorrelation function via

Taylor hypothesis. To this extent, the validity of the hypothesis was checked and an evaluation of the celerity of propagation of pressure fluctuations was obtained.

By comparing the autocorrelation function with the spatial correlation structure, as obtained on an extensive experimental program, propagation celerity values were estimated in the longitudinal and transversal direction as well as at several oblique directions.

The comparison of measured spatial correlation coefficients with the ones obtained via Taylor hypothesis proved satisfactory, especially in the near field, that is, the area of most importance in computing the reduction factor and where the first order Taylor expansion is more likely to furnish adequate results. Comparison of at-piont celerity of propagation of pressure fluctuations in the flow direction is congruent with the maximum velocity in the longitudinal direction. $\bar{c}_x/u_m$ = -0.02ξ/y_1 +1.1 for longitudinal celerity and $\bar{c}_y/u_m$=1.83 for transversal celerity are proposed as general equations for computing the celerity at each point in the hydraulic jump region, knowing the maximum velocity profile under the hydraulic jump at the pivot point. Eq. (2.17) is suggested to evaluate the mean celerity in a general oblique direction. Knowing the values of celerity in any direction, Eq. (2.18) allows to compute the Ω^* and Ω coefficients using the single point pressure measurements.

The comparison of Ω coefficients computed by the presented approach show a good agreement with literature

This chapter verified the validity of the Taylor hypothesis in reproducing spatial correlations from single point autocorrelation function and presented a simplified approach that can be useful in the structural design of stilling basin linings

Pressure under slabs

This chapter presented a theory based on transient seepage flow that is considering the three dimensionality of the flow under the slab, overcoming the concept of thin film, and being applicable in a more realistic way to finite thickness mediums underneath the slab.

The comparison of the results in 3D case with the 2D one showed that at a constant value of thickness Z' and dimensionless parameter RL_x/a, the values of the Ω in 3D cases are smaller than the 2D ones. It can be concluded that by considering the slab shape in 3D context, a non-negligible reduction in the value of Ω coefficient can be pointed out; this results in a realistic and more precise evaluation of slab thickness. Furthermore, the laboratory results can not assure the safety design and need a correction in order to taking into account the foundation response especially for small values of Z'.

From this chapter a criterion in the lining design is drawn in the both cases: i) slab with sealed and ii) unsealed joints in the real life conditions. The comparison between the two cases highlight the technical and economical convenience to use unsealed joint that, generally avoid the use of anchors whenever that is technically feasible.

Anchored slab

When slab stability in spillway stilling basins can not be ensured only by its weight, fraction of the uplift force is sustained by anchors. Therefore, the dynamic behavior of the system (slabs plus anchors) has to be considered.

In this chapter an experimental study was done in order to define the dynamic behavior of anchored slab. In the case of sealed joints the anchors design is analyzed theoretically with the support of experimental data. The theoretical difference in the analysis between the case of unsealed and sealed joint is highlighted. In the limit of the present work the dynamic amplification factor of the pressure is computed around 1.8.

Stability analysis of plunge pools linings

The stability of concrete slabs or rock blocks at plunge pool bottom depends on the instantaneous pressure field and can be investigated with reference to the mean dynamic pressure and to the fluctuating components.

In this chapter, stability of a plunge pool bottom under the impact of an impinging jet is theoretically and numerically studied. Numerical simulations with Ansys Fluent were conducted using a turbulence SST model, showing a good agreement with the solution obtained via the inviscid rotational model for impingement angles of 70°, 50° and 30°.

The analysis of results show that the impingement angle β has an important role in the pressure field at the bottom and it is independent from the impact angle α of the jet at the plunge pool water surface. The impingement angle β depends on the ratio q_e/q and, as a consequence, on the ratio ζ_1/y_e. The minimum impingement angle is larger than 30°.The dimensionless uplift force F_0' depends on the dimensionless slab lengths L'_x and L'_y; as well as the dimensionless uplift force F''_{max}.

This study offers a practical design methodology to define the concrete thickness of the plunge pool lining in a physical model context and suggestions to apply these results to the prototype.

The aim of the thesis is to provide overall criteria in the structural design of stilling basins and plunge pools taking into account the air effect and foundation response. The novel criteria proposed by this thesis are relevant to a robust and safe design and maintenance of stilling basins and plunge pools downstream of large dams that is a timely addition to the current literature results.

References

Abdul Khader, M. H., and Elango, K. (1974). "Turbulent pressure field beneath a hydraulic jump." *J. Hydraul. Res.*, 12(4), 469-489.

Barjastehmaleki, S., Fiorotto, V., and Caroni, E. (2016). "Spillway Stilling Basins Lining Design via Taylor Hypothesis." *J. Hydraul. Eng.*, 10.1061/(ASCE)HY.1943-7900.0001133.

Barjastehmaleki, S., Fiorotto, V., and Caroni, E. (2015). "Stochastic Analysis of Pressure Field in Hydraulic Jump Region via Taylor Hypothesis." *E-Proc. 36th IAHR World Congress*, The Hague, the Netherlands, 1-12.

Belicchi, M., Cerlini, Denis., Maione, U., Fiorotto, V., an Volpe, F. (2008) "Mignano dam rehabilitation", L'Acqua, (6), 17-32.

Bellin, A., and Fiorotto, V. (1995). "Direct dynamic force measurement on slab in spillway stilling basin." *J. Hydraul. Eng.*, 121(10), 686–693. 10.1061/(ASCE)0733-9429(1995)121:10(686), 686–693.

Beltaos, S. and Rajaratnam, N. (1973). "Plain turbulent impinging jet." *J. Hydraul. Res.*, 11(1), 29–59.

Bollaert, E., and Schleiss, A. (2003). "Scour of rock due to the impact of plunging high velocity jets. Part I: A state-of-the-art review ; Part II: Experimental results of dynamic pressures at pool bottoms and in one - and two-dimensional closed-end rock joints." *J. Hydraul. Res.*, 41(5), 451–480.

Bowers, C. E., and Toso, J. (1988). "Karnafouli project, model studies of spillway damage." *J. Hydraul. Eng.*, 10.1061/(ASCE)0733-9429(1988)114:5(469), 469–483.

Bowers, C. E., and Tsai, F. H. (1969). "Fluctuating pressure in spillway stilling basins." *J. Hydraul. Div.*, Vol.95, HY6, 2071-2080.

Caroni E., V. Fiorotto and M. Belicchi. (2002)"Slab stability in hydraulic jump stilling basins as derived from physical modeling.", *Rock scour due to falling high-velocity jets*, A. Schleiss, eds., Balkema Lisse, 43-54.

Castillo, L.G. and Carrillo, J.M. (2011) "Numerical simulation and validation of hydrodynamics actions in energy dissipation devices". *Proc. 34th IAHR World Congress*, Brisbane, 1, 4416–4423.

Castillo, L.G. and Carrillo, J.M. (2015) "Experimental and numerical analysis of velocities in plunge pools of free falling spillways". *E-Proc. 36th IAHR World Congress*, The Hague, the Netherlands, 1-8.

Castillo, L.G., Carrillo, J.M., and Sordo-Ward, A. (2014a). Simulation of overflow nappe impingement jets. Journal of Hydroinformatics, 16 (4), 922-940.

Castillo, L.G., Carrillo, J.M. and Blazquez, A. (2014b) "Plunge pool dynamic pressures:a temporal analysis in the nappe flow case", *J. Hydraul. Res.*, ISSN 0022-1686 print/ISSN 1814-2079 online, 1-18.

Castro, O. O., and Hager, W. H. (2009). "Classical hydraulic jump: basic flow features." *J. Hydraul. Res.*, 47(6), 744-754.

Chanson, H. (2007). "Air bubble entrainment in hydraulic jumps: physical modelling and scale effects." *Proc. 32nd IAHR Biennial Congress*, Venice, Italy, 10 pages (CD-ROM)

Cola, R. (1965). "Energy dissipation of a high-velocity vertical jet entering" *Proc. XI IAHR Congress*, Leningrad, 1(1.52), 1-13.

Epely-Chauvin, G., De Cesare, G. & Schwindt, S. (2014). Numerical modelling of plunge pool scour evolution in non-cohesive sediments. *Engineering Applications of Computational Fluid Mechanics*, *8(4)*, 477–487.

Federspiel, M.P.E.A. (2011). "Response of an embedded block impacted by high-velocity jets" (PhD Thesis). *Faculté environnement naturel, architectural et construit, École Politechnique Fédérale de Lausanne, Suisse.*

Fiorotto, V., and Caroni, E. (2014). "Unsteady seepage applied to lining design in stilling basins." *J. Hydraul. Eng.*, 10.1061/(ASCE)HY.1943-7900.0000867, 140(7), 1-9.

Fiorotto, V., and Rinaldo, A. (1992a). "Fluctuating uplift and linings design in spillway stilling basins." *J. Hydraul. Eng.*, 10.1061/(ASCE)0733-9429(1992)118:4(578), 578-596.

Fiorotto, V., and Rinaldo, A. (1992b). "Turbulent pressure fluctuations under hydraulic jumps." *J. Hydraul. Res.*, 30(4), 499-520.

Fiorotto, V., and Salandin, P. (2000). "Design of anchored slabs in spillway stilling basins." *J. Hydraul. Eng.*, 10.1061/(ASCE)0733-9429(2000)126:7(502), 502–512.

Hager, W. H. (1992). *Energy Dissipators and Hydraulic Jump*, Water Science & Technology Library 8. Kluwer: Dordrecht.

Hager, W. H., and Bremen, R. (1989). “Classical hydraulic jump: sequent depth.” *J. Hydraul. Res.*, 27(5), 565–583.

Hinze, J. O. (1959). *Turbulence*, McGraw-Hill, New York.

Kotsovinos, N.E. (1976). “A note on the spreading rate and virtual origin of a plane turbulent jet.” *J. Fluid Mech.*, 77(2), 305-311.

Kotsovinos, N.E. (1978a). “A note on the conservation of the volume flux in free turbulent .” *J. Fluid Mech.*, 86(1), 202-203.

Kotsovinos, N.E. (1978b). “A note on the conservation of the axial momentum of a turbulent jet.” *J. Fluid Mech.*, 87(1), 55-63.

Kotsovinos, N.E. and Angelidis, P.B. (1991). “The momentum flux in turbulent submerged jets.” *J. Fluid Mech.*, 229, 453-470.

Leutheusser, H. J., and Kartha, V. C. (1972). "Effect of inflow condition on the hydraulic jump." *J. Hydr. Div.*, ASCE, 98(HY8), 1367-1386.

Liu, P., Gao, J. and Li, Y. (1998). “Experimental investigation of submerged impinging jets in a plunge pool downstream of large dams.” *Science in China (Series E)*, 41(4), 357-365.

Liu, P. Q., and Li, A. H. (2007). “Model discussion on pressure fluctuation propagation within lining slab joints in stilling basins.” *J. Hydraul. Eng.*, 10.1061/(ASCE)0733-9429(2007)133:6(618), 618–624.

Lopardo, R. A., and Henning, R. E. (1985). “Experimental advances on pressure fluctuation beneath hydraulic jumps.” *Proc, 21st Congress, International Association of Hydraulic Research*, Vol. 3, Melbourne, Australia.

Lopardo, R. A., De Lio, J. C., and Vernet, G. F. (1982). “Physical modeling on cavitation tendency for macroturbulence of hydraulic jump.” *Proc. International Conference on the hydraulic modeling of civil engineering*

structures, Coventry, England, 109 – 121.Mahzari, M., and Schleiss, A. J. (2010). "Dynamic analysis of anchored concrete linings of plunge pools loaded by high velocity jet impacts issuing from dam spillways." *Dam Eng*., 20(4), 307–327.

Marson, C., Fiorotto, V., and Caroni, E. (2007). "Lining design in spillway stilling basins." *Piña, Portela e Gomes eds., Dam Engineering, Proc. 5th Int. Conference, 14-16 feb 2007, Lisboa,* 299-306.

Mahzari, M,. Arefi, F., Schleiss, A.J. (2002). "Dynamic response of the drainage system of a cracked plunge pool liner due to free falling jet impact", Rock Scour due to falling high velocity jets, 227 - 237, A.A. Balkema, Swets&Zeitlinger B.V. Lisse, The Netherlands.

Mahzari, M., Schleiss, A. J. (2010). "Dynamic analysis of anchored concrete linings of plunge pools loaded by high velocity jet impacts issuing from dam spillways." *Dam Engineering*, Volume XX, Issue 4.

Melo, J. F., Pinheiro, A. N. and Ramos, C. M. (2006). "Forces on plunge pool slabs: influence of joints location and width." *J. Hydraul. Eng.*, 10.1061/(ASCE)0733-9429(2006)132:1(49), 49-60.

Pfister, M., Hager, W.H. and Boes, R.M. (2014) "Trajectories and air flow features of ski jump-generated jets, *J. Hydraul. Res.,* 52, (3), 336–346.

Pinheiro, A.N. and Melo, J.F. (2008). "Effect of jet aeration on hydrodynamic forces on plunge pool floors." *Canadian J. of Civil engrg.*,35(5) 521-530.

Rajaratnam, N. (1965) "The hydraulic jump as a wall jet." *J. of Hydraul. Div*., 91 (HY5).

Rouse, H., Siao, T. T., and Nagaratnam, S. (1955). "Turbulence characteristics of hydraulic jump." *Trans, of ASCE,* Vol. 124.

Rubel, A. (1980). “Computations of jet impingement on a flat surface.” *AIAA Journ.*, 18(2), 168-175.

Sanchez Bribiesca, J. S., and Capella Viscaino, A. C. (1973). “Turbulent effects on the lining of stilling basin.” *Proc. 11th Int. Congress on Large Dams*, Vol. 11(Q2), Madrid, Spain, 1575–1592.

Schauer, J. J. and Eustis, R. H. (1963). “The flow development and heat transfer characteristics of plane turbulent impinging jets.” *Dept. of Mechanical Engineering, Stanford University*, TR3.

Schmocker, L., Pfister, M., Hager, W. H., and Minor, H. E. (2008). “Aeration Characteristics of Ski Jump Jets.” *J. Hydraul. Eng.*, 10.1061/(ASCE)0733-9429(2008)134:1(90), 90-97.

Taylor, G. I. (1938). “The spectrum of turbulence.” *Proc Roy Soc Lond* 164:476–49

Toso, J., and Bowers, E. C. (1988). “Extreme pressures in hydraulic jump stilling basin.” *J. Hydraul. Eng.*, 10.1061/(ASCE)0733-9429(1988)114:8(829), 829-843.

Tu, C.V. and Wood, D.H. (1996). “Wall pressure and shear stress measurement beneath an impinging jet.” *Experimental thermal and fluid science*. 13, 364-373.

Ursino, N., Salandin, P. and Da Deppo, L. (2003). “Fluctuating pressures at the bottom of a plunge pool.” *Proc. 30th IAHR Congress, Thessaloniki,Greece*, 1-8.

Vasiliev, O. F., and Bukreyev, V. I. (1967). “Statistical characteristics of pressures fluctuations in the region of hydraulic jump.” *Proc, 12th Congress, International Association of Hydraulic Research*, Vol. 2.

Wang, M., Jiang, C., Xia B., and Shang, S. (1984). "Stochastic analysis of pressure fluctuations beneath hydraulic jump and primary discussion on scale of turbulence." *Proc. Fourth IAHR Int. Symposium on Stochastic Hydraulics*, University of Illinois, 199-209.

Wilson, E. H., and Turner, A. A. (1972). "Boundary layer effects on hydraulic jump location." *J. Hydraul. Div.*, 98 (HY7), 1127-1142.